Study of a Bulk Superconducting Synchronous Machine

	2019
	12614　　　550
URL	http://id.nii.ac.jp/1342/00001861/

Doctoral Dissertation

STUDY OF A BULK SUPERCONDUCTING SYNCHRONOUS MACHINE

March 2020

Graduate School of Marine Science and Technology

Tokyo University of Marine Science and Technology

Doctoral course of Applied Marine Environmental Studies

Shaanika Erasmus

Doctoral Dissertation

STUDY OF A BULK SUPERCONDUCTING SYNCHRONOUS MACHINE

March 2020

Graduate School of Marine Science and Technology

Tokyo University of Marine Science and Technology

Doctoral course of Applied Marine Environmental Studies

Shaanika Erasmus

Contents

List of Abbreviations

LTS	Low temperature superconductor
HTS	High temperature superconductor
TFM	Trapped field magnet
PM	Permanent magnet
BSCCO	$Bi_2Sr_2Ca_2Cu_3O_{10}$, Bi2223
REBCO	$REBa_2Cu_3O_{7-\delta}$ (RE: Rare earth element or Y)
GdBCO	$GdBa_2Cu_3O_{7-\delta}$
YBCO	$YBa_2Cu_3 O_{7-\delta}$
MgB_2	Magnesium diboride
T_c	Critical temperature
J_c	Critical current density
I_c	Critical current
H_c	Critical magnetic field
H_{c1}	Lower critical magnetic field
H_{c2}	Upper critical magnetic field
FCM	Field-cooling magnetization
ZFC	Zero-field cooling
PFM	Pulsed-field magnetization
B_{app}	Applied external magnetic field density
B_{trap}	Maximum trapped magnetic field density
$QMG^{®}$	Quench melt growth

Abstract

Due to raising demand for energy and tightening emission legislations, there is a need to improve energy efficiency and develop new, cleaner power systems. Ship propulsion systems which are at the heart of international trade, account for a considerable share of carbon dioxide, sulfur oxide, nitrogen oxide and particulate matter emissions globally. Among all other ship propulsion systems, electric propulsion emerged as one of the most suitable alternatives toward the reduction of environmental emissions and general improvement fuel efficiency. Ship propulsion requires compact megawatt-class motors capable of high output torque density and low speed-operation. Output torque is generally increased by increasing the size or the electromagnetic force of the motor. However, electromagnetic force in a conventional machine is limited by permanent magnet (PM) flux strength, copper wire current carrying capacity and iron core saturation. It has thus been challenging to develop compact multimegawatt motors for ship propulsion using conventional technology.

The discovery of low-temperature superconductors (LTS) and high-temperature superconductors (HTS) opened new possibilities for ship propulsion motor development. Superconductor wires and tapes conduct large dc currents with almost zero joule losses and can thus generate high magnetic fields. HTS can also be used in bulk form as single-grain crystals. Bulk HTS trap and maintain a magnetic flux that is an order of magnitude higher than conventional permanent magnets (PMs). Both superconductor wires, tapes and bulks can be used to develop high power density superconducting machines suitable for ship propulsion.

Current research efforts aim to take leverage of high current carrying capacity and the magnetic flux of both LTS and HTS to develop more efficient and high-power density machines for electric propulsion. Considerable research has been conducted on rotating machines using superconductor wires and tapes compared to bulks. To explore the potential of bulk HTS machines, we developed a 30-kW low-speed radial-gap synchronous machine with an air-cored rotor and a conventional stator with ferromagnetic teeth. The rotor has 4 field poles. Each pole is a rectangular array of melt-growth $GdBa_2Cu_3O_{7-\delta}$ bulks. The poles are cooled by a 150 W capacity thermosyphon which maintains an operating temperature of 30 K. This work studies the bulk HTS machine and the thesis is arranged as follows.

Chapter I offers an introduction to the field of superconductivity, including important properties and terminology. A background on rotating machines, including design, and development of HTS machines, and the use of cryogenic thermosyphon cooling are also provided.

Chapter II presents a literature study covering development and testing HTS synchronous machines. Cryogenic cooling is an integral subsystem is all HTS machines, therefore a review of recent developments around the rotating machine cooling is also given.

Chapter III: HTS cooling system is one of the major enablers as far as HTS application and its adoption in industry are concerned. This chapter focuses on a thermal study of a thermosyphon cooling system for HTS machines. The aim is to investigate temperature distribution in a two-phase thermosyphon to gauge the performance of a thermosyphon as the cooling system of HTS machinery.

Chapter IV presents the study of a radial-flux type bulk HTS machine. Features of the 30-kVA bulk HTS prototype machine and its auxiliaries namely, the cooling, magnetizing and data acquisition systems are described.

Chapter V presents the methodology and results of no-load tests, which are the first set of tests conducted on a radial-flux type bulk HTS machine in the world. The main results of generated voltage and core loss at different speeds and field strengths are presented and discussed. The magnetic flux stability of the rotor is established by comparing flux measurements before and after tests. The presence of harmonics in the output voltage and their effect on as well as the core loss are discussed.

Chapter VI presents the methodology and test results of static load and variable load tests, which are the second set of tests conducted on the bulk HTS machine. The machine's output power, torque and speed are presented along with stator and rotor pole temperature. The magnetic flux stability of the rotor under operation is established by comparing flux measurements before and after tests. A summary, conclusions, and prospects are given in Chapter VII.

Chapter I Introduction

This chapter introduces fundamental concepts that provide a foundation for the remaining chapters and gives an outline of the thesis. Superconductivity and superconductor materials are introduced along with terminologies, properties and their application to bulk high temperature superconducting (HTS) rotating machines for ship propulsion. Rotating machines are discussed next, with a focus on synchronous machines. Subsequent sections outline the purpose of this work, its significance, and scope. The last section gives a chapter by chapter breakdown of the thesis.

1.1 History of superconductivity

Superconductivity is a state wherein a substance conducts electric current with zero resistance when cooled to or below some specific temperature. The transition from normal to superconducting state is marked by a drop in resistance over a certain temperature range. The highest temperature at which the drop is observed, in the absence of an external magnetic field, is called the critical temperature, T_c [1], and each superconductor has a unique one. The first superconductor to be discovered was elemental mercury, in the year 1911 by Dutch physicist H. Kamerlingh Onnes. He discovered that the resistance of mercury suddenly dropped from a finite value to zero at the temperature of 4.15 K, as shown in Fig.1-1.
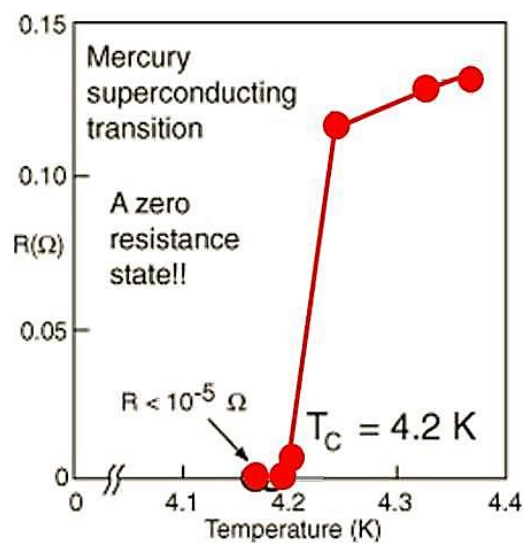
Figure 1-1. Resistance of Mercury as a function of temperature [2]

Thereafter, Kamerlingh Onnes also discovered superconductivity in tin ($T_c = 3.69$ K), lead ($T_c =$

7.26 K), and alloys such as mercury-gold and mercury-tin. Among all elemental superconductors, niobium has the highest T_c (9.5 K) and was discovered in 1930 [3]. Decades that followed saw the discovery of more metallic elements, alloys and even compounds such as NbN (T_c = 16 K) in 1941, V_3Si (T_c = 17.5 K) in 1953, and culminated in the development of first superconductor wires of NbTi at Westinghouse in 1962. In the same year, Brian D. Josephson predicted that a supercurrent could flow between two pieces of superconductor separated by a thin layer of insulator. This tunnelling phenomenon, called the Josephson effect, is used in superconducting devices such as superconducting quantum interference device (SQUID), a magnetometer for measuring weak magnetic fields. A timeline of the discovery of superconductors is shown in Fig. 1-2. The highest T_c had remained at 23.3 K since 1973 leading to a slowdown in pursuit of intermetallic compounds. In fact, until 1986, the highest Tc of superconductors hardly exceeded 20 K [1].
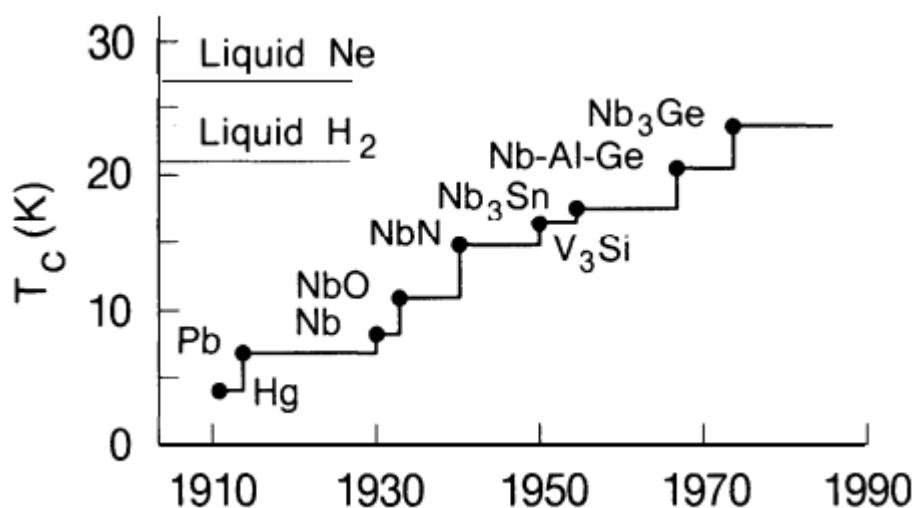
Figure 1-2. Critical temperature and year of discovery of intermetallic compounds [4].

In 1986, Alex Müller and Georg Bednorz made a discovery of superconductivity in lanthanum-barium-copper oxide. This ceramic had a Tc of 35K. The following year, researchers discovered superconductivity in yttrium barium copper oxide (YBCO) with a Tc of 92 K. This discovery, along with those of other cuprate superconductors, were significant in that cooling of these superconductors could be achieved easily using liquid nitrogen which has a boiling point of 77 K at atmospheric pressure. Other milestones include the discovery of superconductivity in mercury copper-oxide comprised of mercury, thallium, barium, calcium, and copper oxide with a Tc of 138 K, and thallium, barium, tellurium, and copper oxide with a T_c near 147 K.

1.2 Properties of superconductors

Superconductors are not just perfect conductors. They exhibit unique properties that distinguish them from a mere perfect conductor. Various theories have been devised to explain the properties of superconductors. A phenomenological theory was put forth by F London and H London in 1935, followed by a semi-phenomenological theory by Ginzburg and Landau in 1950, and a microscopic theory by Bardeen, Cooper and Schrieffer, called the BCS theory, in 1957. The BCS theory attributes superconductivity to cooper pairs, where electrons attract each other to form pairs. This theory has been the most successful at explaining nearly all properties of superconductors, except for some ceramic superconductors. This section describes the properties of superconductors.

1.2.1 Zero resistance

Zero resistance conduction to dc current is the most astonishing property of superconductors. Below Tc, a superconductor conducts transport direct current without joule heat losses as resistivity drops significantly as shown in Fig. 1-3. A current induced in a closed loop of a superconducting sample will flow persistently for years without signs of decay. For comparison, the resistivity of copper at several kelvins is $10^{-9} \Omega \cdot cm$, while the resistivity of superconductors never exceeds $10^{-23} \Omega \cdot cm$, which is a hundred trillion times less than that of copper [1]. The transition from finite resistance to nearly zero resistance is explored in section 1.2.4.
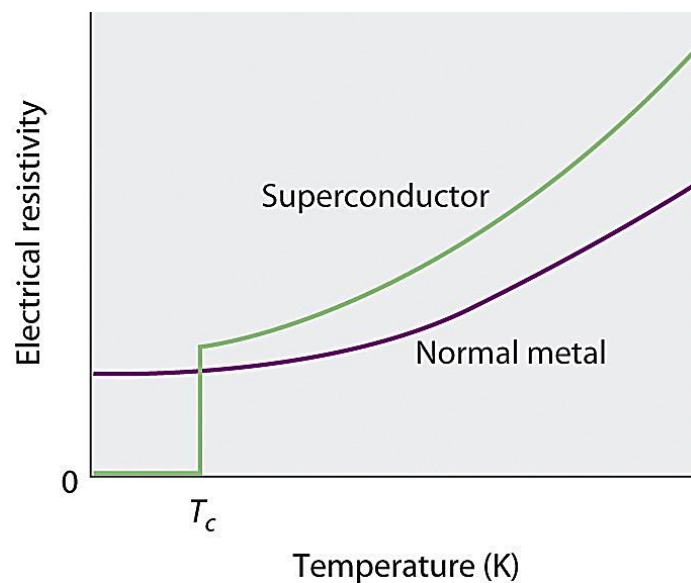
Figure 1-3. Abrupt fall of electrical resistivity in a superconducting material.

1.2.2 Meissner effect

Apart from the zero-resistance characteristic of superconductors, superconductors were found to exhibit another property early on. In 1933, two German physicists, W. Meissner and R. Ochsenfeld discovered that if a superconducting material was cooled in the presence of a magnetic field, the magnetic field lines are expelled from its body. This phenomenon is called the Meissner effect or termed as perfect diamagnetism [1]. Another observation was that a superconductor repels the magnetic field whether the field was introduced before or after cooling. The Meissner effect is responsible for the levitation of a magnet over a superconducting material. Fig. 1-4 shows field cooling (FC) magnetization, whereby a superconductor sample in the normal state is cooled in the presence of an applied magnetic field, H. After reaching its T_c, the field is expelled. This is the hallmark of superconductivity. This repulsion is due to the existence of superconducting screening current in a thin, near-surface surface the superconductor, the magnetic field of which repels the external field.
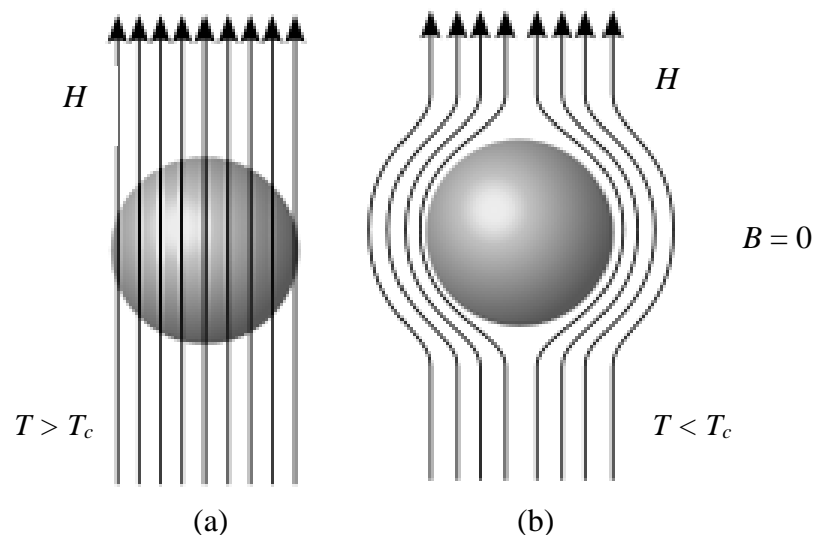
Figure 1-4. The Meissner effect experiment on a type I superconductor under applied magnetic field H. The magnetic field in the sample in normal state (a), is excluded from the interior of the sample when it is in superconducting state (b).

This thin layer also admits a magnetic field. The thickness of the layer is characterized by the London penetration depth λ, in the London equation (1-1). Equation (1-1) was formulated by the London brothers, relating the curl of the screening current density in the superconductor to the local magnetic flux density, $\boldsymbol{B}$ at any point in the superconductor.

$$\nabla \times \boldsymbol{J} = \frac{1}{\mu_0 \lambda^2} \boldsymbol{B} \tag{1-1}$$

The Meissner effect can also be mathematically explained by combining (1-1) with one of Maxwell's equations (1-2), to obtain equation (1-3).

$$\nabla \times \boldsymbol{B} = \mu_o \boldsymbol{J} \tag{1-2}$$

$$\nabla^2 B = \frac{B}{\lambda^2} \tag{1-3}$$

The solution of (1-3) in a one-dimensional case is (1-4), which indicates that the flux density falls exponentially with increasing depth from the superconductor external surface [5].

$$B(x) = B_0 e^{-\frac{x}{\lambda}} \tag{1-4}$$

$B_0 = \mu_0 H$ is the parallel field at the plane boundary, while λ_L is the distance at which $B(x)$ falls by e. The values of λ are typically in the range of several hundred angstroms (Å) for most elemental superconductors. The magnitude of λ is directly related to the superfluid density, and consequently depends on temperature, since superfluid density is a temperature-dependent parameter.

1.2.3 Persistent Currents

When a loop of superconducting material in the normal state is placed in an external magnetic field B_o, the magnetic field penetrates through it as indicated in Fig 1-5 (a). If the temperature of the sample is lowered below T_c, the material becomes superconducting and the magnetic field is expelled from the interior of the wire by surface currents. Upon removal of the external field, the magnetic field that was going through the opening of the loop remains trapped as shown in Fig. 1-5 (b).

Figure 1-5. (a) At $T > T_c$, the magnetic field penetrates a superconductor (b) at $T < T_c$, persistent currents are induced in the loop by the collapsing magnetic field.

5

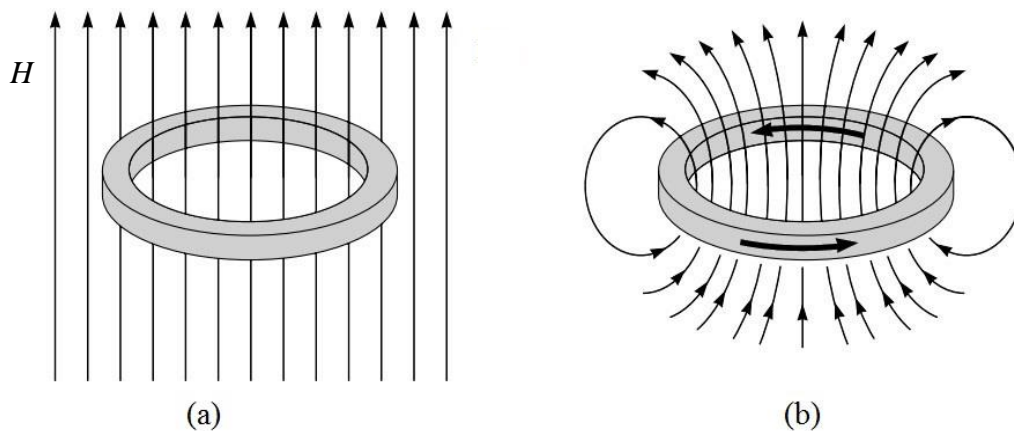Flux trapping has been explained in terms of Faraday's law of induction in (1-5)

$$\oint \boldsymbol{E} \cdot d\boldsymbol{l} = -\frac{d\phi}{dt} \tag{1-5}$$

where $\boldsymbol{E}$ is the electric field along the loop. Before turning off the external field, the magnetic flux inside the loop is Φ. Since the material is in the superconducting state, the electric field in it is zero. Therefore,

$$\oint \boldsymbol{E} \cdot d\boldsymbol{l} = -\frac{d\phi}{dt} = 0 \tag{1-6}$$

indicating that the flux Φ through the loop must remain constant. The trapped magnetic field is due to the current induced by the collapsing external field. This current, called the persistent current, remains without any measurable decay for as long as the loop is superconducting.

1.2.4 Critical Parameters

Superconductivity is a function of three interdependent parameters, namely, critical temperature T_c, critical magnetic field H_c, and critical current density J_c. If any of these limits were exceeded, the superconductor reverts to its non-superconducting state.

(a) Critical temperature T_c

The transition from normal to superconducting state occurs over a small temperature range of width ΔT_c, near the critical temperature T_c. Over ΔT_c, and in the absence of a magnetic field, the sample goes through a second-order phase transition to become superconducting. Typical values of ΔT_c range from 0.5 K to 1 K. Superconductors discovered early on like Nb_3Sn and NbTi have T_c of 9.3 K and 18 K, respectively, but must be cooled to low-temperatures, usually below 5 K, during applications [6]. These are termed as low-temperature superconductors (LTS) and pose cooling challenges in applications. Superconductors with a T_c above 30 K are called high-temperature superconductors (HTS) and thus offer more potential for practical applications due to ease of cooling and their good magnetic properties. As with LTSs, HTSs performs better at temperatures well below their critical temperature. Indeed, HTSs are suitable for use in high magnetic fields in the range of 30 - 40 K where cooling can be achieved with off-the-shelf cryocoolers. For instance, the current-carrying capacity of a YBCO conductor at 20.3 K is 10 times its capacity at 77 K [7]. Fig. 1-6 shows critical temperatures and year of discovery of some LTS and HTS.
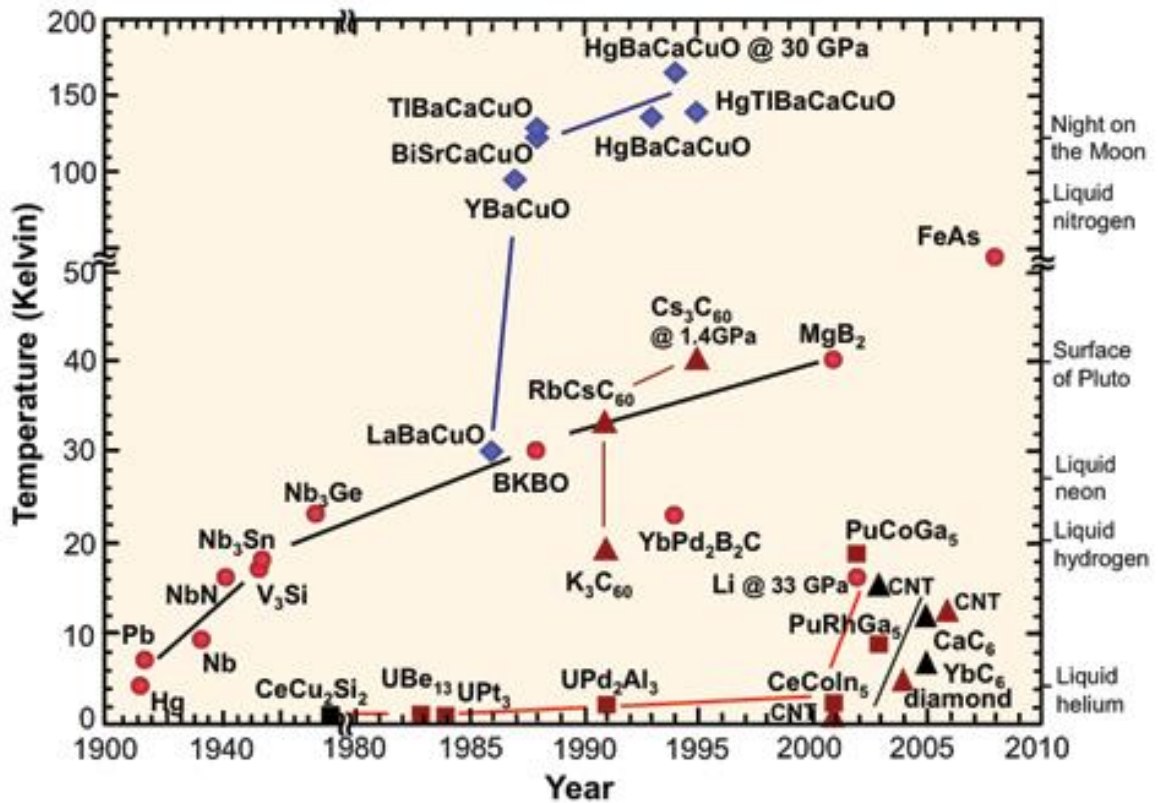
Figure 1-6. Critical temperature and year of discovery of LTS and HTS [8]

(b) Critical magnetic field H_c

The Meissner state breaks when the magnetic field (either external or produced by transport current) is increased beyond a certain value. A first-order phase transition occurs in which the material reverts to its normal state. Such a magnetic field that marks the loss of superconductivity is called the critical magnetic field, H_c. The magnitude of H_c increases as the temperature is decreased. As observed with T_c, the transition between normal and superconducting state occurs over a field transition width of ΔH_c in the vicinity if H_c. Two types of superconductors exist, distinguished by their behavior under applied magnetic fields. The so-called type I superconductors exhibit only one critical field, while type II have a lower and upper critical field H_{c1} and H_{c2}, respectively. Type I and type II superconductors and their properties are explored in section 1.3.

(c) Critical current density J_c

The third critical parameter that determines whether superconductivity occurs, is the maximum dc transport critical current I_c that a superconductor can carry without resistance. Since a current-carrying conductor creates a magnetic field around it, transport current density which creates a

critical magnetic field H_c is termed as critical current, I_c. Just like H_c, the magnitude of I_c gets larger at lower temperatures. In practical applications, critical current I_c, is defined as transport current which causes an induced electric field $E_c = 1$ μV/cm across the superconductor. This criterion was chosen somewhat arbitrarily to provide "reasonably small" electric power dissipation in practical devices [9]. In superconductor applications, it is customary to use critical current density J_c, which is defined as critical current I_c per unit cross-section of the superconductor.

For any superconductor, therefore, superconductivity is bound by three interdependent parameters: critical temperature T_c, critical magnetic field H_c, and critical current density J_c as in Fig. 1-7. If any of these limits were exceeded, the superconductor reverts to its normal, non-superconducting state.
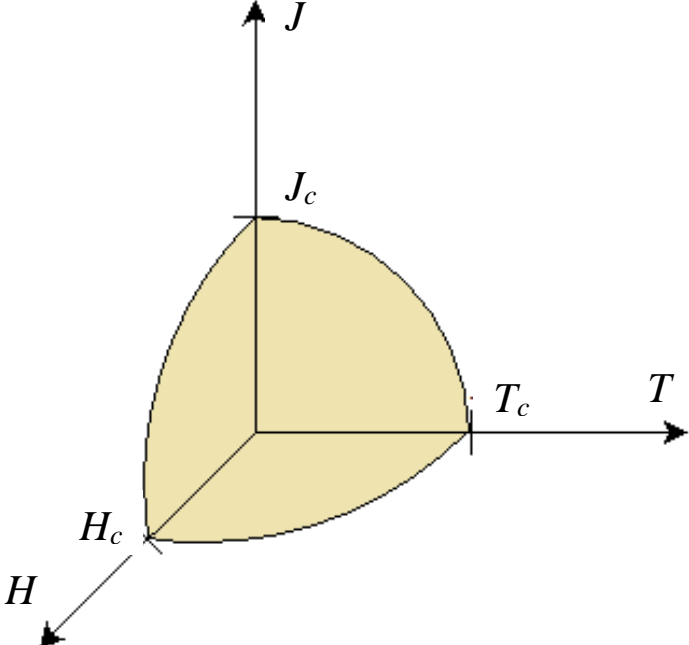
Figure 1-7. A superconducting region bounded by critical temperature, current density and magnetic field [10].

1.3 Classification of superconductors

The first classification of superconductors as LTS and HTS was given in the previous section. Superconductors may be further classified into two types, distinguished by the difference in their behaviour under applied magnetic fields. Two types of superconductors exist, namely type I and Type II superconductors. The criterion used to classify them is the Ginzburg-Landau parameter explained in the next section.

1.3.1 Ginzburg-Landau parameter

When both normal and superconducting phases exist, superconducting properties increase gradually over the length ξ upon travelling from the former to the latter. Therefore, since superconducting electrons form Cooper pairs, the degree of electron pairs order raises over distance ξ. It is also the distance over which a disturbance of a number of superconducting electrons per unit volume propagates. This characteristic length ξ, is called the coherence length. ξ is temperature-dependent such that $\xi \to \infty$ as $T \to T$. Elemental superconductors have ξ on the order of a few thousand angstroms, but HTS have it on the order of 1 to 10 Å. In the interface between a normal and superconducting phase, ξ and penetration depth λ make energy contributions. Free energy density decreases towards the superconducting phase due to an increase in cooper pairs, characterized by ξ. However, there is an increase in free energy due to the transition from the nonmagnetic state to the diamagnetic state, which is characterized by λ. The Ginzburg-Landau parameter κ is the ratio between the two characteristic lengths (1-7).

$$\kappa = \frac{\lambda(T)}{\xi(T)} \tag{1-7}$$

Where κ is dimensionless. κ is a measure of the surface energy of the interface between a normal and a superconducting region. If $\kappa < \frac{1}{\sqrt{2}}$, the surface energy is positive and the superconductor is of type-I. Type-II superconductors have $\kappa > \frac{1}{\sqrt{2}}$ and negative surface energy.

1.3.2 Type I superconductors

Type I superconductors are completely diamagnetic when superconducting. Most are elemental superconductors such as Al, Zn, and Hg, while Nb, V and Tc are some of the few exceptions. Type I have very low critical temperatures and fields, making them less useful in practical applications [5]. Their transition from the normal state to superconducting state occurs abruptly at their critical temperature T_c. In the presence of a critical magnetic field, type I superconductors revert to the normal state. The temperature dependence of the critical field for some type I materials is as shown in Fig.1-8. In the absence of transport current, the critical magnetic field, H_c, at any given temperature T can be approximated by (1-8), where $H_c(0)$ is the asymptotic value of the critical field as T approaches 0 K. The value $H_c(0)$ K gives the highest field at which superconductivity can occur.
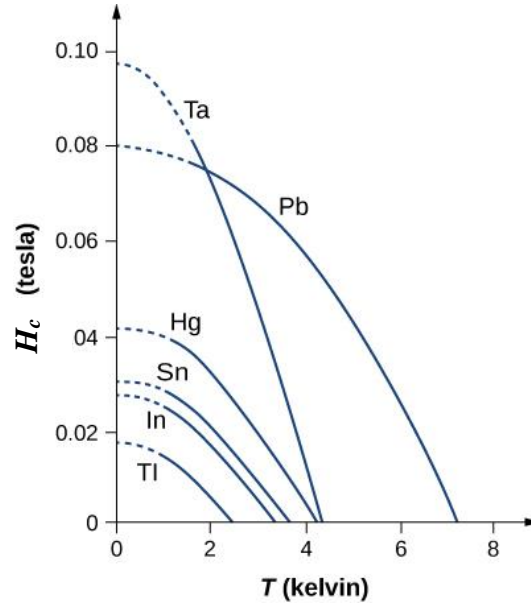
Figure 1-8. Critical Magnetic field as a function of temperature for some type I superconductors [11]

$$H_c(T) = H_c(0)\left[1 - \left(\frac{T}{T_c}\right)^2\right]$$ (1-8)

(a) Critical current density J_c in type I superconductors

If the applied field H is increased, screening currents will increase to ensure that $B = 0$ inside the sample and maintain the Meissner effect. Within λ_L, however, there is an upper limit to the magnitude of shielding currents beyond which the Meissner effect ceases. This limiting magnetic field is H_c, and its corresponding critical current density is J_c. H_c and J_c are related in the London equation (1-1). When conducting transport current in the absence of an external field, the transport current that creates a critical magnetic field equal to H_c is termed as critical current, I_c. The temperature dependence of J_c is given in (1-9), where $J_c(0)$ is the critical current at 0 K.

$$J_c(T) = J_c(0)\left[1 - \left(\frac{T}{T_c}\right)^{\frac{2}{3}}\right]$$ (1-9)

(b) Magnetisation in type I superconductors

When a type I superconducting material is in a magnetic field H, its magnetization is given by (1-10). It acquires no significant free energy and its Gibbs free energy density $G(T, H)$, increases by (1-11).

$$M = -H$$ (1-10)

$$\Delta G = -\mu_0 \int_0^H M \, dH = \frac{\mu_0 H^2}{2} \qquad (1\text{-}11)$$

Figure. 1- 9. Magnetization as a function of H for a type I superconductor. The magnetic field is excluded from the sample volume until $H = H_c$.

If H is increased such that the Gibbs free energy of the sample $G_s(T,H) > G_n(T,O)$ or $\mu_0 H_c^2 > [G_n(T,0) - G_s(T,0)$, the superconductor returns to normal state [5]. This process is reversible.

1.3.3 Type II Superconductors

Type II superconductors include alloys and oxide ceramics and a few elemental superconductors. All HTSs belong to this type.

(a) Critical Current in type-II superconductors

In type II superconductors, J_c is an extrinsic property which significantly determined by defects that are a result of a sample fabrication process.

(b) Magnetisation in type-II superconductors

A type II superconductor is characterised by two critical magnetic fields H_{c1} and H_{c2} shown in the magnetization curve in Fig. 1-10. When the external magnetic field is less than the lower critical field H_{c1}, the material is entirely superconducting and completely diamagnetic ($M = -H$), just like type I superconductors. When the external field exceeds the upper critical field H_{c2}, the flux penetrates completely, and the superconducting state is lost. For fields lying between H_{c1} and H_{c2}, the surface energy is negative, and the material enters a vortex state wherein normal regions appear. Vortices are regions of normal material through which magnetic field quanta

appear when the external field reaches H_{c1} as shown in Fig. 1-9. The vortex regions, also called Abrikosov vortices, are surrounded by supercurrents, generating a quantized magnetic field ($\phi_0 \sim 2.068 x 10^{-15} \, Tm^2$) which decays over a radial distance of λ [5]. More vortices occur as the field is increased, resulting in an increase in vortex density. Part of the material remains superconducting.
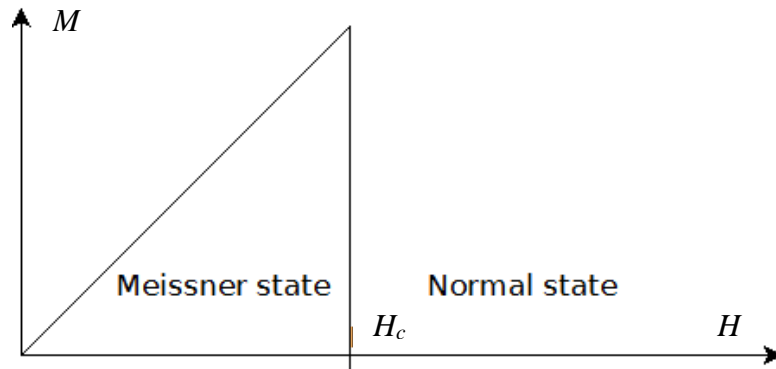

(a)

(b)
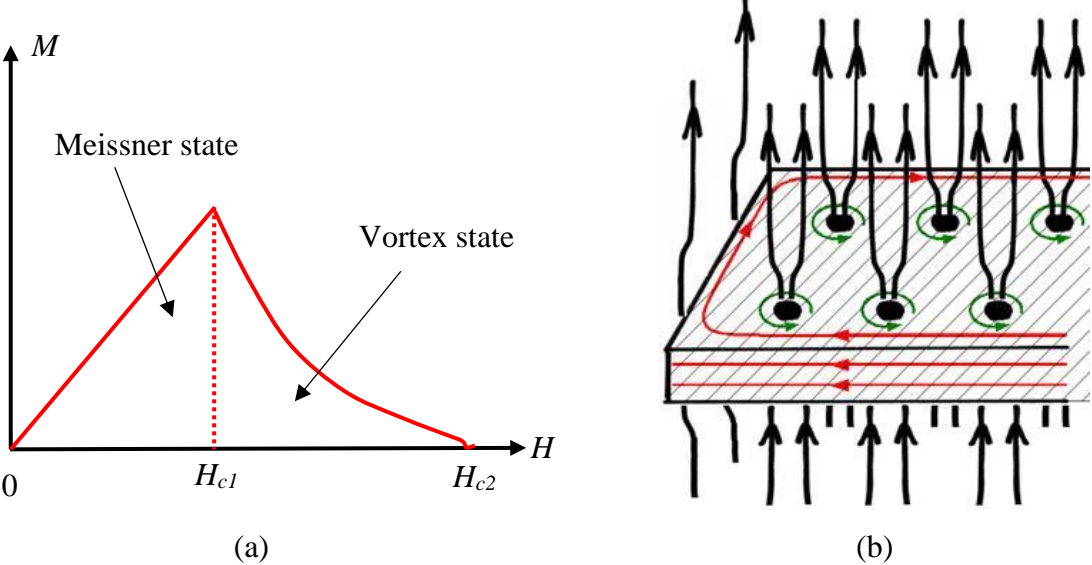
Figure 1-10. Magnetization as a function of H for a type II superconductor (a). The magnetic field is excluded completely from the sample volume until $H = H_c$. Vortex regions oriented parallel to the applied field, with quantized flux at the center (b) [12].

Type II superconductors have much higher critical temperatures and their B_{c2} values are much higher than critical fields of type I superconductors as depicted in table 1. They are therefore suitable for practical application. It is, however, important to ensure the flux lines in Fig. 1-10 do not move about as moving flux would generate a dissipative electric field. This important task of flux pinning is covered in the next section.

Table I-1. Critical temperatures and critical magnetic fields (B_0) of some type I and type II superconductors

Type	Superconductor	T_c (K)	B_0 (T)
I	Al	1.196	0.0105
II	Nb	9.26	0.1991
II	NbTi	9.3	15
II	NbSn	18.0	32.4

1.4 Bulk high-temperature superconductors

This section focuses on electric and magnetic properties of bulk HTS, also called trapped-field magnets (TFMs). Properties that make bulk HTS useful are described in the preceding sections, while subsequent sections cover classical models used to estimate trapped fields in bulk samples. The last section explores bulk HTS magnetization methods.

1.4.1 Bulk HTS and HTS wires and tapes

To date, superconductors have largely been used as conductors in the form of wires and tapes. The most studied conductor and leading candidate in HTS applications is $Bi_2Sr_2CaCu_2O_{8+\delta}$ (Bi-2212) from the $Bi_2Sr_2Ca_{n-1}Cu_nO_{2n+4+x}$ family (n = 1, 2, 3). This cuprate has a T_c of 96 K, and H_{c2} above 100 T at 4.2 K. It has a two-dimensional layer structure as shown in Fig. 1-11, with superconductivity taking place in the copper-oxide planes. The bonding force between the Bi-O layers is small and thus allows the Bi-2212 to be easily drawn into tapes using the powder-in-tube method. Although having a low J_c in the presence of a magnetic field at 77 K, excellent current densities of 7100 A/mm^2 in self-field and 3500 A/mm^2 in 10 T were reported at 4.2 K [13]. BSCCO has therefore been used in demonstrator motors and generators, fault current limiters and high-field magnets. The high cost of the currently available HTS wire [14] is one of the major factors limiting the commercialization of these devices.
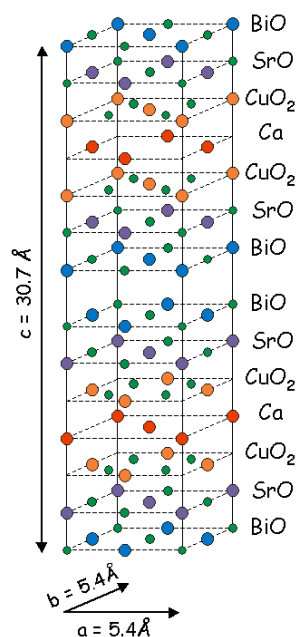
Figure 1-11. Crystal structure of Bi-2212. Superconductivity taking place in the copper-oxide planes [15]

Some superconductors with excellent properties, have a brittle ceramic nature and cannot be readily drawn into conductors. These are used in bulk form. Bulks can be fabricated cheaply and simply, unlike capital-intensive, multi-step processes used to make wires, tape and thin films. Bulk superconductors are fabricated as single crystals through a melt-textured process that involves seeding. With improved flux pinning, bulks can trap a high, and stable magnetic field which is useful in engineering applications. As discussed earlier, type II superconductors under which HTS fall, are more suited to applications due to their higher critical fields and critical temperatures. Most HTS are cuprates. $GdBa_2Cu_3 O_{7-\delta}$, (GdBCO) with $T_c = 92$ K and $YBa_2Cu_3O_{7-\delta}$ (YBCO) with $T_c = 91$ K are most common HTS used in bulk form. They are collectively called $(RE)Ba_2Cu_3O_{7-\delta}$ (REBCO) (RE = rare earth element or Y). REBCO bulk superconductors are renowned for their high magnetic flux trapping capabilities as demonstrated by a trapped field of 17.6 T in a GdBCO sample at 29 K [16]. A crystal structure of GdBCO is shown in Fig. 1-12
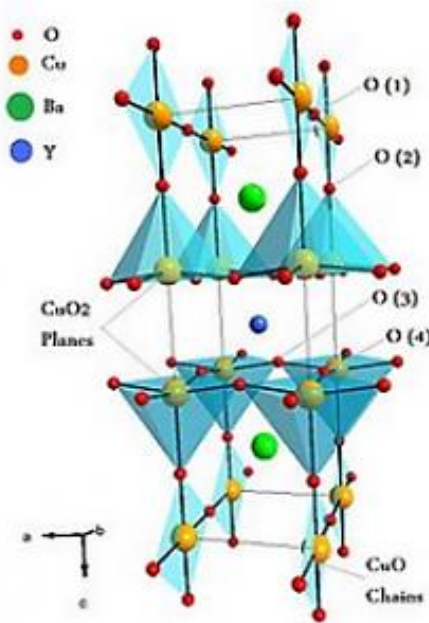
Figure 1-12. Crystal structure of GdBCO. Superconductivity taking place in the copper-oxide planes

Just as with BSCCO, superconductivity takes place in the copper-oxide planes. Another superconductor used in bulk form is MgB_2 with $T_c = 39$ K, pursued its low cost, lightweight, and good J_c homogeneity.

1.4.2 Flux pinning

In the absence of the pinning centers, flux lines would move freely to achieve a uniform density (Abrikosov lattice) when the conductor is in vortex state. From amperes law, a current flow must

correspond to a magnetic field gradient. A uniform flux line density results in a magnetic field gradient of zero. Therefore, the only way to establish and sustain a flux gradient is by pinning flux lines by impurities or other defects. Flux pinning or quantum locking is a mechanism whereby flux pinning centers are added to a superconductor to prevent movement of flux lines under Lorentz force. Flux pinning sites are therefore essential to the sustenance of high **transport currents** in the superconducting state. Pinning centers used are such as dislocations, precipitates, and grain boundaries. Magnetic flux pass through these regions since no Meissner effect occurs in them.

As both a current and a field are present, the current exerts a Lorentz force on the magnetic flux. The maximum pinning force is given by (1-12),

$$\boldsymbol{F}_p = \boldsymbol{J}_c \times \boldsymbol{B} \tag{1-12}$$

where J_c is the critical density at $T = 0$ and B is the local area density of the flux lines [5]. At a field referred to as the irreversibility field, flux break pinning center bonds and their motion lead to the loss of superconductivity.

1.4.3 Bean Model

The most popular models used to describe irreversible magnetization behavior of type II superconductors are the Bean or critical-state model and variations such as the Kim-Anderson model. The following assumptions are made for the Bean model, for an infinitely thin disc in a static, non-linear case;
   (a) The relative permeability of a type II conductor is 1.
   (b) Any electromotive force in the region penetrated by external flux lines induces a critical current.
   (c) a constant J_c, that is, there is no field dependence of J_c and $J = J_c$ at vortices.
   (d) Areas with no flux penetration have $J = 0$.

(a) Bean model applied to trapped field in cylindrical bulks

Based on the Bean model, the peak trapped magnetic flux density, B_{trap}, at the center of the top surface of a single-grain bulk superconductor, oriented with its thickness parallel to the c-axis, due to an induced, persistent supercurrent is given in its simplest form by (1-13).

$$B_{trap} = k\mu_o J_c a \qquad (1\text{-}13)$$

where μ_0 is the permeability of free space, J_c is the critical current density of the superconducting material and a is the radius of the sample. k is a correction factor to the simple Bean (slab) approximation due to the finite thickness t, of a disk-shaped bulk superconductor sample. Based on the Biot-Savart law, k given by (1-14)

$$k = \frac{t}{2a} \ln\left(\frac{a}{t} + \sqrt{1 + \left(\frac{a}{t}\right)^2} \right) \qquad (1\text{-}14)$$

Equation (1-13) shows that the magnetization of a bulk increases with sample volume. Indeed, another way of increasing trapped flux is by increasing the thickness to increase the aspect ratio. The trapped field, however, was found to saturate when the thickness was comparable to the diameter or the length of the edge in case of a square sample. The field trapping ability of a bulk superconductor can also be improved by enhancing the critical current density through improved flux pinning and increased sample homogeneity. The magnitude of the trapped field decreases with increasing distance z from the top surface along the c-axis. This decay is given by the following equation (1-15) [17].

$$B_z = \frac{\mu_0 J_c}{2} \left((z + t) \ln\frac{a + \sqrt{a^2 + (z + t)^2}}{z + t} - z \ln\frac{a + \sqrt{a^2 + z^2}}{z} \right) \qquad (1\text{-}15)$$

1.4.4 Magnetization of bulk superconductors

There are two ways of magnetizing bulk superconductors, namely field cooling magnetization (FCM) and zero-field cooling magnetization (ZFC). In FCM, the bulk superconductor is cooled below its critical temperature in the presence of the magnetizing field. Through this method, HTS bulks can trap significantly high flux as this method can fully magnetize a bulk superconductor to its critical magnetic field. The required magnetizing flux has to be higher or equal to the desired trapped flux. The magnetizing flux is usually provided by a superconducting magnet.

With ZFC, the bulk superconductor is cooled below its critical temperature before a magnetic field is applied. This method requires a magnetic field at least 2 times the desired trapped field. Pulsed-field magnetization (PFM) is a ZFC magnetization method wherein bulk superconductors are magnetized by application of a large, pulsed magnetic field with a timescale on the order of

milliseconds. The coil current can be as high as 3 kA, creating a field of 10 T within 6.8 ms. As PFM involves rapid magnetic flux motion (flux penetration and relaxation), a significant amount of heat is generated, raising the temperature of the bulk and thereby reducing J_c. As a result, trapped fields are lower than the theoretical maximum and generally lower than those attained via FCM [18]. PFM requires a magnetizing flux at least two times the required trapped flux. Compared to FCM, PFM is inexpensive to deploy, and bulks can sometimes be easily magnetized in-situ. As a disadvantage, thanks to momentary hoop stress, a lot of microcracks appear inside the bulk materials which causes degradation of trapped flux as a function of the number of PFM. The unique proposal by employing a single pulse PFM exhibited considerable enhancement of flux trapping [19].

When magnetized by field cooling (FC) magnetization or pulsed-field magnetisation (PFM), bulks like GdBCO and YBCO can trap magnetic fields that are orders of magnitude higher than conventional permanent magnets (PM) [16]. Therefore, with sufficient cooling, bulk HTS can be used as trapped field magnets in lieu of permanent magnets. Unlike the heavily coated conductors, the engineering J_c of TFMs is higher than those of coated conductors [20]. Another advantage of bulks is that they do not need a connection to a power supply to retain their magnetic flux, unlike HTS electromagnets. This eliminates the thermal invasion from the power current leads.

Despite their high field potential, only a few motors and generators have been designed with bulks due to a number of technical challenges [21]. One of the drawbacks of using bulks is that it is challenging to magnetize them in-situ. FC magnetization makes it is difficult to magnetize bulks in-situ since an external flux source is required. PFM, on the other hand, involves fast-flux dynamics that reduce the trapped flux, while the successive application of pulsed-field causes mechanical damage due to hoop stress. Moreover, to magnetize a bulk superconductor to a desired magnetic field value, PFM requires a magnetic field twice the desired field. One other challenge that also discouraged some researchers from pursuing bulk HTS machines is the possibility of bulk demagnetization due to cross-fields.

1.5 Background on synchronous electric motors

1.5.1 Construction

Electric motors are the most commonly electric components used in industry consuming about 65-70 % of electric power produced [22]. The majority of electric motors used in industry are radial-gap synchronous and induction motors. The main components of a synchronous motor are a three-phase ac armature winding and a field winding which is supplied by a separate dc source Fig. 1-13. While the two windings are interchangeable, the most common configuration is the ac armature winding on the stator, while the field winding on the rotor. In the case of PM synchronous machines field windings on the rotor are replaced by permanent magnets (PMs). Conventional motors have a laminated iron core on both the rotor and stator.
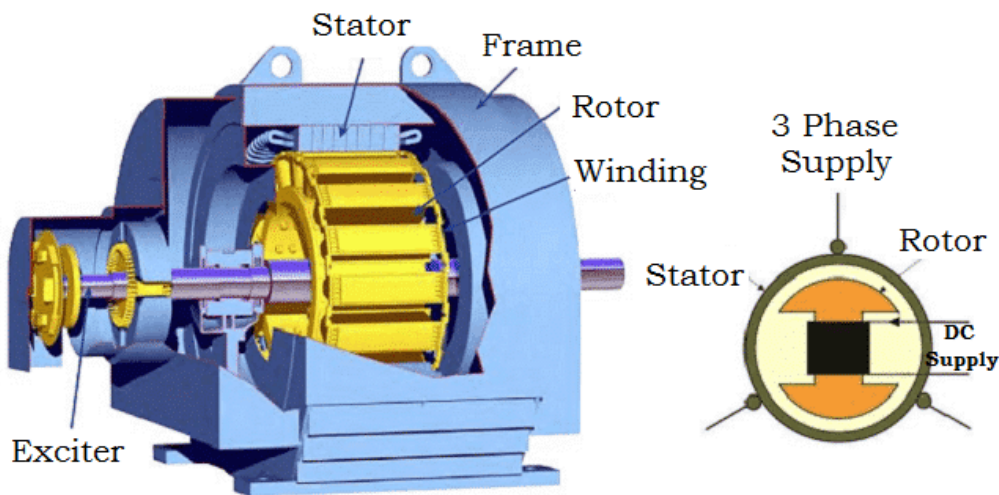
Figure 1-13. Radial-gap synchronous machine [23]

In general, the power produced by a radial gap rotating machine is given by (1-16)

$$P = knABD^2L \qquad (1\text{-}16)$$

where k is a design specific constant, A is the electric loading, B the magnetic loading, D the machine diameter, L is the machine active length and n the rotating speed. Equation (1-16) indicates that the power density of a machine of any given size can be increased electromagnetically by increasing A and/or B or by increasing n, the speed. The magnitude of B in high flux density Nd-Fe-B is about 1 T, while A in copper wires is limited to avoid excessive resistive heating in the copper armature in the stator. The physical dimensions of an electric motor

are primarily determined by the required torque. Torque in a conventional radial gap motor is given by (1-17)

$$T = 2\pi R^2 LAB \qquad (1\text{-}17)$$

where R and L are the radius and length of the rotor respectively. The torque can be increased by increasing the radius or length of the rotor, widening or elongating it or by increasing the electromagnetic shear stress.

Radial synchronous HTS machine rotors can be classified, depending on the magnetic properties of the rotor and stator core as iron-cored or air-cored topologies. Conventional machines use an iron core to carry, guide and shield magnetic fields. Iron-cored rotors have a high moment of inertia due to the presence of heavy iron, which is beneficial when the machine is used on land in power utilities. Less magnetomotive force to achieve a given magnetic flux density and thus require short wire length. Iron also provides a sturdy structure to support excitation coils as they are subjected to centrifugal forces. Iron-cored rotors, however, suffer from core losses, while their high moment inertia is undesirable in applications that require light-weight motors or involve high accelerations. Air-cored rotors have also been developed to offer light and compact alternatives suitable for applications in naval and aerospace industries. When used with a non-magnetic teeth stator, the air-gap field can be increased without saturation and core losses. A conventional stator has stranded copper winding located between magnetic teeth. Designs employ non-magnetic teeth and a back iron as a flux return path, resulting in a high field stator topology that allows high air gap magnetic flux densities.

1.5.2 Rotating machine characterization

In the typical tests and characterisation of electric rotating machines, a variety of tests are conducted, and tests described hereunder are only a few of many characterization tests conducted. The IEEE body has a framework that informs on various testing techniques and procedures [24]. This section gives a background of the no-load tests and core loss.

(a) No-load test

A no-load allows for the determination of a no-load characteristic which gives the relationship between the rotational steep and the induced emf E, at different magnetic fields. In the case of wound-filed machines, the field is changed by varying the field current I_f pressed as (1-18). The

characteristic curve is useful in assessing for the occurrence of saturation in ferromagnetic armatures as shown in Fig. 1-12. It is also used for determining the relation between the induced voltage and field current.
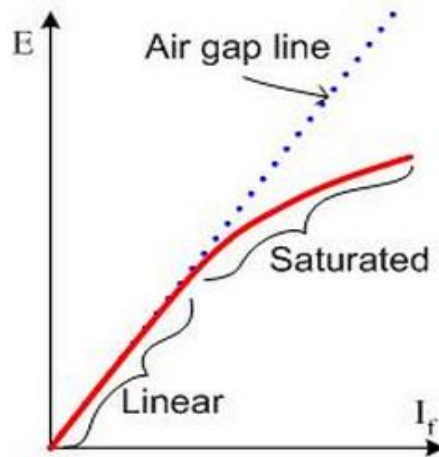
$$E = f(I_f)$$ (1-18)

Figure. 1-12 No-load characteristic curve.

(b) Core loss

Core or iron loss is one of the major causes of heating in rotating machines and amount to 20-25 % of total losses [25]. Determining core loss is therefore important in efficiency optimization of high-power density machines. Core loss is divided into hysteresis, eddy current and excess losses (also called anomalous losses). Hysteresis loss is due to the changing magnetic field polarity which results in magnetic domain wall movement. Hysteresis loss depends on the material and the total flux density in it. Eddy currents are circulating currents induced in the magnetic material of the armature core by a time-varying magnetic field. The current is proportional to the total flux density, its frequency and the size of its flow path, but inversely proportional to the resistivity of the material [26]. Such currents result in joule heating. Excess loss is due to high-frequency micro-currents [27].

Core loss, P, is often estimated using models such as the Steinmetz and Bertotti models. The Bertotti model in (1) considers specific core loss (watts per kilogram) as a sum of hysteresis, eddy current and excess losses [28].

$$P = k_{hyst}B^{\alpha}f + k_{eddy}B^2f^2 + k_{excess}B^{1.5}f^{1.5}$$ (1-19)

where the three terms represent hysteresis, eddy current, and excess loss. f and B are the field excitation frequency and peak flux density, respectively, while α, k_{hyst}, k_{eddy} and k_{excess} are coefficients that originate from the material. Equation (1-19) is used under the assumptions that

20

the air-gap field is sinusoidal, the magnetic flux density of 1 T is not exceeded, and the hysteresis loop is under static condition [29]. For a non-sinusoidal air-gap flux distribution such as that of the HTS bulk poles considered in this paper, total core loss is taken as a combination of losses due to all harmonics in the air-gap flux. Even though rotational field effects are not accounted for, (1) indicates that core losses increase with increasing magnetic flux and magnetic flux harmonics.

Core losses can be experimentally determined via separate drive, electric input, retardation or heat transfer method. In the separate drive method, the no-load power consumption of the tested machine is measured at different speeds and at different magnetic flux densities. Friction and windage losses are then subtracted to remain with core loss. Friction and windage account for losses due to all mechanical components connected to the rotor shaft and resistance of air to rotor rotation. These losses are determined separately as the total electric input, less mechanical losses such as from pony motor and gearbox, while the machine is driven at zero field excitation. Generally, frictional losses are proportional to the rotor speed while windage losses are proportional to the cube of the rotor speed. The separate drive method is used in this thesis, in chapter V.

1.6 HTS rotating machines

1.6.1 Merits of HTS motors

Motor size and weight are limiting factors in electric propulsion systems. Ship electric propulsion specifically requires motors with high-torque capability. Conventional motors suffer from iron saturation. The magnetic loading of PM machines cannot be raised as the peak magnetic flux of Nd-Fe-B permanent magnets is limited to about 1.5 - 2 T [30]. Moreover, the electric loading cannot be improved as the current carrying capacity of copper wire is also limited (2000 A/cm^2 for a water-cooled wire at 300 K). All These limitations make it challenging to develop high power density motors. Motors would be significantly bulky if built with conventional technology. The use of HTS rotating machines can address most of these shortcomings.

High-temperature superconductors have allowed for the design and development of compact motors with high power and torque density and efficiency. This is easily achieved by raising both the electric and magnetic loadings using HTS conductors or by replacing PM with bulk HTS. In the case of bulk HTS, the total magnetic flux, ϕ_T, which is the surface integral of magnetic flux,

is important in motors and generators [31]. Synchronous machines employing HTS are compact, up to 4-5 times lighter than conventional machines [32]. The specific output power of a bulk HTS machine operating at 77 K is about 3-6 times that of a conventional machine [33]. Fig.1-12 captures the size and weight reduction achieved by an HTS motor relative to a conventional motor with the same rating. This particular motor employs coils of HTS wire that can carry 150 times more current than copper wires of similar size. It weighs less than half the size and weight of a conventional motor and could significantly reduce ship weight, making it more fuel-efficient while freeing up space.
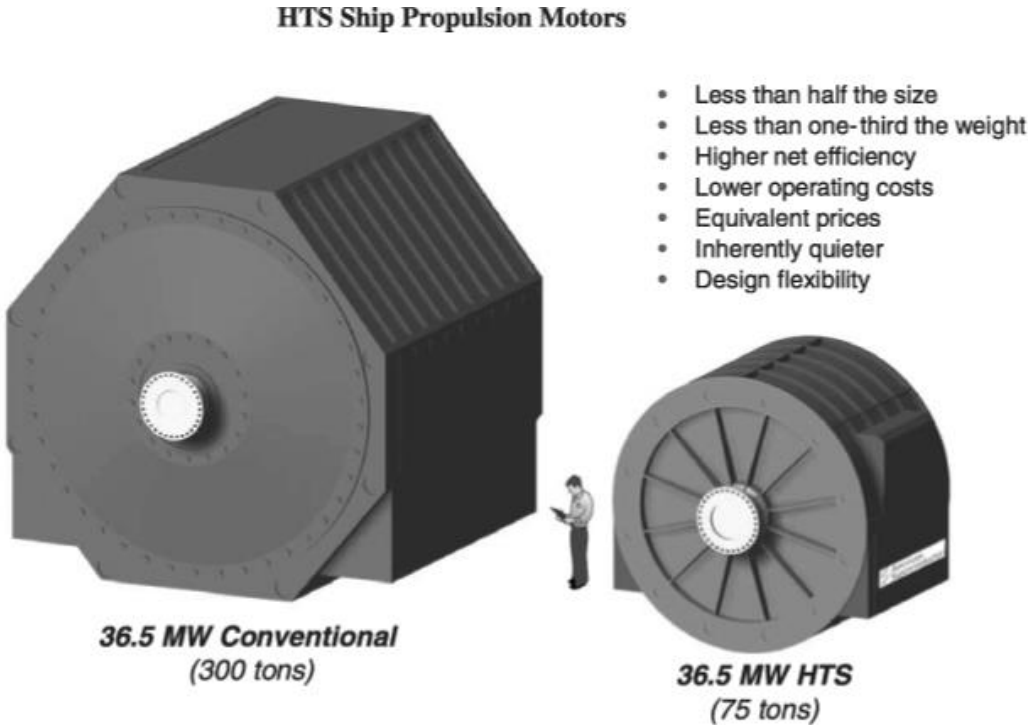
Figure 1-13. Size and weight reduction by using HTS machines [34]

Superconductors do not suffer from losses when conducting dc currents. Thus, rotating machines are designed with superconducting dc field components, while ac components such as the armature comprise of conventional conductors. The structure of synchronous machines renders them suitable for HTS technology applications since HTS dc field coils or bulk HTS can be used to generate high magnetic flux. In terms of ship propulsion, HTS synchronous motors offer also more benefits due to their high energy efficiency, the low nominal rate of revolutions and good torque/speed characteristics. Moreover, they can be used in a direct drive propulsion system, leading to an efficient drive train with sensitive control.

Due to ac losses, two types of superconducting machines have emerged namely, partly superconducting and fully superconducting motors. Partly superconducting motors have one

superconducting component, such as a superconducting rotor bulk HTS as field poles. Fully superconducting machines utilize superconductors on both the rotor and stator.

1.6.2 HTS motors for ship propulsion

Tightening emission legislations and increasing energy demand, require us to reduce carbon emissions, improve fuel efficiency and develop new innovative power systems. Ships produce a significant amount of hazardous sulfur oxides, nitrogen oxides and particulate matter emissions. A study published in 2014 estimated emissions from international shipping at 2.2 % of global total CO_2 emissions [35]. Electric ship propulsion was therefore introduced to in an attempt to decarbonize the maritime industry by promoting energy efficiency. In electric propulsion, a gas turbine, diesel generator or both are used to generate electricity which is then used to power propulsion motors, auxiliary machinery and hotel loads. Electric propulsion was used in ice breakers of the 20th century that utilized DC motors to split ice with back and forth motion [36].

The advent of modern electric ship propulsion is, however, usually credited to the retrofitting of Queen Elizabeth II with diesel-electric propulsion in 1988. Although the initial aim was to reduce ship fuel consumption, environmental emissions and improve efficiency, the advance in rotating machines, power electronics, energy storage and control enabled electric propulsion to offer more benefits such as flexibility in ship design and components arrangement, reduced maintenance, improved maneuverability and reduced lifecycle costs. Apart from the abovementioned benefits, the use of superconducting ship propulsion motors offers high power density, high efficiency and low structural noise [37]. Since superconductors suffer from significant losses under ac currents and magnetic fields, most superconducting propulsion demonstrator motors are designed with superconducting dc field components, while ac components such as the armature is made of conventional conductors.

1.6.3 Challenges facing HTS motors

HTS machines are a new technology that is not yet commercial, so HTS technology is still costly than that for a conventional machine. Therefore, further prototyping and testing efforts are necessary to prove the reliability and appeal of this new technology.

(a) Cooling systems

The reliability of HTS machine cooling systems is still low and this challenge is deemed as one of the major hindrances to the adoption of HTS motors for ship propulsion. Moreover, the cost of cryocoolers is still prohibitively high

(b) In-situ magnetisation

The high flux trapping capability of bulks has to a large extent been overlooked despite significant research and development efforts of wires and tapes [21]. Although bulk HTS are relatively cheaper and can trap large magnetic flux, they have largely been overlooked in electrical machine applications due to fear of demagnetization. Another main challenge hindering the use of bulks is the difficulty of magnetizing bulks in-situ since an external magnetic field is required. For a rotor with bulk HTS, it will have to be extracted from the stator to be magnetized. Alternatively, a provision for PFM such as vortex magnetizing coils has to be incorporated into the machine design. The Performance of PFM is still comparatively low, however.

(c) Quench in HTS machines

HTS materials have a small but finite resistivity in normal operating conditions. This resistivity increases non-linearly with increasing temperature and current. Thus, the resistivity of HTS field coils increases significantly when either the temperature or current increases. In the event that the cooling system fails or the current raised to the certain quench current, the resulting temperature of the HTS winding leads to the loss of superconductivity, termed as quenching. Quenching damages HTS windings. Electric machines experience current and temperature transients after disturbances. HTS machines, therefore, require a quench detection system that de-energize the machine to avoid damage. Bulk HTS machine quench without suffering damage. Moreover, they are not liable to current-initiated quenching.

1.7 Thermosyphon cooling system for HTS machines

A cryogenic cooling system is pivotal to the superconductor technology application. An HTS motor or generator differs from a conventional one in that it would have a superconducting rotor or stator or both, cooled by a cryogenic cooling system. At the heart of the cooling system is a cryocooler (cold head), the most common of which is the pulse tube and Gifford-McMahon (GM) cryocooler. The cooling methods employed are conduction cooling or forced cryogenic gas circulation. In a

thermosyphon-cooled machine, superconducting field coils or bulks are installed on the periphery of an evaporator which is located in the rotor cryostat as shown in Fig1-13. An adiabatic flow tube is used to supply the evaporator with liquid cryogen from the condenser located outside the rotor. Most HTS rotating machines designed thus far have superconducting rotors that operate at 25-68 K [38]. A rotary seal to enable relative motion between the stationary cryocooler and the rotor is indispensable.
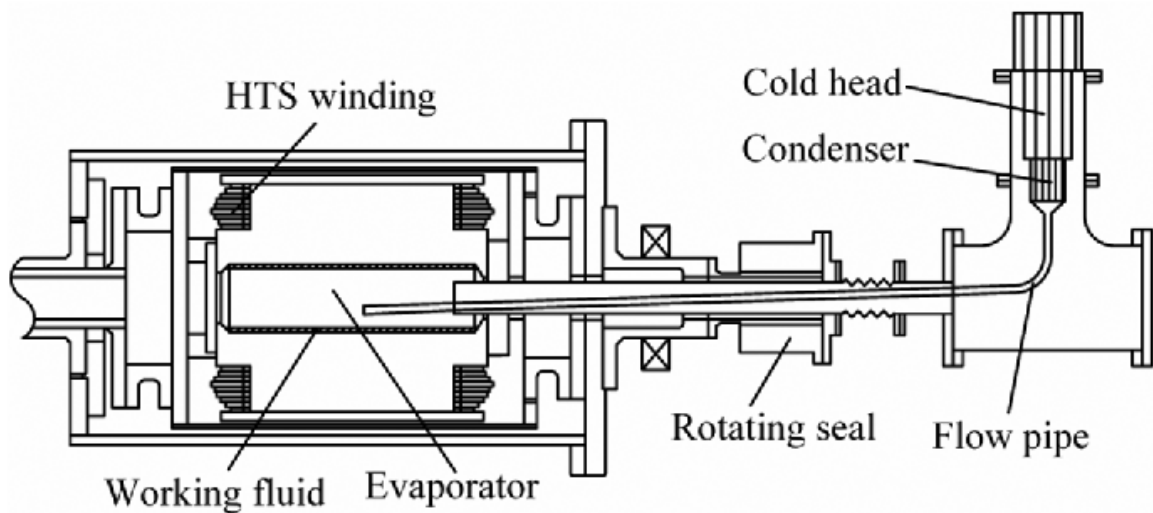

Figure 1-14. A thermosyphon-cooled rotating machine [39].

This thermosyphon is based on the latent heat of the working fluid, therefore the operating temperature depends on the working fluid used. Neon and nitrogen are the most commonly used working fluids in HTS machine thermosyphon cooling systems. Neon is used for high field applications (30 K to 40 K) whereas nitrogen suits low-field applications at around 77 K.

1.8 Aims of present research and scope of the investigation

HTS motors have great potential in the application as ship propulsion motors. Most of HTS machines designed and developed so far employ superconducting wires in spite of their high production costs low heat capacity and high ac losses. Only a few projects have sought to leverage the high flux trapping capability of bulk HTS due to fear of demagnetization and difficulties related to bulk magnetization. The low reliability of HTS cooling systems has also remained a hindrance to the adoption of HTS motors in ship propulsion. Additionally, the cost of HTS machines remains prohibitive compared to conventional technology. This research work aims to address some of these challenges.

In order to explore the potential of bulk HTS machines and validate the technologies required to develop them, while addressing challenges above, a 30-kW partially superconducting bulk HTS motor was designed, developed and tested. The machine is cooled with a neon thermosyphon cooling system that not only has a high heat transfer rate but is also reliable as it has no moving parts. Prior to the development of the 30-kW machine, a standalone thermosyphon cooling system was designed, developed and tested. The aim was to investigate its cooling performance and applicability to bulk HTS machines. This research covers the part of the study where a thermal model was developed from experimental results and used to estimate the temperature distribution of the thermosyphon evaporator.

1.9 Significance of this work

Although superconductivity was discovered over 100 years ago, and its potential in the realm of superconducting machinery is yet to be tapped. This research, therefore, has significance for researchers and the electrical machines industry alike, as far as viability of superconducting machinery is concerned. Both the superconducting rotor and cooling system of the prototype are unique in design. Moreover, the results obtained during testing prove that bulk HTS machines operate without suffering demagnetization as previously feared by most researchers. These aspects contribute to the creation of new knowledge on superconducting machines and should encourage researchers and industries to pursue bulk HTS rotating machines.

Chapter II Literature Study

This Chapter covers a review of the development of bulk HTS materials as well as bulk HTS superconducting machines, and the use of cryogenic thermosyphon cooling systems.

2.1 Bulk HTS development

Through research, properties of bulk HTS continue to improve. Trapped fields have been enhanced due to the introduction of strong pinning centers and the improvement in crystal growth techniques, which results in increased critical current densities. The primary reasons why they are being pursued are their large transport current capacity even under strong magnetic fields and their high trapped field ability. In addition, HTS bulks require no metal substrates like HTS tapes, leading to a highly effective critical current density (J_c) [20]. The main areas of application of bulk were summarized in [21] as;

- Flux shielding application where the diamagnetic behavior of type II superconductors is used instead of expensive specialist alloys.
- Flux pinning
- Flux trapping application such as in medical magnetic drug delivery and in low-cost and portable MRI. Bulks are also considered for applications as permanent magnets in a lightweight, high power machines such as in aviation.

The research and development in REBCO bulks have especially been impressive. Standard (non-irradiated) bulk superconductors exhibited J_cs of 5 x 10^4 A/cm^2 at 1 T and 77K, resulting in trapped fields in the range of 1 T and 1.5 T for YBCO and over 2 T for (RE)BCO. Bulk HTS made from YBCO achieve critical current densities of up to 325 kA/cm2, at 77 K in the presence fields of 1T. Mass-produced YBCO bulks of 2 cm diameter can achieve current densities of 300 kA/cm2, trapping a field B_{trap} of 2.3 T at the surface [17]. Nippon Steel Corporation (NSC) has been developing high J_c large grain YBCO and LRE-Ba-Cu-O (LRE: light rare elements = Nd, Sm, Eu, Gd) bulks by controlling their microstructure. Their conclusion was that LRE-Ba-Cu-O could trap higher magnetic flux then YBCO. Specifically, a ϕ60 mm, 20 mm thick GdBCO bulk was found to have trapped a flux of 2 T at 77 K, two times higher than that of a YBCO bulk of the same dimensions [40]. GdBCO bulks of 20 mm diameter were also reported to have trapped up to 2 T at 77 K, while a 65 mm diameter can trap up to 3 T at this temperature [41]. The highest recorded trapped magnetic field is 17.6 T that was achieved in a 25 mm diameter Gd-Ba-Cu-O bulk at 26

K [16]. Apart from REBCO, research on MgB$_2$ bulks has been widely conducted and a trapped field of 5.4 T has been reported [21].

As for magnetization, PFM is still far less effective than FC magnetization. The main reason for low trapped fields is the large temperature rise due to rapid flux motions. Current research is focused on employing multi-pulse techniques to reduce temperature rise [42]. The phenomenon of giant field leap is also being used to enhance field trapping during PFM. The highest PFM trapped field to date is 5.2 T obtained in a 45 mm GdBCO bulk at 30 K [43].

2.1.1 Challenges in bulk HTS research

There are challenges researchers are attempting to solve. At low temperatures, flux trapping capability of REBCO bulks as obtained from estimates of critical current density, J_c, is very high. However, the electromagnetic force the bulk is subjected to is proportional to the trapped field resulting in fracture of these ceramics during high flux magnetization. Therefore, the pursuit of high trapped fields is paralleled by efforts to mechanically reinforce bulks. At the moment, mechanical properties are the limiting factor for high fields greater than 10 T. So far, bulks have been reinforced using resin impregnation, carbon-fiber wrapping and shrink fit steel [44]. A compositional gradient technique was also used to improve mechanical properties in large-sized bulks.

Another challenge in the application of bulk HTS is demagnetization. A trapped field in a bulk HTS decays when subjected to a cyclical transverse variable magnetic field. The prospect of demagnetization by AC armature field perturbations has discouraged most researchers from pursuing bulk HTS rotating machines. Jean-Francois studied the long-term influence of small amplitude transverse ac magnetic fields on GdBCO bulk [45]. In a study to suppress decay using HTS shielding coils wound around a bulk with $B_{trap} = 1.22\ T$, $J_c = 7.37\ \text{x} \frac{10^7 A}{m^2}$ at 77 K, the trapped field decay was found to reduce significantly as the number of shielding coils increase [46]. Flux decay in the application such as motors can be avoided by operating at 30 K. The J_c of current HTS materials deteriorates significantly and become anisotropic at 77 K [33].

2.2 HTS machines development testing

Research and prototyping of superconducting machines began in the 1960s following the development of metal (LTS) superconducting wires at Westinghouse. Between 1978 and 1997,

superconducting machines using NbTi were developed in Japan, America and Europe. LTS superconductors were cooled using liquid helium [47]. Due to significant ac loss in superconducting wires, the majority of superconducting rotating machines developed early on were dc machines. One such R&D case was the Super-GM project which started in 1988 in Japan, where a 70 MW superconducting generator with three different rotors employing three different NbTi field windings was tested [48]. Although the tests were considered successful, yielding an efficiency of up 98.3 %, this and similar projects listed in table 2-1 were discontinued. LTS technologies operated at liquid helium temperatures (about 4.2 K) which are challenging to maintain. Moreover, LTS wires have a small operating temperature range of 4.2 K to 5.5 K which required stringent stability [49]. As a result, cooling systems were complex, unreliable and inefficient [32]. As a result, LTS machines were not commercialized.

Table 2-1. Some of the superconducting rotating machines using LTS.

Year Tested	Speed (rpm)	Power (kW)	Conductor	Coolant	Country
1978	3600	20 000	NbTi	Liquid He	USA [50]
1980	7000	20 000	NbTi &Nb$_3$Sn	Liquid He	USA [50]
1978	3000	18	NbTi	Liquid He	USA [51]
1997	3600	78 700	NbTi	Liquid He	Japan [52]

High-temperature superconductors (HTS) breathed new life into superconducting machines research. HTS machines have a more practical appeal due to their ease of cooling as they have high operating temperature range between 25 K – 77 K. HTS materials also have a heat capacity about two orders of magnitude higher than compared to LTS, which enables them to better withstand thermal transients. The 36.5 MW HTS marine propulsion motor, motor constructed and tested by AMSC in 2007 remains one of the largest in terms of power rating. It featured an HTS field winding on the rotor which was cooled by gaseous helium supplied from a stationary cooling unit through a seal assembly. Its non-magnetic stator was cooled by a dielectric fluid [53]. Between 2010 and 2013, motors were constructed utilizing mainly BSCCO conductors. A variety of cooling systems from gaseous helium to neon thermosyphon and liquid nitrogen were employed [49].

2.2.1 HTS synchronous machines

Synchronous motors offer high energy efficiency, low nominal speed and good torque/speed characteristics, so they are preferred in industry, and ships for direct drive propulsion system [54]. Therefore, following advancements in power electronics and the development of variable speed drives, the development of HTS synchronous motors for ship propulsion started [47]. The majority used the most commonly used superconductor tape, the Bi-2212 as well as Bi-2223 as field coil [54]. Table 2−2 lists some of the synchronous motor prototypes that were developed.

Most rotating machines are radial type, with a cylindrical rotor. An axial rotating machine has a disk-shaped rotor (s) and stator(s) such as that in Fig. 2-1. One of the world's first axial-gap coreless (HTS) motors were developed at Tokyo University of Marine Science and Technology (TUMSAT) [55], [56]. They were cooled with a two-phase nitrogen thermosiphon cooling system. One of these motors had an output of 3.1 kW at 720 rpm. A multi-rotor axial bulk HTS motors was also developed at TUMSAT, with a speed of 200 rpm [57]. Both machines were magnetized by PFM using vortex copper coils. The IHI Corporation group has developed four types of axial-type HTS motors since 2004. Using a cooling system based on liquid nitrogen, they achieved the world's highest output at 365 kW in 2007 [58].

Table 2-2. Some of the superconducting machines using HTS and their year of development.

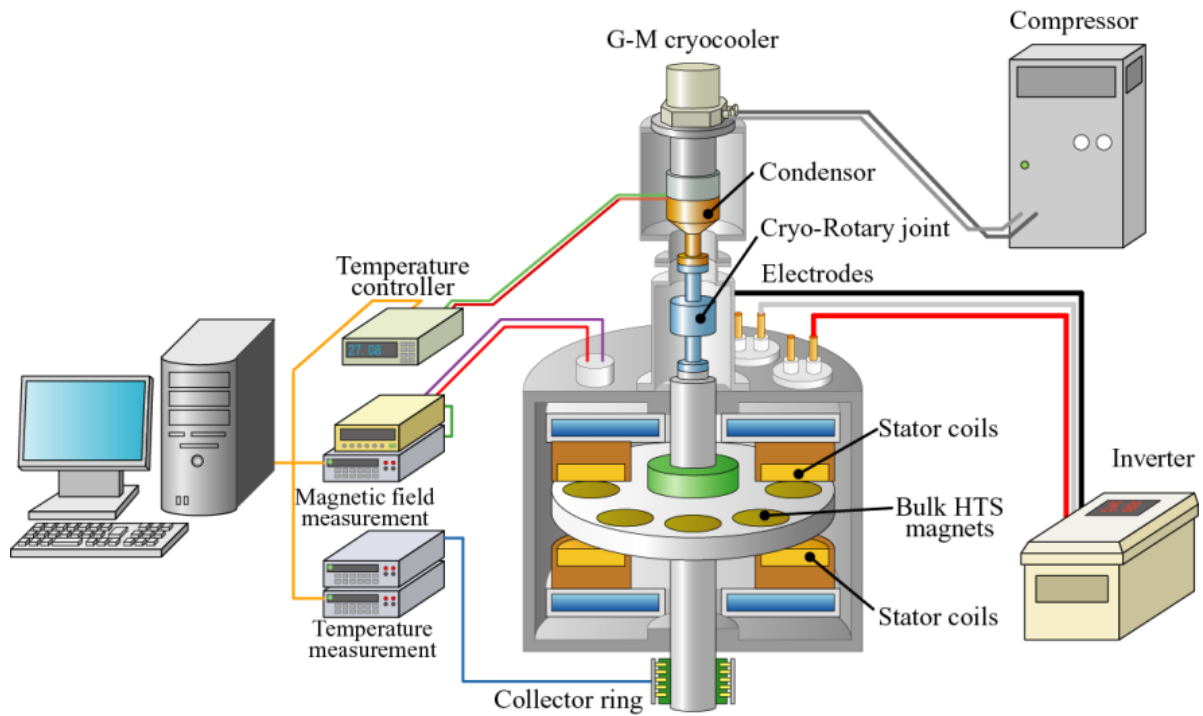| Year	Speed (rpm)	Power (kW)	Type	Trapped field (T)	HTS material	Coolant	Country
2005	720	3.1	Axial	0.5-0.8	Bulk GdBCO	Liquid N_2	Japan [59]
2007	120	36 500	Radial	--	BSCCO tape	Gas He	USA [53]
2007	200		Axial	1.04	Bulk GdBCO	Liquid N_2	Japan [57]
2010	190	1000	Radial	---	BSCCO tape	Gas He	Japan [60]
2012	190	3000	Radial	----	BSCCO tape	Gas He	Japan [60]

Fig. 2-1 An axial motor cooled by a thermosyphon cooling system Developed at TUMSAT.

2.2.2 Quench in HTS machines

In the event of a thermal or a current disturbance, the temperature of superconductor coils or bulks increase. During quenching in HTS coils, the resistivity and thus coil voltage drop, and temperature continue to rise, and the coil must be deenergized before they suffer damage. Extensive research has been conducted on HTS coil quenching. A study on quenching was conducted on motor BSCCO pancake coils by subjecting them to low quench current at 77 K [61]. One of the conclusions was that coil quenching was a complex phenomenon that depended on the properties of the coil, magnetic field distribution around it and its cooling environment. Moreover, coil voltage drop was found to have more than doubled while the coil power dissipation increased by an order of magnitude in a span of nearly 8 min 20 seconds from the onset of quenching. Lastly, it was reported that after the onset of quenching, it took up to 20 minutes for the coil voltage drop to raise to significant levels. This time is significantly shorter if the quench current is much higher than the critical current.

In the event of a cooling system failure, quenching would occur as temperature increase would result in the operating current to exceeding the critical current. Yet again a quench detection system must deenergize the machine to prevent damage. While HTS coils quench due to temperature and

31

current disturbances, bulks in electric machines normally quench due to temperature disturbances only.

2.3 Summary

From the above literature, it is evident that because of the nature of axial machines, it is challenging to trap high magnetic fields in axial machines. The use of PFM still does not yield high trapped flux. It was imperative to make bulk rotating machines of radial topology and devise an in-situ magnetization procedure for in-situ magnetization. Moreover, it has always been stressed that some technical challenges needed to be addressed to improve the development of bulk rotating machines [21]. Such are;

- There is a challenge of in-situ magnetization, since in-situ magnetisation does not yield hight trapped flux. The pursuit of high-density bulk HTS machines has concomitant challenges of in-situ bulk magnetization, mechanical reinforcement, cooling system reliability and bulk demagnetization. In-situ magnetization does not yield high trapped flux.

- Many researchers have feared the possibility of demagnetization as the trapped flux would be exposed to perturbating armature flux in a rotating machine. Bulks have been reported to demagnetise when exposed to perturbating fields.

- The need for the high mechanical strength of bulks when subjected to successive pulsed-field, and when subjected to high magnetising fields and rotational speeds. Bulks tend to physically degrade when subjected to successive pulsed-fields and could break when subjected to high magnetizing fields and rotational speeds since most are of ceramic nature. At the moment, mechanical properties of the bulk are the limiting factor towards the attainment of fields greater than 10 T.

- The need for cooling system reliability, as cryogenics is the enabler of superconductor application.

- HTS prototyping is still a very expensive undertaking. Low-temperature refrigerators and HTS material, especially wires are expensive [21]. However, bulks are cheap to fabricate.

Literature indicates that a number of partially superconducting synchronous machines including some for marine propulsion have been developed and tested around the world. Bulk HTS machines have virtually been overlooked elsewhere, except in Japan. But even after many demonstrator electrical machines based on HTS conductors were developed, such machines are still not

commercial. The lack of commercialization is due to the high-cost mass-produced HTS conductors and other auxiliary components that would allow for mass production of electrical machines. Therefore, more effort is needed to research and develop bulk HTS machines and this thesis contributes towards this cause.

Chapter III   Thermal analysis of a Thermosyphon Cooling System for HTS Machines

As one of the key enablers of HTS applications, cryogenics is one and thermal management is a crucial aspect in HTS machinery. Specifically, the cost and reliability of cooling systems are a major challenge in superconducting machine cooling technology. There is a need to develop reliable cryogenic power devices [49]. In parallel with work on HTS machinery, a cryogenic cooling system for an HTS machine, based on a thermosyphon was studied. The effectiveness of any thermosyphon as a heat transfer device is measured by its ability to cool the evaporator. Other thermal properties used to measure performance of a thermosyphon, such as heat flux and heat transfer area calculations are not included in this thesis but may be found in [62]. In this study, the temperature was measured only at certain points on the evaporator using low-temperature sensors. However, to get the temperature distribution of the whole evaporator, a thermal model was necessary.

This chapter discusses experimental and simulation works done on a stand-alone, non-rotating cryogenic thermosyphon system, with the aim of estimating temperature distribution of the evaporator of a two-phased thermosyphon cooling system. It is divided into two sections; experimental work and simulation. In the experimental scheme, heat load tests were conducted on the thermosyphon and its thermal parameters such as temperature and heat invasion were measured. In the simulation, a 3D model of the experimental thermosyphon equipment was developed for use in the ANSYS software. Temperature and heat invasion data from the experiments were incorporated as boundary conditions to estimate the temperature distribution around the evaporator.

3.1 Thermosyphon cooling system principle

A thermosyphon is essentially a gravity-assisted heat exchange device that circulates fluid in a closed-loop to transfer heat between two points that are at different temperatures. A thermosyphon comprises of three main parts, namely, the evaporator, adiabatic tube and the condenser shown in Fig 3-1. A natural thermosyphon has no moving parts, so fluid flow is gravity-assisted only. As such, the condenser is invariably placed above the evaporator in a gravity field [63]. The two most common thermosyphons, classified according to the number of phases of the working fluid, are

the one-phase and two-phase thermosyphons. One-phase thermosyphons employ a single-phase working fluid which may be liquid or gas. A two-phase thermosyphon operates with both liquid and gaseous phases of the working fluid. As such, it operates at saturated conditions, exploiting the latent heat of vaporization to achieve cooling.

In the evaporator section, heat is added to the working fluid which then absorbs latent heat vaporization as it turns into the gaseous phase. Pressure in the evaporator increases and pushes the vapor toward the condenser region through the adiabatic tube. Heat is rejected in the condenser as the vapor liquefies, leading to low pressure in the condenser section.
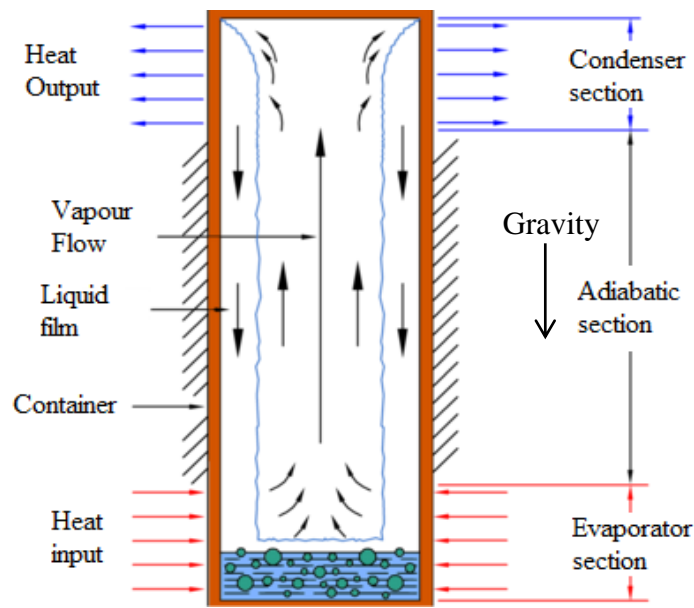
Figure 3-1. Parts of a two-phase closed thermosyphon.

The performance of a thermosyphon varies depending on the working fluid, filling ratio, and shape of thermosyphon. The filling ratio is defined as the ratio of the volume of liquid to the volume of the thermosyphon or evaporator. For any working fluid quantity, the filling ratio decreases as the evaporator heat load increases. The effectiveness of a thermosyphon as a heat transfer device is measured by the heat transfer capacity and effective thermal conductivity. The latter is calculated using (3-1) where A is the cross-sectional area of the thermosyphon, R is the thermal resistance and L the effective length of the thermosyphon. L is given by (3-2) where L_e, L_a and L_c are the lengths of the evaporator, adiabatic tube and condenser sections respectively [64].

$$K_{eff} = \frac{L}{A \cdot R} \tag{3-1}$$

35

$$L = \frac{Le}{2} + La + \frac{Lc}{2} \qquad (3\text{-}2)$$

There exists an optimum filling ratio at which both heat transfer and effective thermal conductivity are the highest. At low filling ratios, heat transfer is low since there is little fluid to transport heat. High filling ratios are associated with thick film boiling as well as large bubbles that tend to lower heat transfer. Two-phase thermosyphons cooling offer numerous benefits over conduction cooling. Since they utilize the latent heat of vaporization, thermosyphons have effective thermal conductivity several hundred times greater than that of copper and can, therefore, transfer large amounts of heat effectively with very small temperature gradients. Due to this, such thermosyphons operate nearly isothermally at saturation temperature. Consequently, an increase in the evaporator heat load causes a minimal increase in operating temperature [65]. Moreover, their simple structure makes them inexpensive and reliable. Fitting HTS machines with such a system are advantageous.
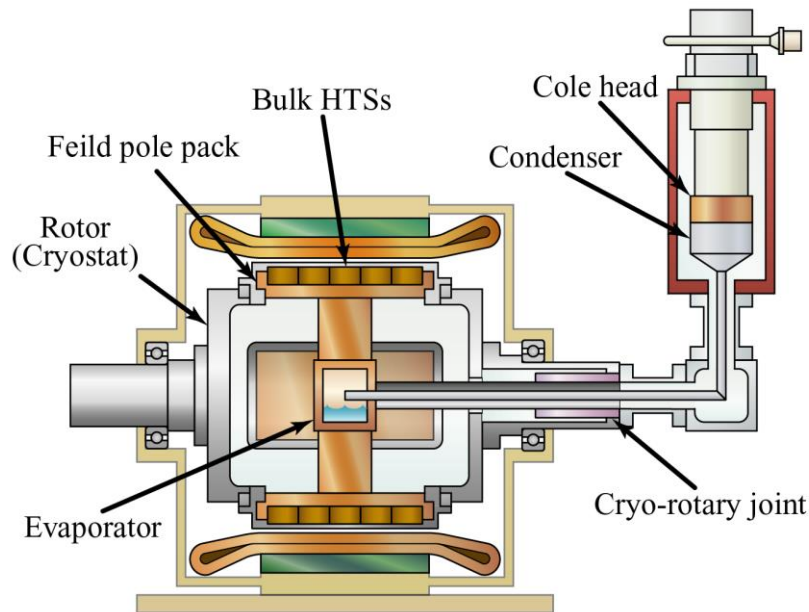

Figure 3-2. A sectional view of a thermosyphon-cooled HTS machines.

HTS motors and generators have HTS field coils or bulks that must be maintained at cryogenic temperatures. Thermosyphon-cooled HTS machine has superconductor field coils or bulks that are installed on the periphery of the evaporator which is located in a rotor cryostat as shown in Fig 3-2. An adiabatic tube is used to supply the evaporator with liquid cryogen from a stationary condenser mount on a cryocooler. Such cryogenic environments are created and maintained with the help of multi-layer insulation (MLI) blankets. Wrapping MLI blankets around the cold mass minimize heat radiation to the cold mass [66].

3.2 Thermosyphon experimental apparatus

The thermosyphon cooling system studied in this work was designed to resemble that in Fig. 3-2. It was designed to deliver nearly half the cooling requirement of a 20 MW HTS machine (400 W). Some of its design parameters are shown in table 3-1. The equipment has a cylindrical evaporator which is connected to two condensers with an adiabatic tube as shown in Fig. 3-3.

Table 3-1. Some parameters of the thermosyphon cooling system

Parameter	Value
Operating temperature (K)	30
Maximum cooling power (W)	183 at 29.6 K
Evaporator volume (ℓ)	21.5
Evaporator diameter x length (mm)	400 x 150
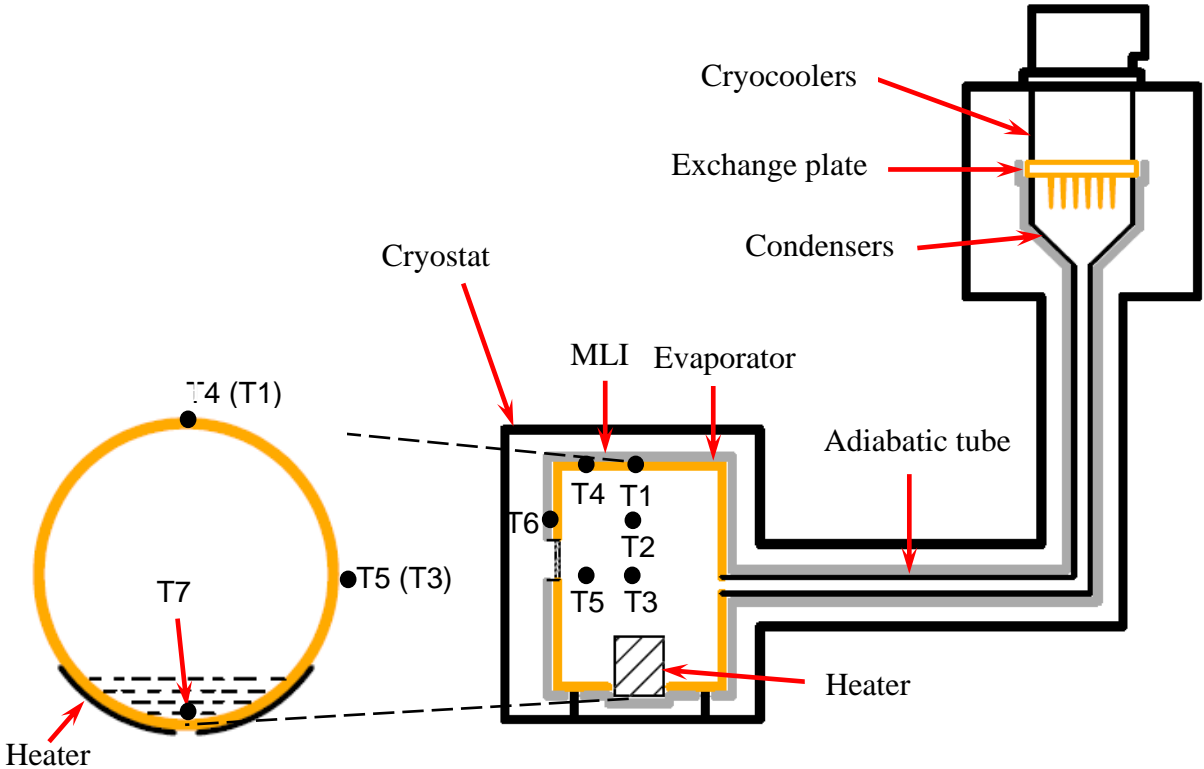
Figure 3-3. Thermosyphon experimental set-up and temperature sensors location.

Each condenser is mounted on a Cryomech G-M cryocooler with an oxygen-free copper (OFC) where a LAKESHORE silicon diode temperature sensor if fitted. Both cryocoolers were regulated at 29.7 K using a Lakeshore temperature controller. The adiabatic tube transfers fluid between the condensers and the evaporator and makes no direct contact with the cryostat. From the elbow, it slopes slightly downward to the evaporator to enhance fluid flow.

The evaporator and adiabatic tube are also fitted with a multitude of temperature sensors to measure the temperature at various points on the evaporator and adiabatic tube. Seven of the evaporator sensors are shown in Fig. 3-3. Sensors T1-T5 are on the outer diameter, T6 is on the leading flange, while T7 is inside the evaporator. T7 measures the temperature at the liquid neon-evaporator interface. Fig. 3-4 is a section of the evaporator side of the thermosyphon. The evaporator is suspended in the cryostat by fiberglass supports. On the underside, the evaporator has two polyimide thermofoil heaters wrapped on it, used to mimic heat generation in an HTS machine. Heaters are connected in series and are powered by a regulated dc power supply. Each heater has an effective heating area of 18548 mm^2.
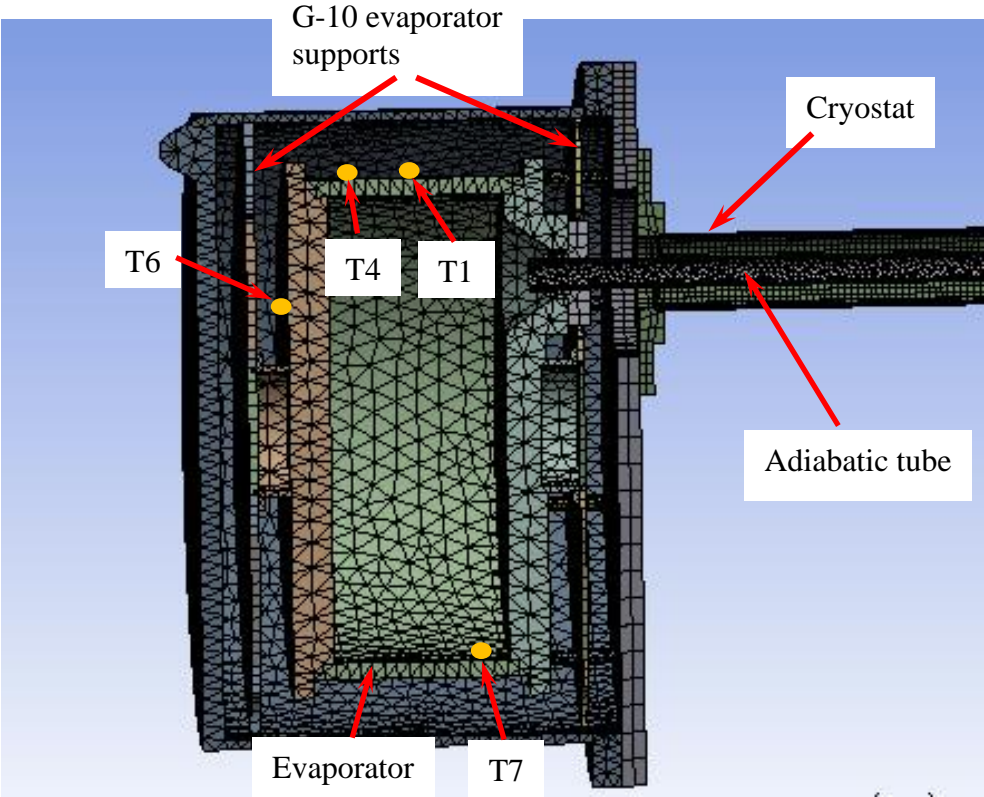

Figure 3-4. Meshed 3-D drawing of the thermosyphon. The model is 1:1.

There is also a provision to measure the internal pressure of the thermosyphon and a viewport through which liquid neon is viewed. The evaporator, adiabatic tube, condenser as well as the cold heads are wrapped in a Ruag Coolcat2 multi-layer insulation MLI (Fig. 3-4) blanket to minimize radiation heat transfer from the cryostat to the cold components inner. Each blanket consists of 10 layers of low emittance polyester films aluminized on both sides, separated from each other by polyester spacers. To reduce heat transfer by convection and gaseous conduction between the cold mass and the cryostat, a series connection of a scroll and turbo-molecular pumps were connected to evacuate the cryostat.
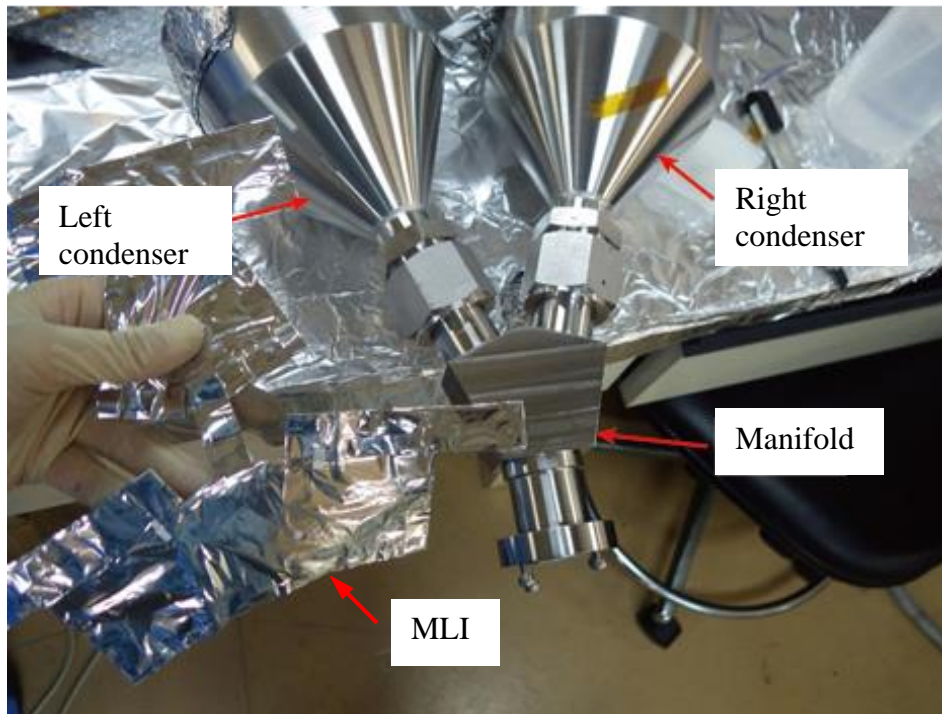
Figure 3-5. Ruag Coolcat 2 multi-layer insulation (MLI) before installation.

3.3 Heat load experiments

3.3.1 Initial cooling

The first step involves vacuuming of the thermosyphon to avoid air contamination. This is done using a scroll pump and a turbomolecular pump connected in series. After vacuuming, the pressure of the neon gas bottle was set to 0.106 MPa (gauge) before the valve between the thermosyphon and gas bottle was opened. During fill-up, the neon gas quantity and flow rate are measured and regulated with a HORIBA STEC SEC-E40 mass flow counter (Fig. 3-6). Next, the cryocoolers are switched on. Gaseous neon liquefies in the condensers which were regulated at $29.7\,\text{K}$. Liquefied neon flows down the adiabatic tube to the evaporator by gravity. The Horizontal section of the adiabatic tube slopes slightly downwards toward the evaporator to aid liquid flow.
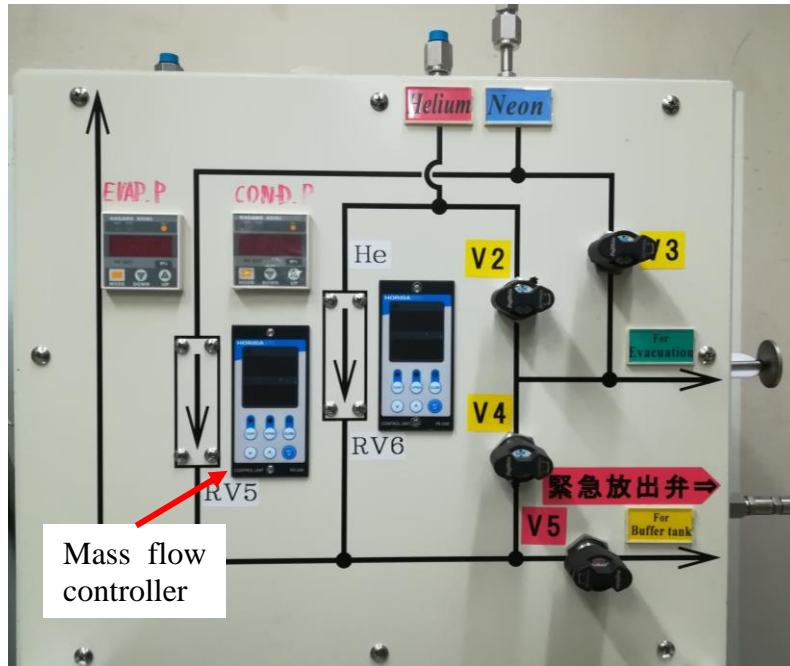
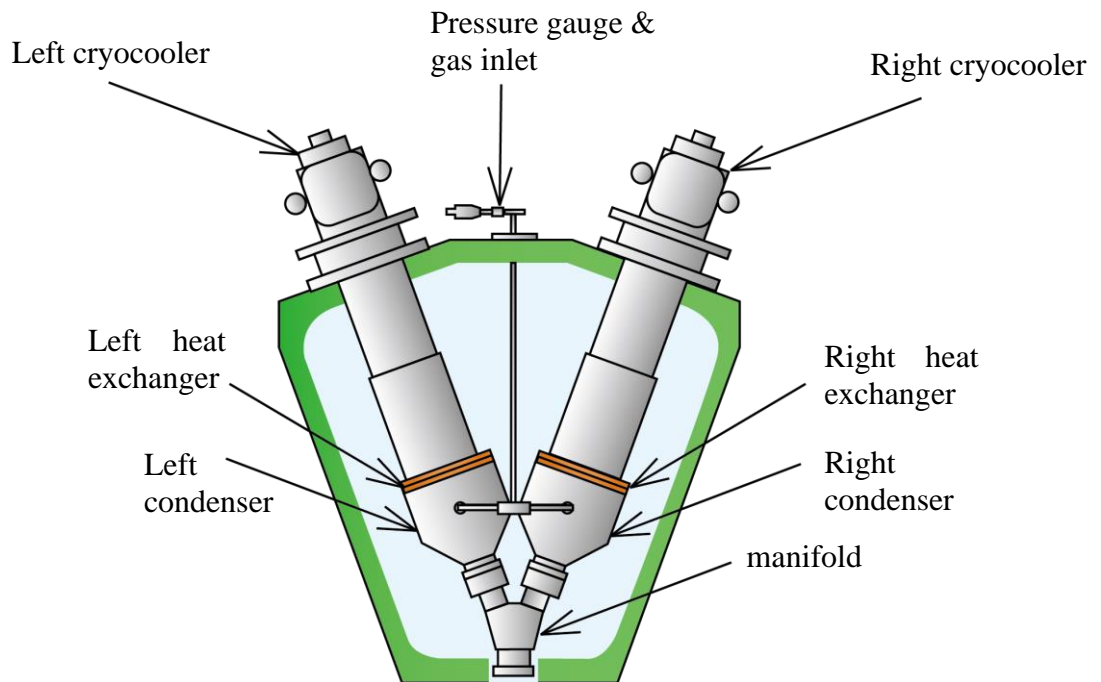Figure 3-6. Gas control panel with gas flow valves and mass flow controllers.

Figure 3-7. Thermosyphon gas inlet port.

3.3.2 Heat load experiments

The purpose of a thermosyphon is heat transfer. We filled up the thermosyphon with different neon quantities to determine its heat transfer characteristics so as to deliver cooling capacities. Four of the investigated neon quantities are indicated in table 3-1, where 100% cooling power is 183 W.

Table 3-1. Neon quantities fed into the thermosyphon.

Cooling power required (%)	Estimated Neon gas Quantity (NL)
50	434.7
75	440.4
100	451.4
125	469.5

Using the heaters on the evaporator, heat loads were applied to mimic heat load in an HTS machine. The heat load generated by both heaters is given by (3-3) where V is the voltage across the heater terminals and I the current through them. The thermal load from the heaters vaporizes the liquid and the gas flows to the condenser, thereby completing the cycle. For each neon quantity, the heat load was systematically increased in 5 W increments from 0 W until the nucleate boiling limit was reached. Each heat load step was maintained for 3 hours to ensure the steady-state operation was attained. The temperature of the evaporator, liquid -evaporator interface, adiabatic tube and condensers were acquired.

$$Evaporator\ heat\ load = V*I \tag{3-3}$$

The cryostat outer surface and the room temperature was measured and an averaged. The total amount of heat invasion into the cryostat was computed with a LabVIEW function from data of the cold heads cooling power using equation (3-4).

$$Heat\ invasion = Q_{CH} - Q_R - Q_E \tag{3-4}$$

where Q_{CH} is the total cooling power of the cold heads at 29.6 K, Q_R is the cold head temperature regulator heat load and Q_E is the evaporator heat load.

Invasive heat comes from the cryostat due to ambient air convection. The room temperature average was 296.3 K. Heat radiates to the MLI and eventually to the cold mass. Another heat invasion path was heat conduction from the cryostat to the cold mass through structural supports. The heat from instrumentation wires was presumed to be negligible.

3.4 Results

3.4.1 Filling ratio

The filling ratio is defined in equation (3-5). As the evaporator heat load was increased, the amount of liquified neon decreased. The filling ration, therefore, decreases with increasing heat load as shown in Fig. 3-8 and Fig. 3-9.

$$Filling\ ratio = \frac{Volume\ of\ liquid}{Volume\ of\ evaporator} \tag{3-5}$$
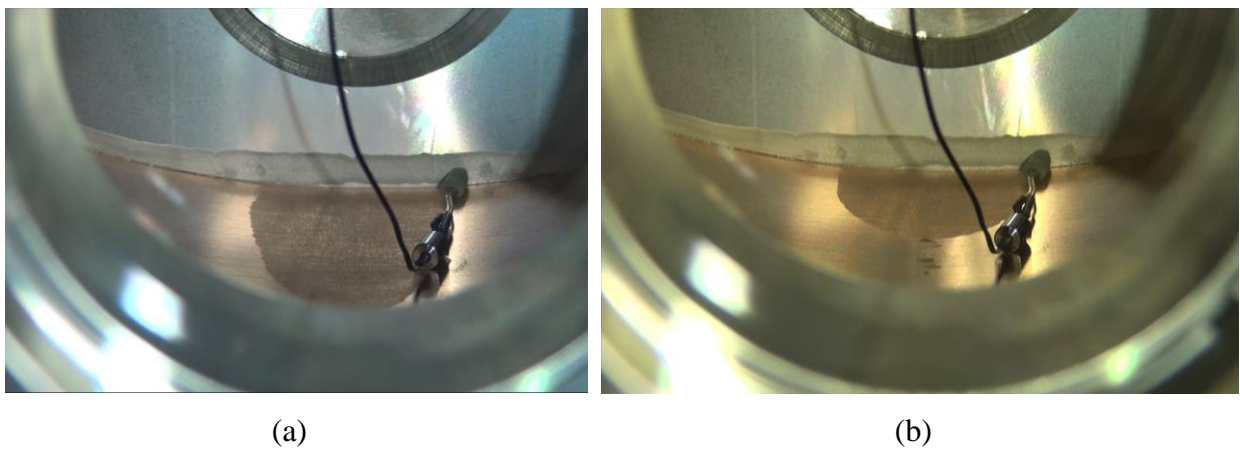

|(a)|(b)|

Figure. 3-8 Change in filling ratio at 434.71 NL as heat load increased. (a) 25 W, (b) 35 W.
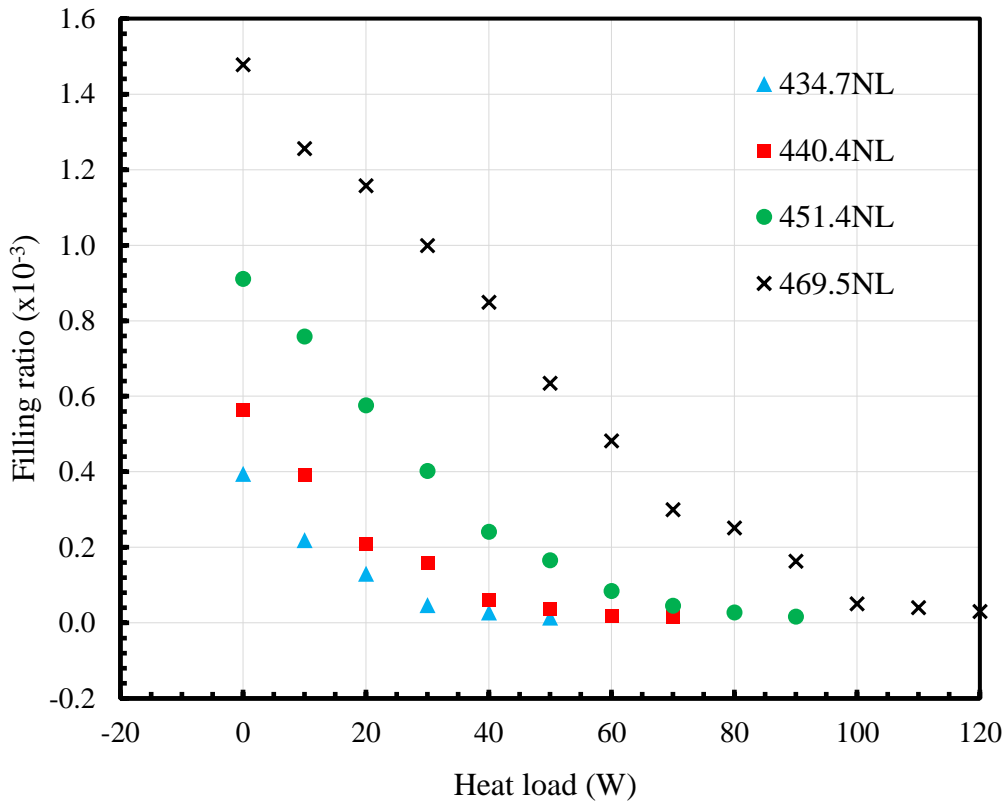
Figure 3-9. Variation of filling ratio with the applied heat load.

3.4.3 Heat invasion

Table 3.2. Heat invasion at different filling ratios at 0 W evaporator heat load

Neon Quantity (NL)	Heat Invasion (W)
434.71 NL	21.03
440.40 NL	21.93
451.4 NL	23.0
469.5 NL	22.51

3.5 Temperature estimation in ANSYS® workbench software.

Since we could mount only so many temperature sensors, we could not get the temperature at every point on the evaporator. To be able to compute the heat transfer capacity of the thermosyphon, the temperature distribution of the evaporator was necessary. The one solution was

to use thermal data from the experiment to estimate the temperature at all other points on the evaporator. Section 3.4.1 introduces heat transfer mechanisms which are key to understanding the rest of the section. Section 3.4.2 explains the thermal analysis of the thermosyphon and how it was implemented in ANSYS workbench.

3.5.1 Heat transfer modes

Heat in a thermosyphon is transferred between its different parts by one or a combination of the three mechanisms, namely, conduction, convection and radiation.

(a) Conduction

Conduction is the transfer of energy from the more energetic particles of a substance to the adjacent less energetic ones as a result of interactions between the particles. In gases and liquids, conduction is due to the collisions and diffusion of the molecules during their random motion. In solids, it is due to the combination of vibrations of the molecules in a lattice and energy transport by free electrons. The rate of heat conduction through a medium depends on the geometry of the medium, its thickness, and the material of the medium, as well as the temperature difference across the medium. The rate of heat conduction is governed by Fourier's law as [67];

$$\dot{Q}_{cond} = -k\,A\frac{\Delta T}{\Delta x}\ (\text{W}) \tag{3-6}$$

where: $k\left[\frac{\text{W}}{\text{m}}°\text{C}\right]$ is the thermal conductivity of the material and, ΔT is the temperature difference between the two points that are Δx apart, and A is the area normal to the direction of heat transfer.

(b) Convection

Convection heat transfer is the mode of energy transfer between a solid surface and the adjacent fluid that is in motion. Due to the continuity of temperature, the temperature of the fluid at the surface equals that surface temperature. Convection heat transfer is governed by Newton's law of cooling which is stated as [67]:

$$\dot{Q}_{conv} = hA_s\,(T_s - T_\infty)\ (\text{W}) \tag{3-7}$$

where h is the coefficient of heat transfer, T_s is the temperature the surface, and T_∞ is the temperature of the fluid sufficiently far from the surface.

(c) Radiation

Radiation is the energy emitted by matter in the form of electromagnetic waves as a result of energy transitions of molecules, atoms, and electrons of a substance. Unlike conduction and convection, the transfer of energy by radiation does not require the presence of an intervening medium. All bodies at a temperature above absolute zero emit thermal radiation. The radiation emitted by a surface at a temperature T_s is expressed as follows [67]:

$$\dot{Q}_{emit} = \epsilon \sigma A_s T_s^4 \qquad (3\text{-}8)$$

where $0 \leq \epsilon \leq 1$ is the emissivity of the surface, and A_s is the area of the surface.

The difference between the rates of radiation emitted by the surface and the radiation absorbed is the *net* radiation heat transfer. If the rate of radiation absorption is greater than the rate of radiation emission, the surface is said to be *gaining* energy by radiation. Otherwise, the surface is said to be *losing* energy by radiation. When a surface of emissivity ε and surface area A_s at an absolute temperature T_s is completely enclosed by a much larger surface at absolute temperature T_{surr} separated by a gas or vacuum (media which do not intervene with radiation), the net rate of radiation heat transfer between these two surfaces is given by (3-9) [67]:

$$\dot{Q} = \sigma A_s \varepsilon (T_s^4 - T_{surr}^4) \quad (W) \qquad (3\text{-}9)$$

3.5.2 Analysis of heat transfer in thermosyphon

The thermosyphon can be represented in schematic form as shown in Fig. 3-10. Heat invasion comes via convection from ambient air to the cryostat, and from the cryostat to the MLI by radiation. Heat transfer through MLI is a combination of radiation, solid conduction and in the presence of a gas, gaseous conduction. Consequently, the effectiveness of the MLI is affected by the physical composition of the blanket, average blanket temperature as well as mechanical compression. It is also affected by the presence of gas or humidity within the layers as MLI is more effective under high order vacuum [68]. We kept the vacuum at about $1\text{x}10^{-4}$ Pa, rendering residual gas conduction negligible. There was heat conduction from the cryostat to the cold mass through glass epoxy (G-10) structural supports. The heat from instrumentation wires was presumed to be negligible. Heat transfer mechanisms in the thermosyphon are shown in Fig. 3-10.
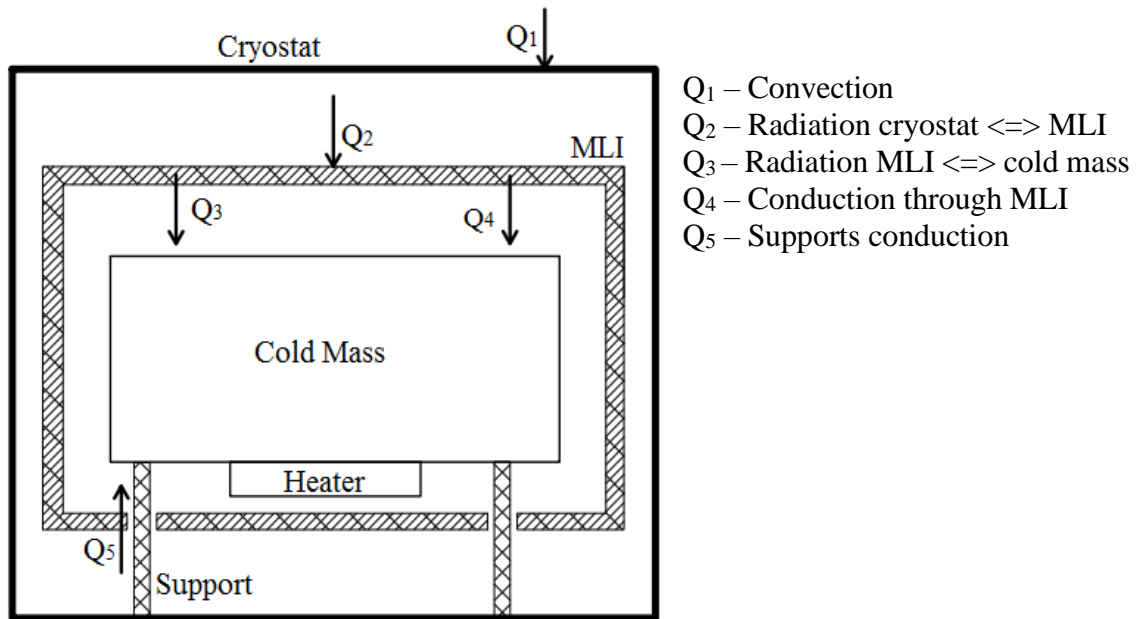
Figure 3-10. Heat transfer mechanisms in the thermosyphon.

3.5.3 Thermosyphon simulation in ANSYS®

A 3D model of the thermosyphon cooling system was used as a model in ANSYS® Workbench. The materials of the thermosyphon were defined in Ansys Workbench. Their Engineering properties were obtained from a NIST database. Components that are in contact were modelled with "bonded contact". For each filling ratio, the temperature of the adiabatic tube, the temperature of the evaporator area "wetted" by liquid neon, evaporator, evaporator heat flux, radiation and convection boundary conditions were defined. The program then computed the temperature of all objects of the thermosyphon.

(a) Determination of MLI effective emissivity

Due to the nature of heat transfer in MLI, the thermal conductivity of the insulation is not strictly defined in terms of variables such as temperature or physical properties of the component materials. It is therefore plausible to refer either to an apparent thermal conductivity, K_{eff}, or effective emissivity, ε_{eff}. Under high vacuum pressures, the theoretical value of effective emissivity can be predicted using equations but the actual value is usually larger than predicted due to conduction paths created between layers as a result of handling, and penetrations [68].

Thermal conductivity and effective emissivity values can be derived experimentally from data of a thermal system during steady-state heat transfer [68]. In this simulation, the MLI effect is modelled

with ε_{eff} which is defined as effective emissivity from the cryostat wall, through the MLI to the cold mass. As such, the MLI is modeled as a single surface coupled directly to the cold mass it surrounds and characterized by this effective emissivity. To determine the value of effective emissivity of the MLI in our thermosyphon, steady-state experimental data were used. This was done by using experimental data of 0 W heat load and then inputting this data into the thermal model of the thermosyphon. temperature and convection boundary conditions. The value of the effective emissivity was then tweaked until the total heat invasion (conduction and radiation) estimated by the model $Q_{\text{I,estimate}}$, was equal to the experimental value of 22.1 W at 0 W. The whole process is illustrated in Fig.3-11. The effective emissivity value was found to be 0.03. The rate of radiation heat transfer equation that models the MLI effect is, in this case, given by (3-10) [68]:

$$Q = \sigma A_{\text{S}} \varepsilon_{\text{eff}} (T_{\text{S}}^4 - T_{\text{Surr}}^4) \quad [W] \tag{3-10}$$

Where Q is the net heat transferred from cryostat through MLI to the cold mass [W], A_{S} is the surface area of the MLI [m^2], T_{S} is the temperature of the cold mass which the MLI surrounds [K], T_{Surr} is the temperature of the enclosing cryostat [K], and σ is the Stefan-Boltzmann Constant [5.67x10-8 W/m^2 K4].
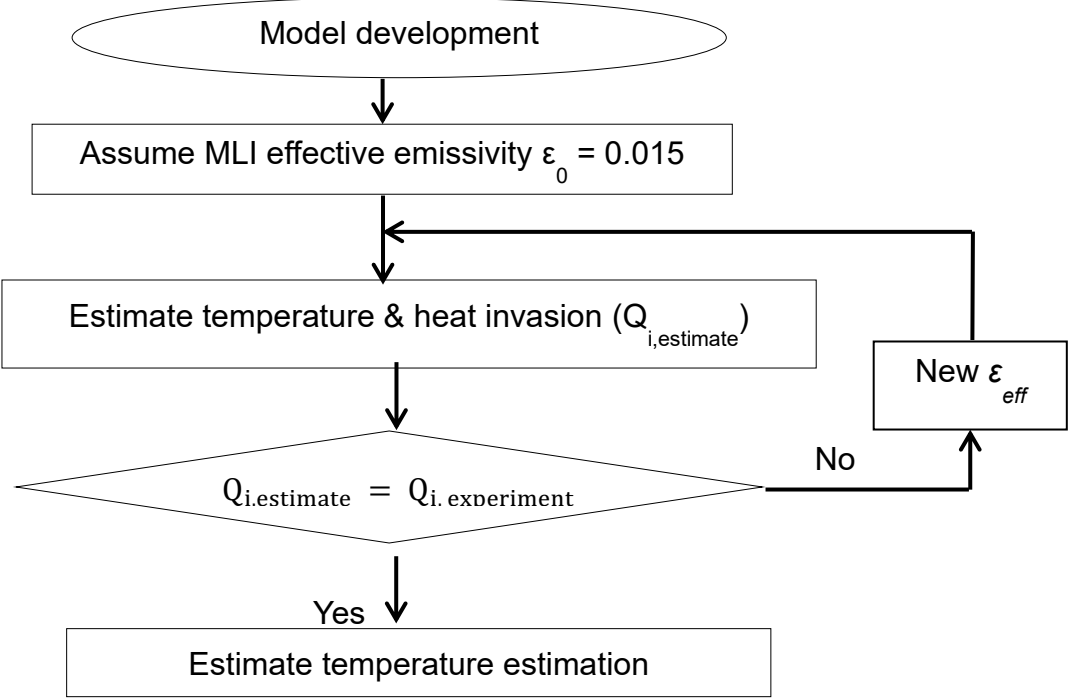

Figure 3-11. Process of determining the correct effective emissivity of the MLI.

(b) Boundary conditions

Convection. A convection heat transfer had been defined between the outer surface of the cryostat and ambient air. Since the bulk movement of the air was minimal, a convection heat transfer coefficient of $5\,W/m^2$ was chosen. The average temperature of ambient air had been computed as $296.3\,K$.

Radiation

Radiation objects were defined between the cryostat and the MLI. Radiation interaction is obtained by defining an enclosure between objects radiating to each other. The enclosure was further defined as PERFECT, as there was a negligible amount of air due to a high vacuum. Stainless steel has an emissivity of 0.15, and the effective emissivity (0.03) of the MLI was defined on surfaces directly coupled to the cold mass.

Temperature

The evaporator cryostat is equipped with two viewports through which the evaporator liquid neon contact area covered could be worked out for each heat load. The area covered by the neon was set to the temperature measured by a sensor at the liquid-evaporator interface. The area was determined by geometrical relations using images obtained from the experiment. The temperature was defined as such due to temperature continuity- the temperature of the liquid at the liquid-evaporator interface assumes that of the evaporator's inner surface. The inside of the adiabatic tube was set to the temperature registered by the liquid neon sensor.

Evaporator heater heat flux

Two model thermofoil heaters were used to apply heat loads to the evaporator. Heat load from of the heaters was applied as heat flux, specified on heater surface and directed onto the evaporator. The heater has an effective area of 18,548 mm^2 so I modelled it such that its area is equal to the effective area. The volume of the heater is 4618 mm^3. Heat load from the heater patch was defined as an internal heat generation, $\dot{G}$. Heat generation per unit volume $\dot{g}$ for each heater any heat load W is given by (3-11). since there are two heater patches.

$$\frac{\left(\dfrac{W}{2}\right)}{4618} \tag{3-11}$$

(c) Heat invasion in the model

Invasive heat in the model was calculated as the sum of heat transfer through the MLI and glass fiber supports of the evaporator. Heat transfer from glass fiber supports to the cold mass is conduction, while that from the MLI is a combination of radiation and conduction. Gaseous conduction was neglected due to the high vacuum level.

(d) Limitations

Limitations encountered during the simulation came in the form of physical model size and mathematical model restrictions placed on the academic version license used. Due to these, a rather coarse model had to be employed.

3.5.4 Results

Heat load tests were performed at different neon quantities. As the evaporator heat load was systematically increased, the filling ratio decreased until the dry-out limit.

(a) Temperature distribution

The temperature of the periphery of the evaporator was lower in the bottom and higher in the top section of the evaporator, consistent with the temperature profile from experimental data.

As the heat load is increased until nucleate boiling, the temperature increased. Table 3-3 gives the estimated maximum temperature (on evaporator periphery) for each neon quantity. The estimation suggests that the temperature is low enough for superconductor operation. Figure 3-12 shows the temperature distribution of a section of the evaporator as well as the supports and the cryostat.

Table 3-3. Estimated maximum temperature for various neon quantities

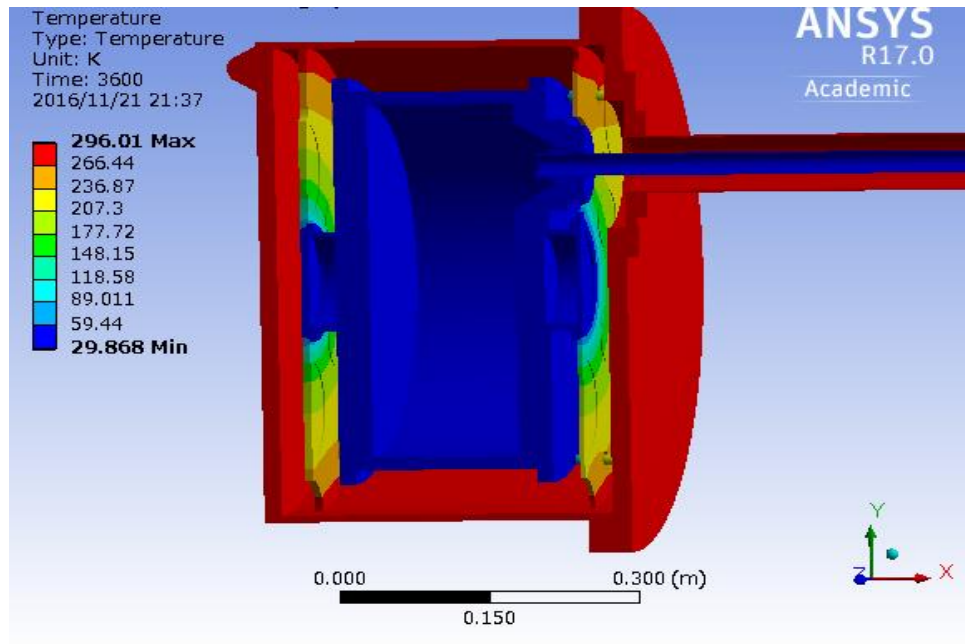| Neon Quantity (NL)	Maximum temperature (K)
431.7	32.6
440.4	33.1
451.4	33.6
469.5	34.1

Figure 3-12. Estimated temperature distribution of thermosyphon components. The evaporator in blue is at around 30 K. The cryostat is at room temperature (296 K).

(b) Temperature estimation error

The temperature estimation error is indicated here for some six sensors on the evaporator. Figures 3-14-3-17 show the error between experimental and estimated temperatures for different heat loads. The estimated temperature tended to underpredict temperatures at each sensor location compared to the experimental data.

$$\text{Estimation error} = T_{\text{experimental}} - T_{\text{estimated}} \tag{3-12}$$
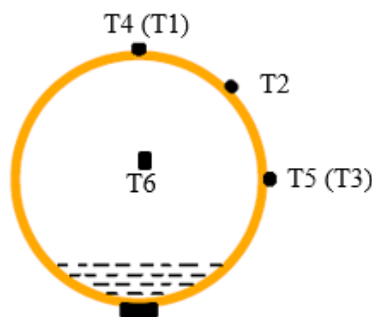
Figure 3-13. Locations of selected evaporator temperature sensors
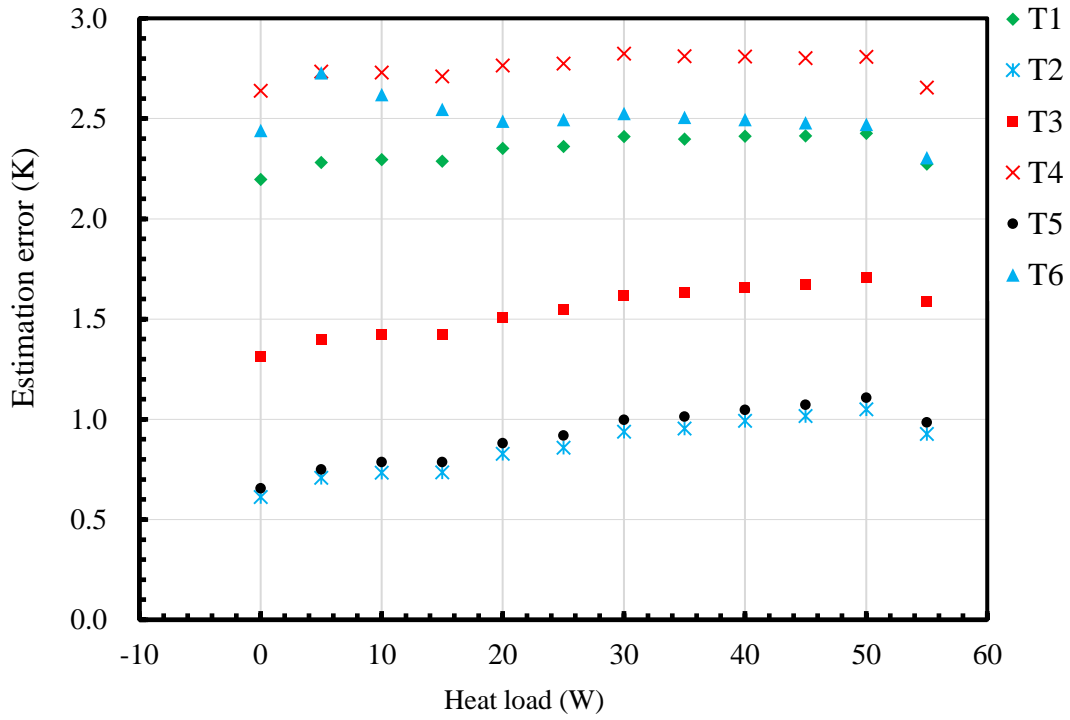
Figure 3-14. Temperature estimation errors at different heat loads. Neon quantity: 434.7 NL.
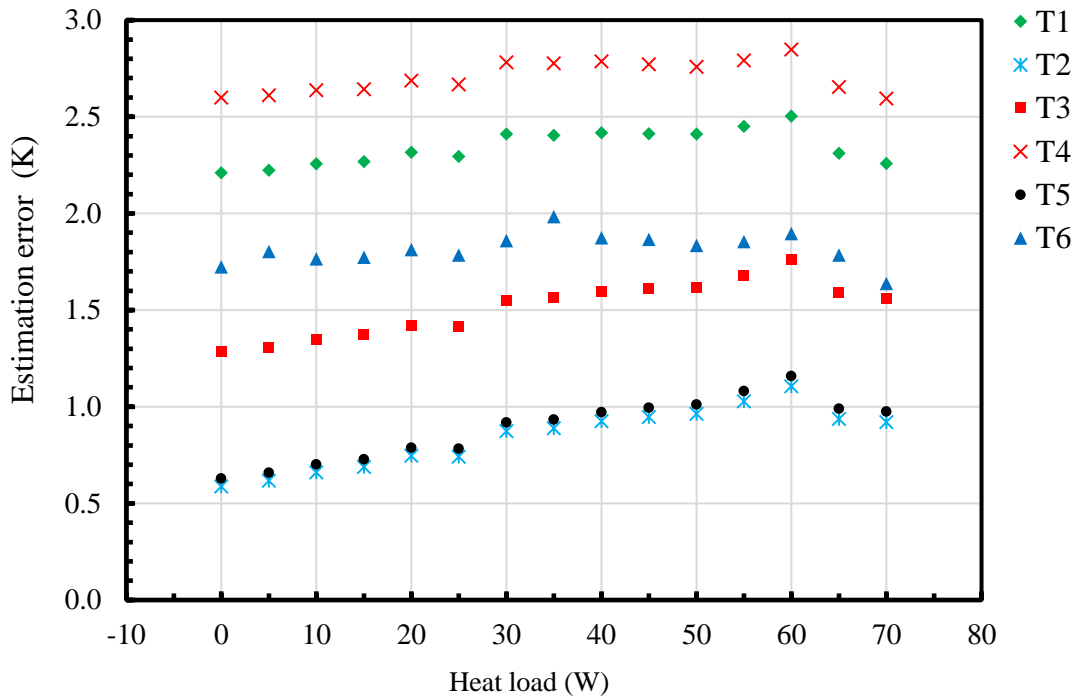

Figure 3-15. Temperature estimation errors at different heat loads. Neon quantity: 440. 4NL.
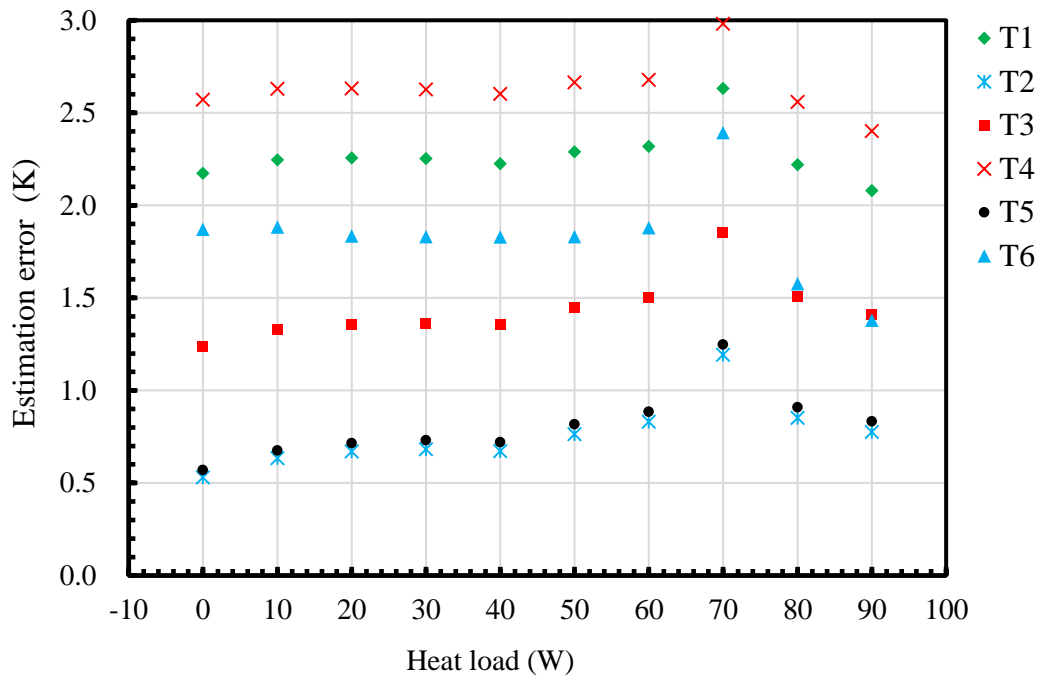
51

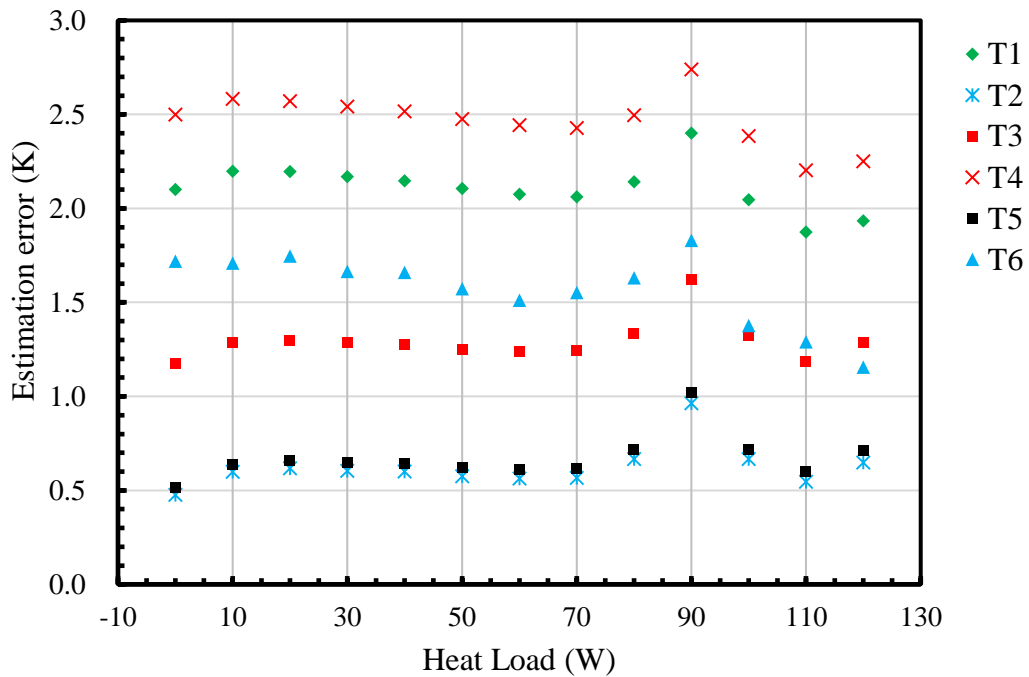Figure 3-16. Temperature estimation errors at different heat loads. Neon quantity 451.4 NL.

Figure 3-17. Temperature estimation errors at different heat loads. Neon quantity:469.5 NL.

The causes of the error could be threefold. The first cause could be the simulation 'bonded contact' that was defined between objects in contact. Bonded contacts lead to thermal coupling higher than the actual one. Secondly, the ambient air temperature changes continuously, thus convection may have played a role in the error. The third cause may be the neon liquid-evaporator contact area,

which may account for the concave downward shape of all graphs in figures 5-8. The implication of large errors at these inflection points is that they suggest a change in the boiling regime. Film boiling may have occurred at high heat loads, leading to a reduced neon liquid-evaporator contact area. During film boiling, pockets of vapor cover the evaporator surface so that the wet area is only a portion of the total contact area. In defining the evaporator temperature boundary condition, the total neon contact area was used.

(c) Heat invasion

Figure 3-18 shows the experimental and estimated heat invasion. It may be noted here that because the heat invasion value for 434.7NL was used in determining the effective emissivity, the experimental and estimated heat invasion values at 434.7NL are equal. The estimation is fairly good since the difference is at most 0.8W. The model further could be used to enumerate heat invasion being transferred to different heat transfer mechanisms. The estimated invasive heat through the MLI to the cold mass accounted for 48%, while conduction via all the supports amounted to 52% of the total heat invasion.
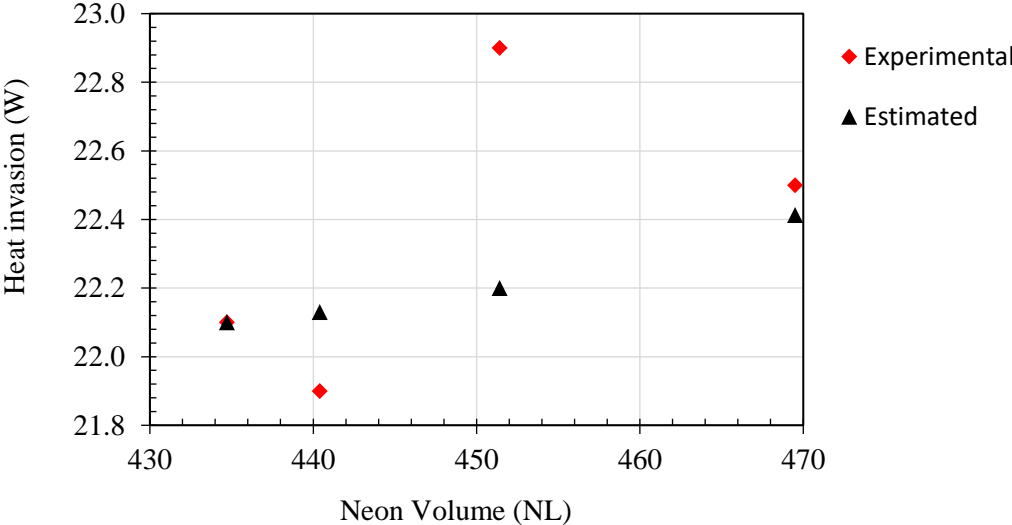

Figure 3-18. Experimental and estimated invasive heat at 0W of evaporator heater.

3.6. Discussion

This paper compared temperature distribution between experimental and simulated temperature data of a closed two-phase thermosyphon. Firstly, experimental data was obtained from neon thermosyphon at various filling ratios and heat loads. Secondly, thermal properties- temperature and heat invasion- of the thermosyphon were estimated by simulation. To include its thermal insulation effect, the MLI had been modelled using the effective emissivity approach and a reasonable estimation of the temperature distribution of the evaporator was obtained. It is noteworthy that the effective emissivity value falls well within the effective emissivity rage found in the literature (0.0005-0.5). The close proximity of simulation results to experimental data suggests that simulation results can be used to estimate temperature distribution or validate temperature sensor readings. The temperature error trend may be indicative of changes in boiling so that different boiling regimes could be inferred. The model also provided further insight into heat invasion into the thermosyphon.

Chapter IV Bulk HTS synchronous machine

In order to explore the potential of bulk HTS machines and validate the technologies required to develop them, while addressing challenges affecting HTS machine development, we developed a 30-kW, 190 rpm radial-gap synchronous motor using bulk HTS. The motor is prototype for electric ship propulsion. This chapter describes the design of the motor, its cryogenic cooling and magnetizing subsystems, and the test bed in which tests were conducted. It should be noted that the cryogenic cooling system employed to cool the bulks is similar to that studied in chapter III. Therefore, the utility of the neon thermosyphon cooling system discussed above is investigated in a practical machine operation. The setup of no-load and load tests and results thereof are presented in chapter V and chapter VI.

4.1 Bulk HTS synchronous machine description

This bulk HTS machine is a low-speed, radial-gap synchronous machine prototype envisaged for use as a ship propulsion motor. It has a rated power and speed of 30-kW and 190 rpm, respectively, at the operating temperature of 30 K. Other technical specifications of the machine are given in table 4-1. The stator, shown in Fig. 4-1, is a conventional air-cooled stator with ferromagnetic teeth and a back yoke. Core laminations are made from silicon steel grade M600-50A with maximum core loss of 2.60 W/kg at 1.0 T and 6.00 W/kg at 1.5 T at 50 Hz. Stator laminations inner and outer diameters are 300 mm and 385 mm, respectively. The iron core length is 265 mm long and has a mass of 358 kg. The armature winding has 3 phases of stranded copper conductors. Each is equipped with a PT100 RTD temperature sensor. Propulsion motors must be reliable, and resistant to mechanical shocks. Thus, it is essential that a propulsion motor has a large physical air gap of 6.5 mm.

Table 4-1 Technical data of the HTS synchronous machine

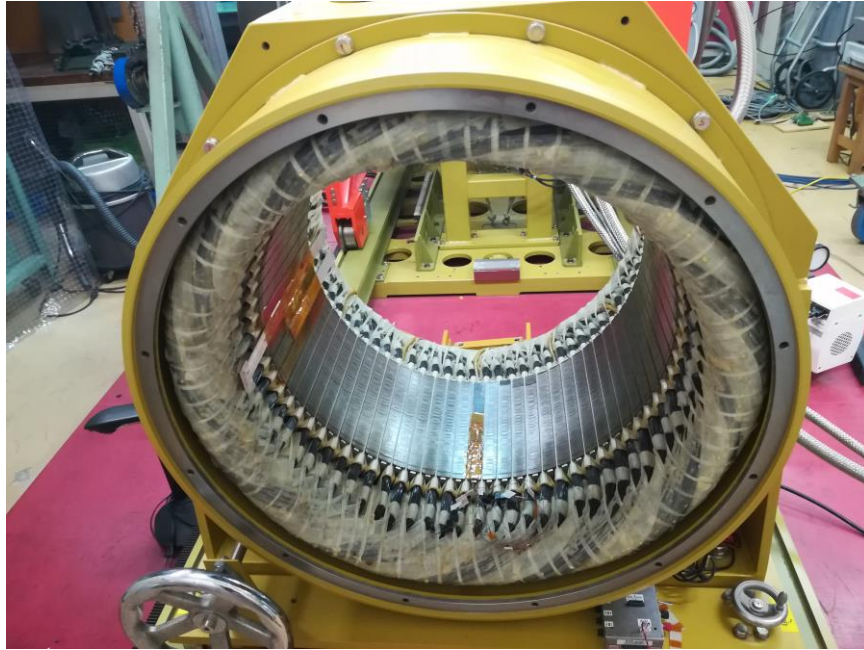|	
Rated Power (KW)	30
Number of poles	4
Rated Speed (RPM)	190
Physical air-gap	6.5 mm
Rated stator voltage (V)	220
Stator winding connection	Y (star)
Winding	Double-layer

Figure 4-1. the conventional stator of the 30-kVA bulk HTS machine.

4.1.1 Rotor

The rotor is 540 mm long while its outer diameter is 590 mm. It has 4 salient poles, and each is 334 mm long and 192 mm wide. Each pole has an oxygen-free copper (OFC) holder with a rectangular array of 15 melt-growth $GdBa_2Cu_3O_{7-\delta}$ bulk HTS ($QMG^{®}$) as shown in Fig. 4-2. Copper holders are thermally anchored to the evaporator of the thermosyphon cooling system via radial OFC bars shown in Fig. 4-3. Each plate is equipped with a 160 W electrical heater used for pole temperature control during magnetization. Specifications of the rotor are summarized in Table 4-2.
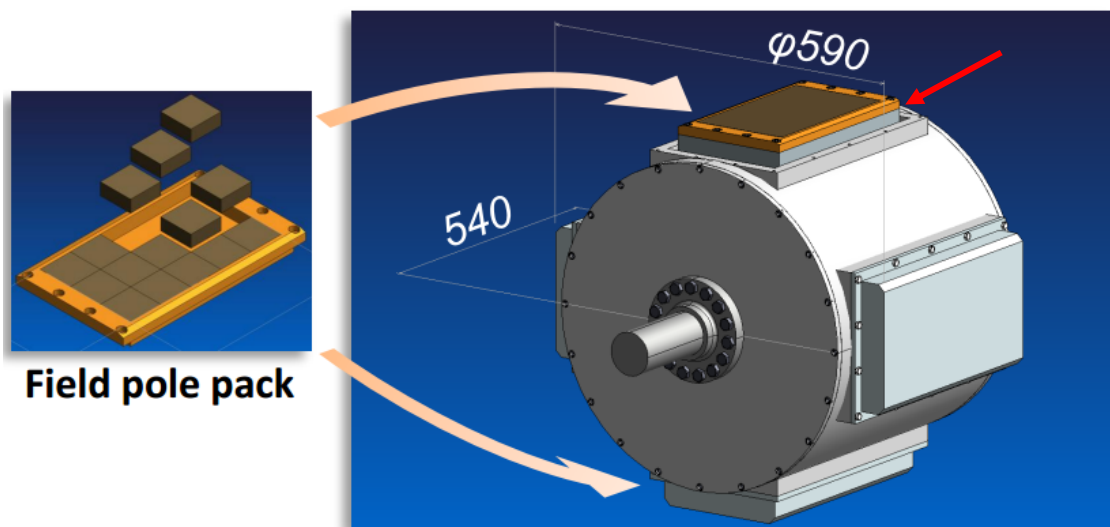

Figure. 4-2. Concept design of bulk HTS pole and outer dimensions of the rotor.
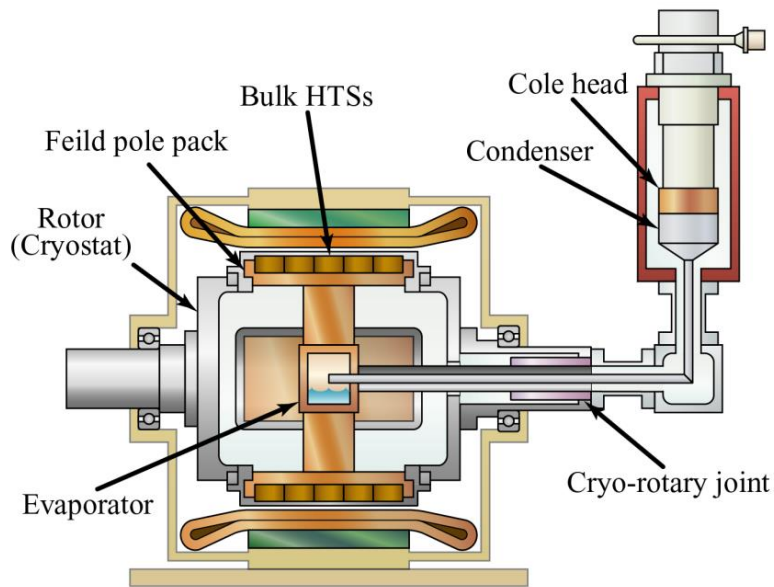
Figure 4-3. A side view of the HTS rotating machine showing the rotor and its thermosyphon cooling system.

Table 4-2. Specifications of the rotor

Field Poles	GdBCO (QMG$^{\circledR}$)
Bulks per pole	15
Bulk dimension (mm)	15 x 15 x 20
Thermosyphon working fluid	Neon
Operating temperature range (K)	30 - 40

4.1.2 Cooling system

HTS poles are cooled by a 150 W capacity neon thermosyphon, similar to the one discussed in chapter III, which maintains an operating temperature of 30 K. At the heart of the cooling system are two G-M cryocoolers (Cryomech AL330). Attached underneath each cryocooler, is a condenser with copper fins. Condensers are connected to a manifold of the vertical section of the adiabatic tube as shown in Fig.4-4. The thermosyphon was filled with 105 NL of neon using a HORIBA STEC neon mass flow counter in Fig.4-5. Gaseous neon is liquified in the condenser, then flows down to the evaporator by gravity. The liquid in the evaporator absorbs latent heat from the evaporator as it evaporates and flows back to the condenser, thereby cooling the evaporator and completing the thermosyphon cycle. The temperature of the poles and thermosyphon internal

pressure were monitored throughout the test. To enable relative motion between stationary cryocoolers and the rotating rotor, a rotary joint [69] is used.
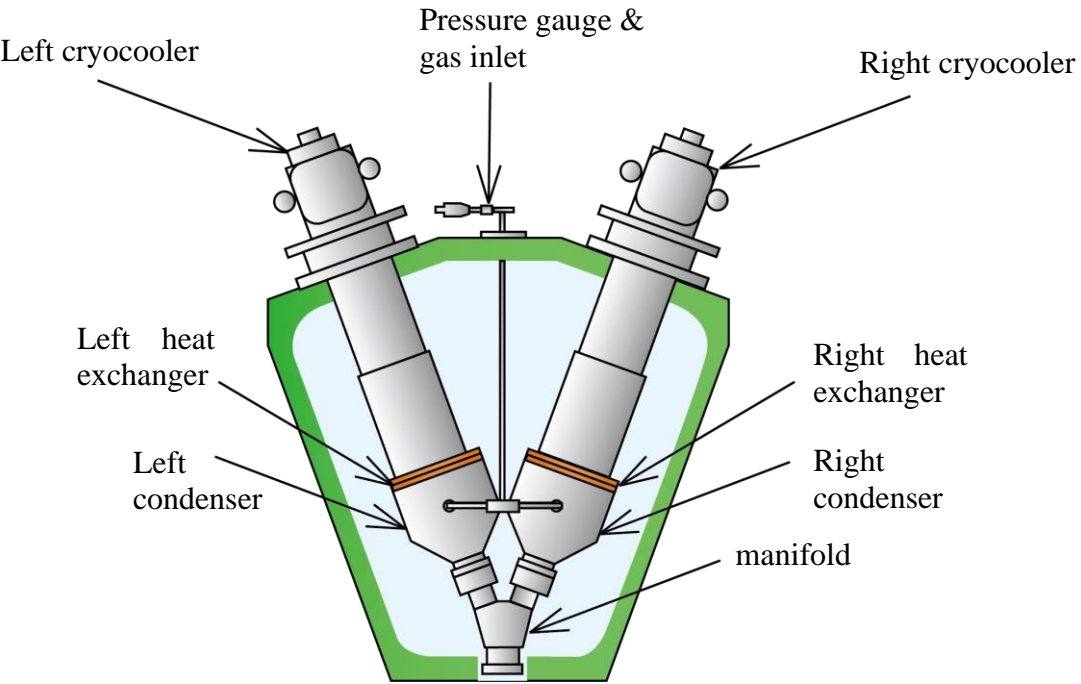

Figure 4-4. The G-M cryocoolers and condensers of the cooling system.
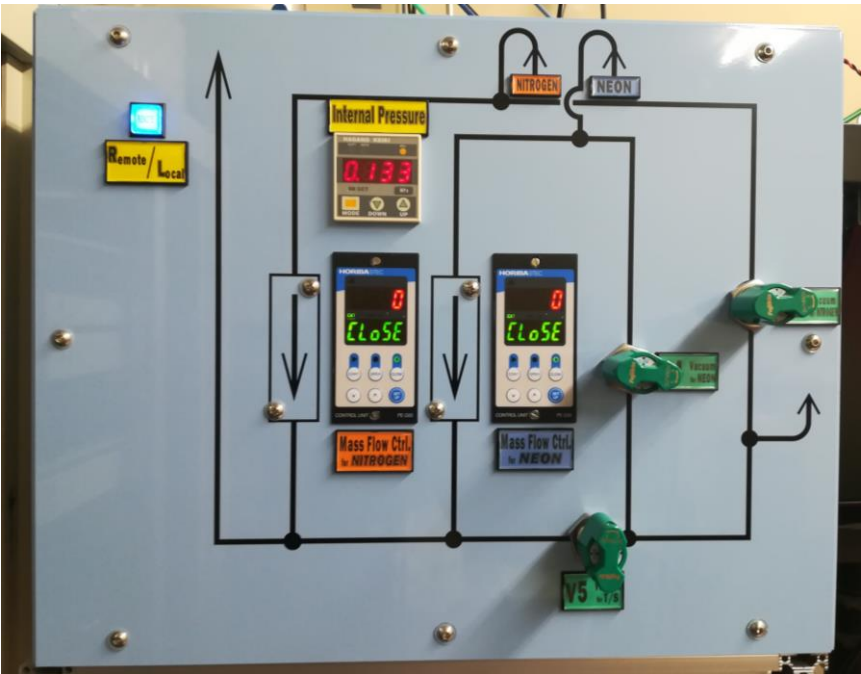

Figure 4-5. Gas control panel with HORIBA STEC mass flow counters.

4.1.3 Magnetising system

Field pole bulks are magnetized via field cooling (FC) using an HTS magnetizing coil unit consisting of 6 racetrack coils of 2G HTS wire. It is operated at a temperature of 20 K. The unit provides a uniform magnetic flux cavity that is 581.4 mm long, 230.0 mm wide and 48.24 mm deep wherein the pole to be magnetized (hereinafter called target pole) is centrally positioned as shown in Fig. 4-6. Limit switches in the vertical and horizontal directions are used to position the poles relative to the coil. Only one pole can be magnetized at a time, therefore the four poles have to be magnetized sequentially. The coil can develop a magnetic flux of up to 3.5 T. The magnetizing procedure is schematically illustrated in Fig. 4-7, where is T_c the critical temperature (93 K for GdBCO). The pole to be magnetized is heated to a temperature of 100 K, above T_c using an electric heater of the target pole. Heater power is kept held constant to maintain the bulks in the normal state. The magnetizing field is then applied, after which the heater is turned off to decrease the target pole temperature. The external field is turned off when pole the temperature of the pole is 70 K.
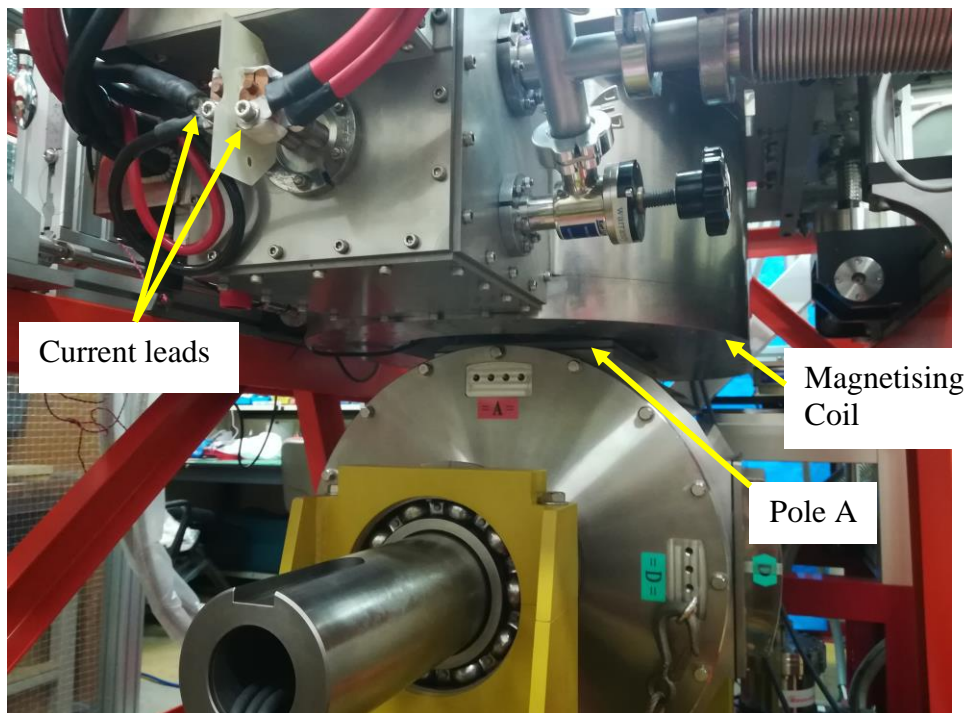

Figure 4-6. Coil-pole positioning during the magnetization for bulk pole A. Pole A is inside the uniform-flux cavity of the coils Positioning is achieved using a set of limit switches.
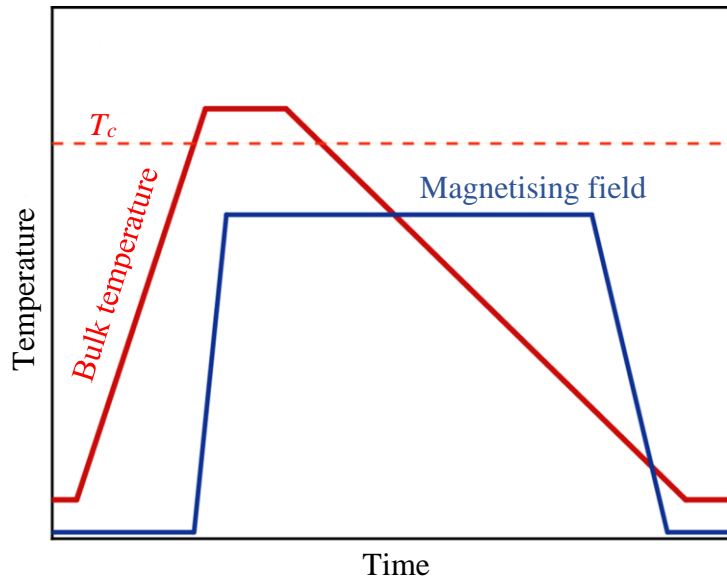
Figure 4-7. Schematic of a field-cooling (FC) magnetization procedure of a bulk HTS pole.

By alternating the polarity of the magnetizing coil current, the rotor is magnetized with alternating polarity as shown in figure 4-8. The trapped magnetic flux density was measured in the airgap using Hall sensors (BHT-921 Bell) which have an error of 1 % at ± 3 T. A total of 5 hall sensors were fixed on the inner diameter of stator teeth in order to measure the trapped field at a distance of 17 mm from the surface of bulk.
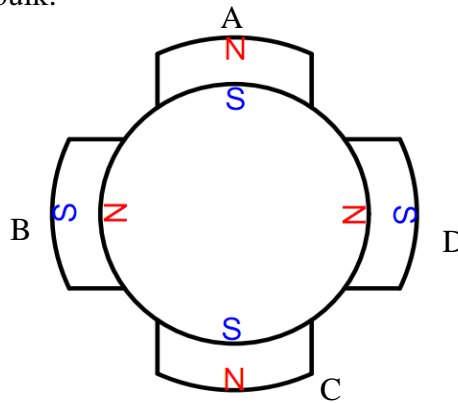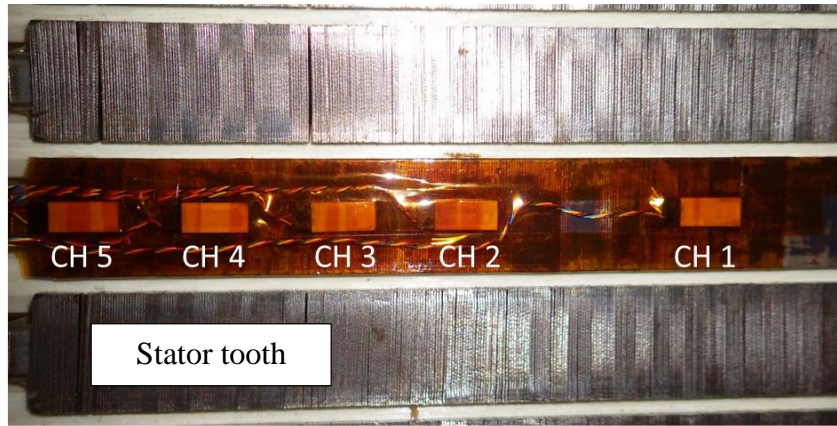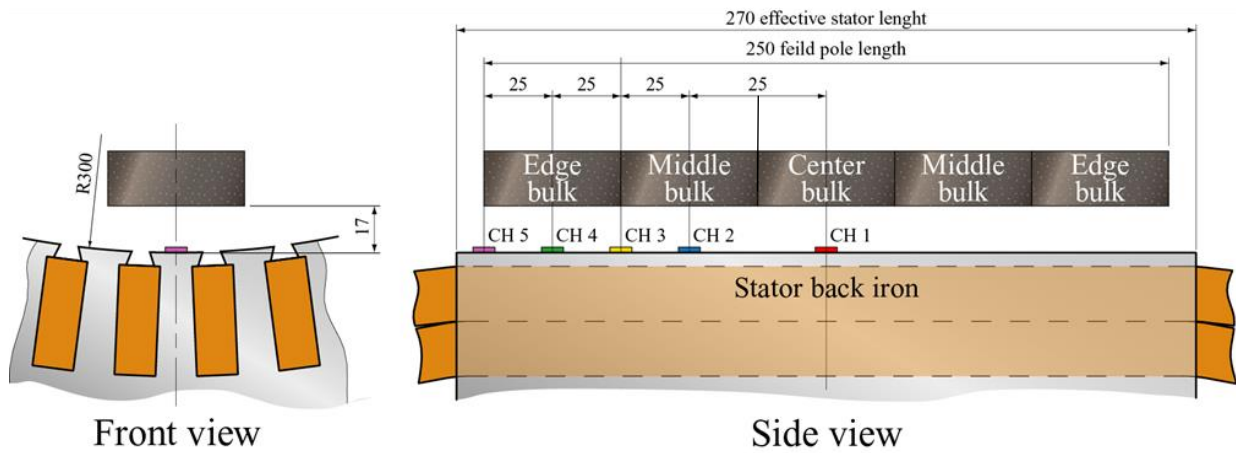

Figure 4-8. Identifier letters and polarity of rotor poles after magnetization is complete.

The positioning of the hall sensors, relative to pole bulks is shown in Fig. 4-9. A rotary encoder was employed to measure the angular position of the rotor with ± 0.25° angular resolution.

(a)

(b)

Figure 4-9. (a), the five Hall sensors mounted on the inner diameter of stator teeth. (b), the position of the Hall sensors, relative to pole bulks. Channel 1 (CH1) coincides with the center if the middlemost bulk, while CH5, is on the edge of the outermost bulk.

4.1.4 HTS motor test bed arrangement

After magnetization, the stator is installed back over the rotor. A 14.9 kW induction pony motor, reduction gearbox, and a speed-torque transducer are connected onto the output end of the rotor shaft and mechanically aligned. The pony motor is used to rotate the rotor of the HTS motor during tests. The gearbox provides a 9.26:1 speed reduction ratio was used so that the HTS motor can be run at low speeds. At the motor's rated speed of 1759 rpm, the gearbox outputs 190 rpm and a torque of approximately 750 Nm. The arrangement of the test bed is shown in Fig. 4-10. The torque meter measures the speed and torque on the driving end of the HTS motor shaft.
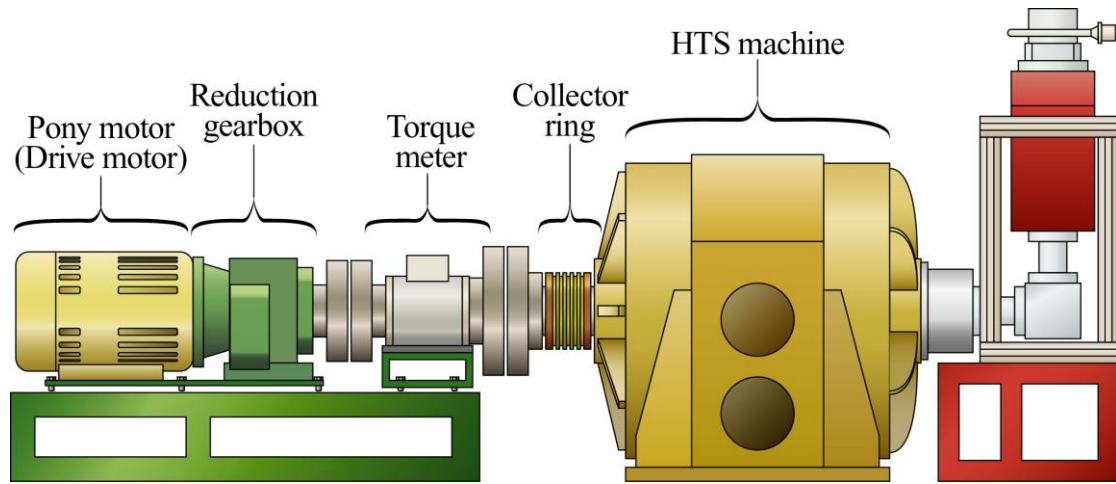
Figure 4-10. Testbed after magnetization and installation of the stator. The speed-torque (S. Himmelstein MCRT 48004(5-3)-N-F-Z) transducer measures mechanical parameters.

4.2 Conclusion

This section was dedicated to the description of the bulk HTS machine and its testbed. The most crucial subsystems, the cooling, and magnetizing systems and their operation have been highlighted. The cryogenic cooling system employed is similar to that studied in chapter III, and therefore, the performance of the neon thermosyphon cooling system is gauged during machine operation.

Chapter V No-load tests

This chapter is dedicated to the set-up and execution of no-load tests conducted on the bulk HTS machine described in chapter IV. The results thereof are discussed.

5.1 Magnetisation

With the rotor cooled to the operating temperature of 30 K (see Fig.1), poles were magnetized sequentially. The FC magnetization procedure for target pole A at 1 T is shown graphically in Fig. 5-2. The target pole is warmed up to a temperature of 95 K, above the critical temperature of GdBCO (93 K). It takes about 36 minutes. The magnetizing coil is excited and reaches 1 T after 5 minutes. The pole heater is turned off soon thereafter causing the temperature of the pole to drop. Upon reaching 70 K after 73 minutes, the magnetic field is ramped down. It takes nearly 91 minutes from pole heating to the point where the magnetizing flux reaches zero. Magnetizing current ramp up and ramp down rate can be reduced by increasing the allowable voltage drop across the coil. A maximum of 2.0 V was used in this experiment.
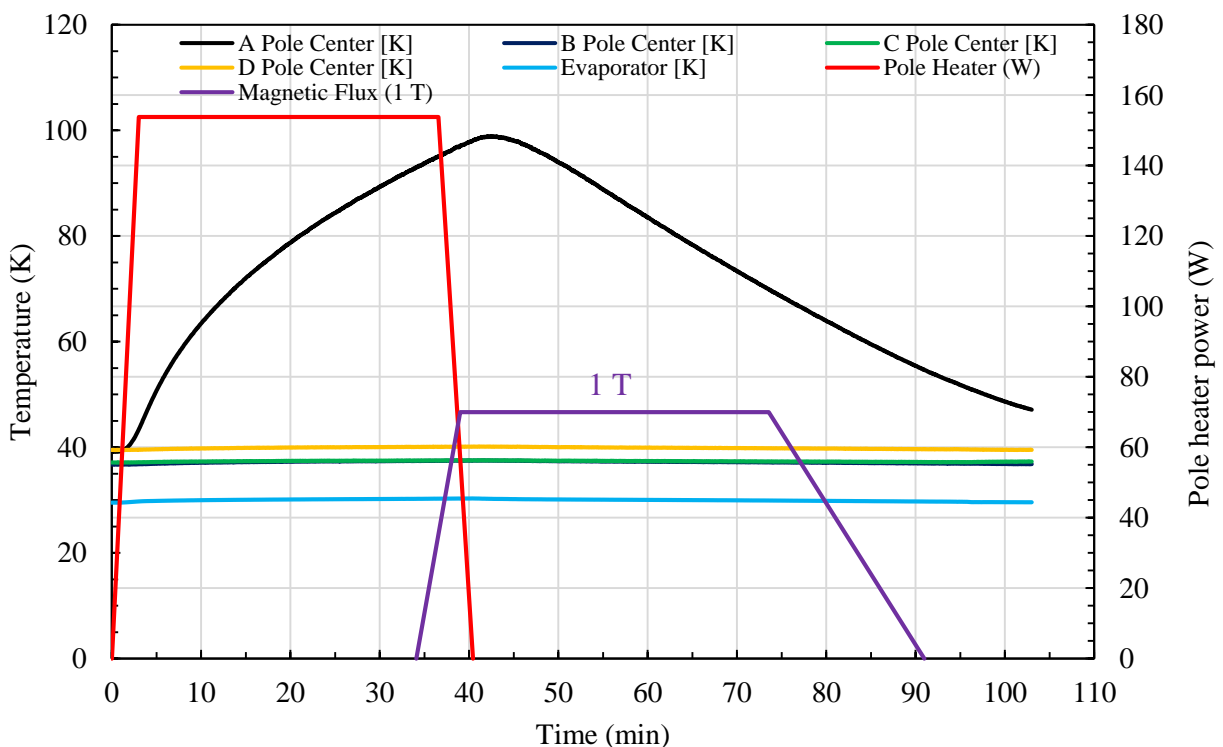

Figure 5-1. Magnetization procedure for bulk pole. Here, the target pole is A.

5.2 No-load setup

A no-load curve is a typical characterization curve of a rotating machine obtained from test running a machine without a load connected. In this test, the HTS synchronous machine was tested in the generator mode by rotating it with a pony motor. The speed of the pony motor was controlled using a commercial ABB ACS800 variable speed drive with an output power rating up to 110 kW. No-load voltage (terminal voltage) induced in the armature was measured at speeds between 10 rpm to 190 rpm using the set-up in Fig. 5-2. The speed and torque of the motor were measure using a torque transducer. A power analyzer was used to record and compute the electrical parameters of both the variable speed drive and the HTS machine. Tests were conducted at different rotor magnetization levels of 1 T, 2 T and 3 T. For each magnetization level, the rotor was demagnetized and magnetized to the required level.

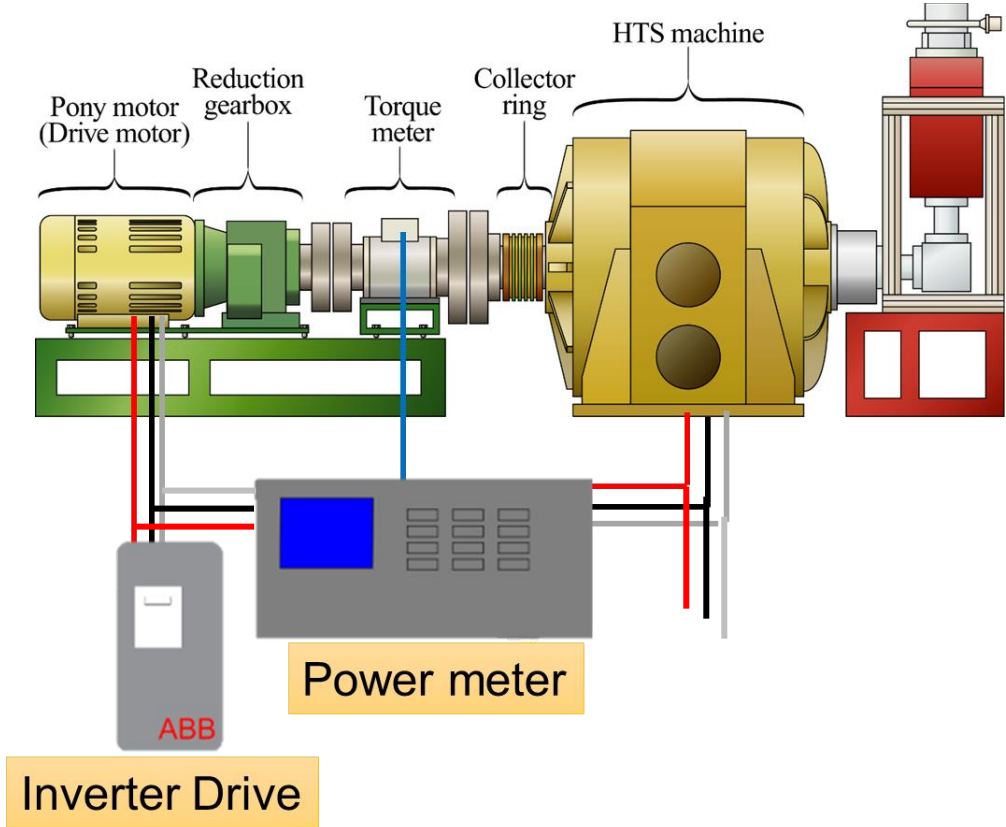Figure 5-2. No-load set up of the HTS machine in the testbed. The terminals of the HTS machine were left open.

5.2.1 No-load voltage

Alternators generate an AC electromotive force (emf) whose frequency depends on the speed of the rotor. Emf induced in a coil of N turns is sinusoidal and depends on the rotor speed ω, and the total magnetic flux in the air-gap as per equation (5-1) [70].

$$V_{ind} = N\phi\,\omega\cos\omega t \tag{5-1}$$

From a rotating machine point of view, the emf induced in armature coils depends on the armature winding flux linkage λ, and the rotational speed ω of the rotor. From (5-1) the peak induced emf can be obtained (5-2).

$$V_{max} = \lambda\omega \tag{5-2}$$

Where $\lambda = N\phi$. The RMS value of this emf is given by (5-3)

$$V_{rms} = \frac{\omega\lambda}{\sqrt{2}} \tag{5-3}$$

The emf was obtained from the no-load set up in Fig.5-2 for various levels of rotor magnetization and at different rotor speeds.

5.2.2 Open-circuit core loss

The no-load set up also allowed for determination core loss at different magnetic flux levels and different speeds. In the core loss measurement scheme of Fig.5.2, the pony motor rotates the generator and the terminals of the generator were left open-circuited. Torque and speed data from the torque transducer were used to determine machine mechanical input power. Friction and windage losses were determined by measuring the power consumption of the machine while running the machine with an unmagnetized rotor. Core loss at any given speed was computed using (5-4).

$$Core\ loss = total\ power\ input - friction\ and\ windage \tag{5-4}$$

5.3 Results

5.3.1 Trapped field profile After magnetization

Fig. 5-3 shows the profile of the trapped flux density distribution at the center of the pole along the a-axis. The 5 peaks are on the c-axis of the five center bulks, with the maximum trapped flux of occurring near the center of the pole. The trapped flux value decreases towards the pole edges along with both the a- and b-axes. Table 5-1 lists the values of the magnetic field, B_{centre}, at the surface of the rotor with 10 mm above the surface of the field-pole bulks after magnetization under 1, 2, and 3 T. It also lists the maximum magnetic field (measured at CH1) in the airgap after stator installation. Air-gap flux density was measured at the centre of the pole as well. The air-gap flux

is high due to the low reluctance of the teeth. Although the trapped field on the bulk surface may be close to the magnetizing field, its value decreases dramatically along the c-axis. However, the surface integral of the flux over the pole, and consequently the magnetic loading of the machine are rather large.
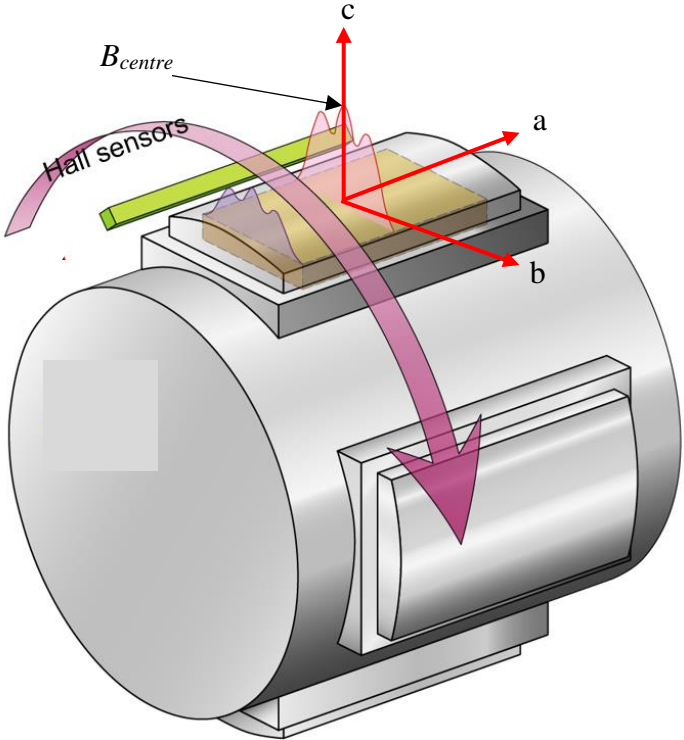

Figure 5-3. Schematic profile of the trapped flux profile after FC magnetization procedure. The trapped field is the maximum at the center of the field pole and decreases towards the edges of the pole.

Table 5-1. Magnetic field at the surface of the pole (rotor) before stator installation and the airgap field (airgap) after stator installation.

Magnetizing Field (T)		Magnetic Field (T)			
		Pole A	Pole B	Pole C	Pole D
1 T	Rotor	0.66	0.72	0.67	0.71
	Air-gap	0.84	0.90	0.84	0.89
2 T	Rotor	1.19	1.19	1.17	1.23
	Air-gap	1.38	1.50	1.36	1.49
3 T	Rotor	1.69	1.77	1.73	1.78
	Air-gap	1.97	1.83	1.99	1.84

After stator installation, the magnetic field was measured using the 5 Hall sensors fixed mounted on a stator tooth. Fig 5-4 shows the magnetic flux profile from the stator-mounted Hall sensors in

the airgap measured while rotating the rotor as shown in Fig. 5-3. It corresponds to the radial component of the trapped flux linking the armature. The flux profile across each pole features three distinct peaks corresponding to the three rows across the b-axis. Unlike the bell-shaped profile seen in salient pole PM and wound field machines, this profile is not sinusoidal but resembles a wave with a superposition of harmonics. The airgap field at the CH1 which is located at the center of the tooth with the stator was 1.99 T in the case of 3 T magnetization. In the case of 1 T and 2 T magnetization, it was 0.90 T and 1.49 T respectively.
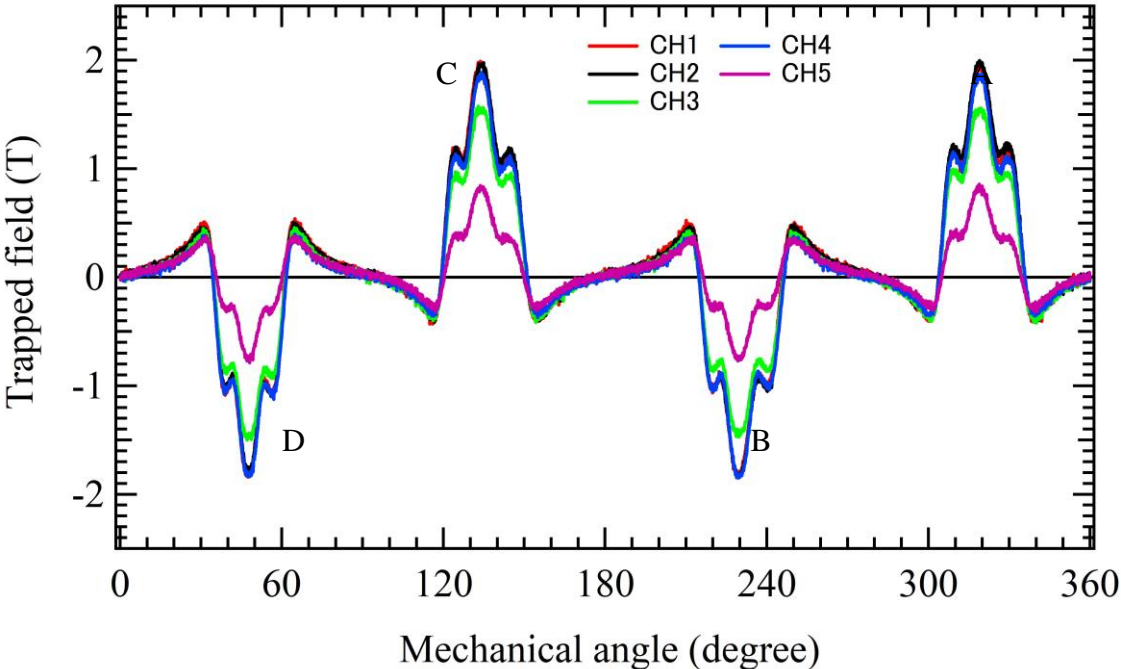

Figure 5-4. Profile of the radial component of the air-gap field, measured across half of each pole after magnetization at 3 T. The flux was measured after stator installation, using the Hall sensors mounted on a stator tooth.

5.3.2 Open-circuit voltage, and open-circuit characteristic curve

In agreement with (5-2), the induced voltage increases linearly with speed for any given flux linkage. Figure 5-5 shows the peak phase voltage induced in the armature windings for speeds between 10 rpm and 220 rpm. The voltage–speed relationship is linear, indicating a very good agreement with (5-2). The peak voltages at the design speed of 190 rpm are 40.6 V, 65.9 V and 93.4 V for 1, 2 and 3 T, respectively. A characteristic curve of induced voltage at the design speed is shown in Fig. 5-6 for the three magnetization levels. It is evident that the voltage curve follows that of the trapped field. Consequently, the conclusion is that the deviation from the linear portion between 0 T ant 1 T is not indicative of saturation in armature teeth.
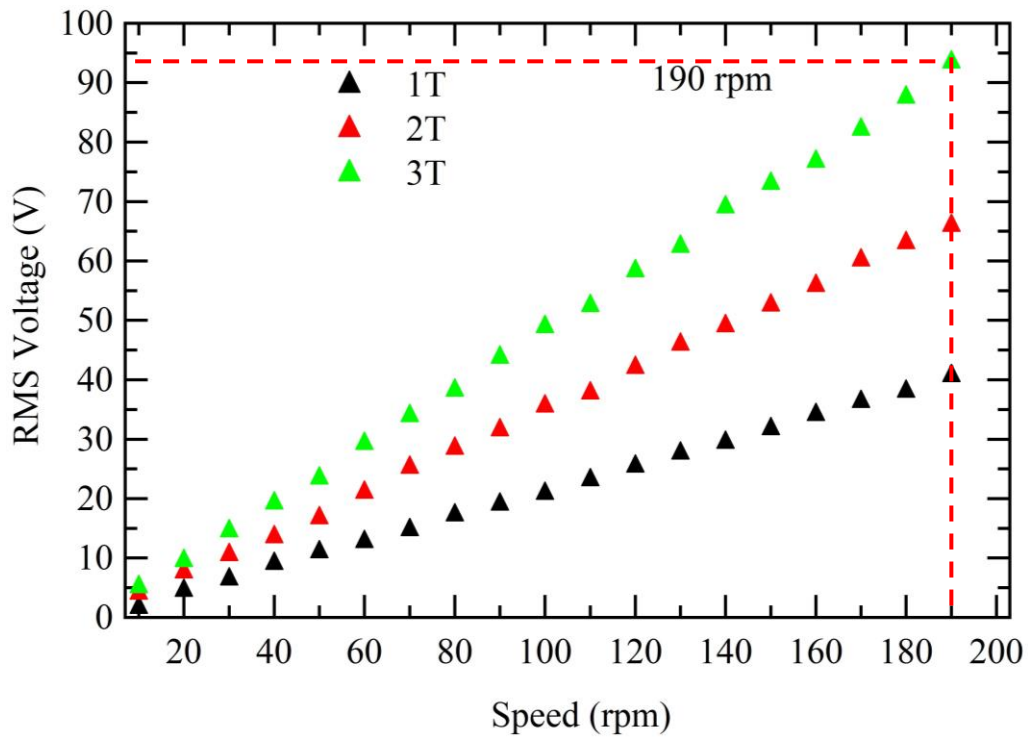
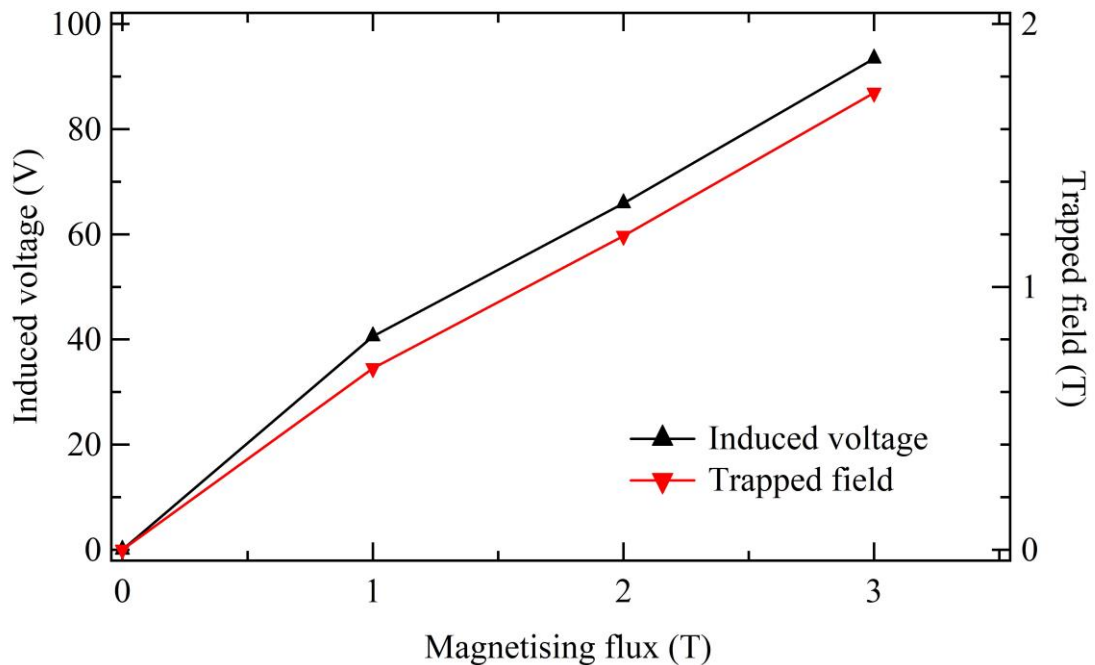Figure 5-5. Induced RMS phase voltage at different speeds.

Figure 5-6. The open-circuit characteristic curve at the design speed of 190 rpm. The induced voltage graph follows that of the tripped flux.

A waveform of the induced voltage in the three phases is indicated in Fig.5-7. A perfect sinusoidal wave is superimposed on phase V for comparison. The induced voltage waveform assumes the

shape of a sinusoid but has harmonics which are a direct result of harmonics in the air-gap flux. A fast Fourier transform (FFT) was conducted on 1 electrical cycle of the induced voltage waveform. The harmonic content by FFT is shown in Fig. 5-8. Harmonics 2-5 are the most dominant compared to the rest, but their normalized magnitudes are less than 0.2 relative to the fundamental.
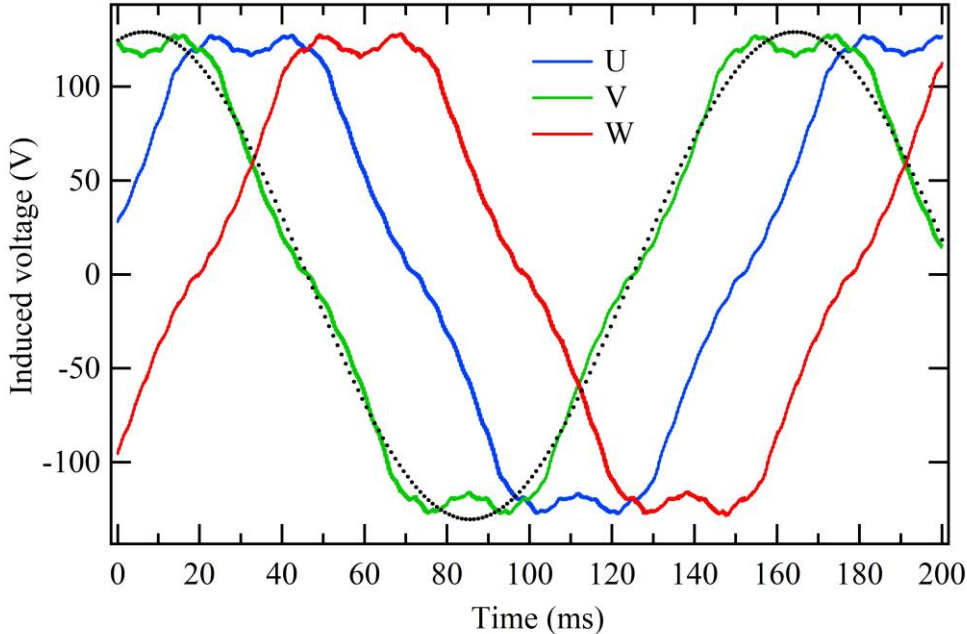

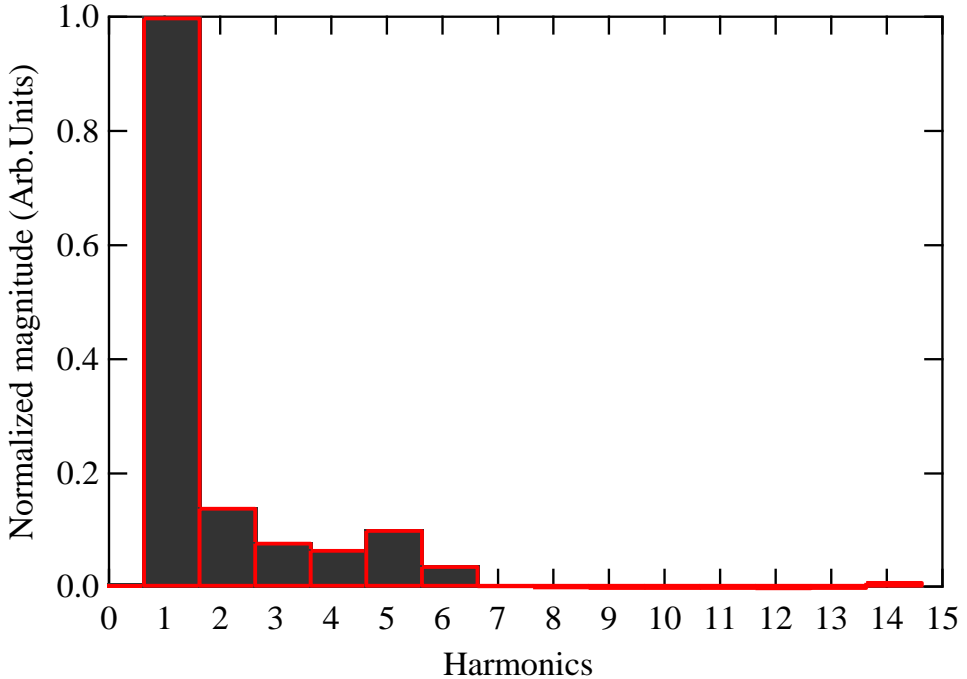Figure 5-7. The waveform of the induced no-load voltage at 3 T, 190 rpm.

Fig. 5-8. Harmonics in the generated voltage waveform of the open-circuit test.

69

5.3.3 Magnetic flux stability

Measurements of the trapped flux were conducted before and after the no-load test. Measurements with Hall sensors indicate that there was no significant change in the trapped flux. Flux linkage calculated using (5-3) from induced voltage and speed data is constant, indicating that the flux did not change during the no-load test. Flux linkage is indicated in Fig.5-9 as a function of speed.
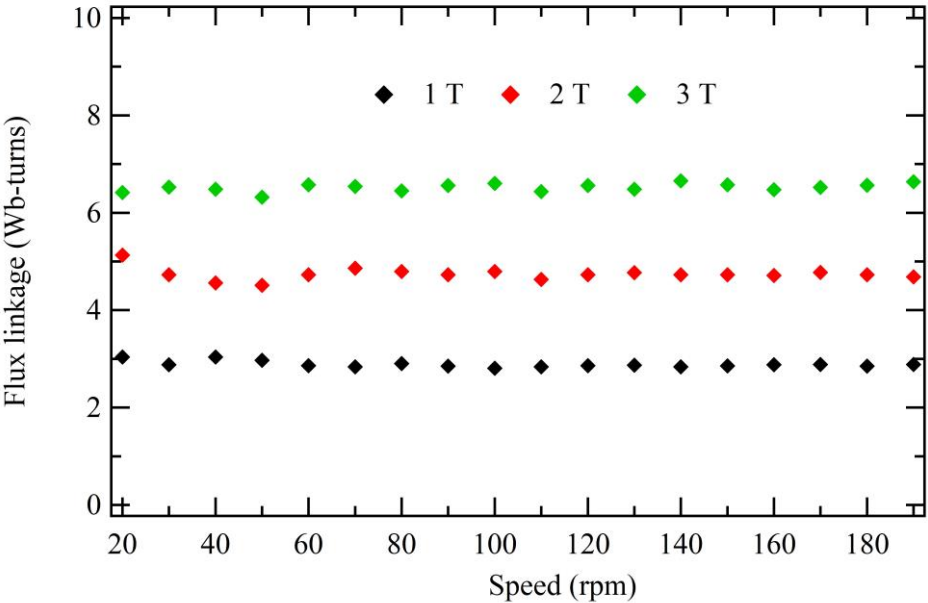

Figure 5-9. Flux linkage at different speeds.

5.3.4 Core Loss

Since the air-gap field is non-sinusoidal, total core loss is a combination of losses due to all harmonics present in the air-gap flux. Total core loss at 1, 2 and 3 T is shown in Fig. 5-10 as a function of speed. Core loss has also been expressed as a specific core loss (core loss per kilogram of core mass) as a function of frequency. Core loss increases with increasing rotor trapped flux and frequency (rotor speed) as suggested by Steinmetz and Bertotti core loss models. At the rated speed of 190 rpm (6.33 Hz), the no-load core losses are 164 W, 369 W and 577 W at 1, 2 and 3 T rotor magnetization, respectively. Specific core loss at 190 rpm is 0.46 W/kg, 1.03 W/kg and 1.61 W/kg at 1, 2 and 3 T, respectively. The temperature increase of the armature core during core loss testing was 2 K, with the maximum recorded temperature of 299.4 K (26.2 °C) when the rotor was magnetized at 3 T. However, if magnetized above 3 T, core losses and consequently temperature may increase significantly. Core losses are therefore detrimental to the efficiency of electrical machines and therefore, to leverage the high field of bulk HTS without suffering core loss penalty, it is imperative to use non-magnetic composite armature teeth.
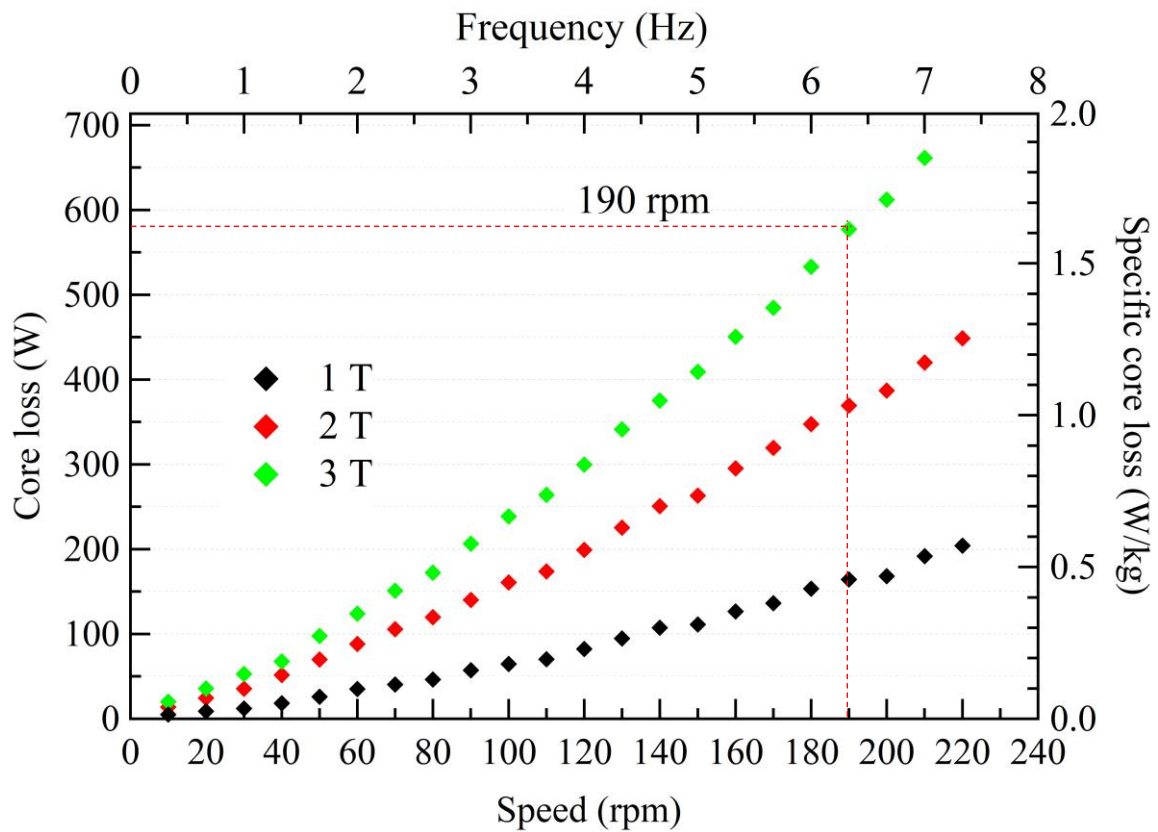
70

Figure 5-10 Total core loss as a function of rotor speed. The machine was run from 10 rpm to 220 rpm with the speed being incremented by 10 rpm.

5.4 Discussion

A 30-kW prototype HTS bulk synchronous machine composed of 15 GdBCO bulks was tested at 1, 2 and 3 T. No-load tests were conducted, and the open-circuit characteristic curve has been obtained. Core loss has been experimentally determined. Due to the nature of the trapped flux, air-gap flux has harmonics that show up in the terminal voltage of the machine. As expected, core losses increase with increasing rotor speed and magnetic flux density. The presence of harmonics in the air-gap flux increase core loss. A temperature rise of approximately 2 K was recorded in the armature core during no-load tests. Thus, it is plausible that harmonics may adversely affect the efficiency of this machine topology, especially at high speeds and flux densities. Similar machines can, therefore, benefit from the large integrated flux of these trapped field magnets if composite teeth are used instead of ferromagnetic teeth. Compared to a wound-field HTS machine, the bulk HTS machine has more harmonics in its terminal voltage due to the highly non-sinusoidal shape of the trapped field.

71

Chapter VI Bulk HTS machine load tests

One of the main concerns regarding the use of bulk HTS is the possibility of demagnetization due to the perturbation of cross fields. Bulks on the rotor are inevitably subjected to a changing magnetic field of the armature. In this chapter, the bulk HTS machine is tested as a motor after magnetization at 1, 2, and 3 T. It should be noted that this bulk motor has a rated power of 30 kW at 190 rpm at 5 T magnetization, therefore tests herein were conducted at lower magnetic field loadings.

6.1 Bulk HTS machine load testbed

6.1.1 Load test set-up

The bulk HTS machine was tested as a motor connected to the same 14.9 kW pony motor which acts as load motor. The speed of the pony motor is varied using the ACS800 variable speed drive, while the bulk HTS motor was powered by another commercial ABB (ACS 880) variable speed drive with at output power rating of up to 261 kW. The ACS 880 has a direct torque control (DTC) capability, feature that was exploited in conducting these load tests, as explained in section 6.1.2. Figure 6-1 shows the setup of the testbed.
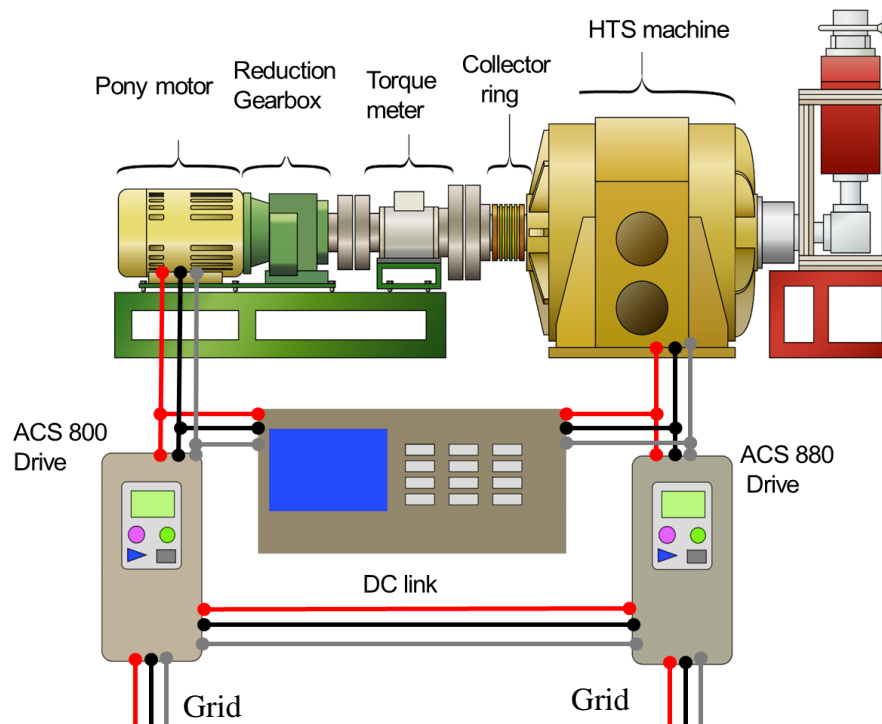

Figure 6-1. HTS machine load test bed.

6.1.2 DTC and ID run

DTC is a control method that relies on the stator flux and torque as primary control variables. When the ACS880-01 is set to DTC mode, it allows for accurate control of the motor speed and torque without the need for motor shaft encoder. After magnetization and prior to any load test, the HTS motor is decoupled from the pony motor so that the ACS880-01 drive performs a DTC identification (ID) run. During an (ID) run, the nameplate nominal voltage, current, frequency, speed and power of the HTS motor are entered, and the ACS880-01 drive accelerates the HTS motor to its nominal speed of 190 rpm to confirm the entered parameters. The nominal voltage of the HTS machine is the same as the back EMF at nominal speed obtained from the no-load tests. The nominal power at 1, 2, and 3 T levels of magnetization was unknown and therefore had to be estimated. If any data in the nameplate data set is incorrect, the ID run indicates an error. Upon conducting a successful ID run in DTC mode, the ACS880-01 uses the ID run data to calculate the maximum torque that the HTS motor can produce at each level of magnetization. This maximum torque is displayed on the ACS880-01 as 100 %. The nameplate data of the HTS machine at 1, 2, and 3 T magnetization was obtained and is listed in table 6-1.

Table 6-1. Nameplate data of the bulk HTS motor entered ID run.

Parameter	1.0 T	2.0 T	3.0 T
Motor nominal current (A)	58.6	55.8	54.6
Motor nominal voltage (V)	75.0	130	185
Motor nominal frequency (Hz)	6.33	6.33	6.33
Motor nominal speed (rpm)	190	190	190
Motor nominal power (kW)	4.2	7.25	10.1

6.1.3 Load test method

To execute a load test, the rotor of the HTS motor is driven to the desired speed first, using the pony motor. Next, the stator of the HTS motor is then powered using the ACS880-01 drive in DTC mode, to exert a torque opposite to that of the pony motor. This counteractive torque can be varied from 0 – 100 % where 100 % is the maximum torque value which the ACS880-01 computed during the ID run. When the counteractive torque increased to 100 % at 190 rpm, the HTS motor will be running at full load. Load tests were conducted speeds between 50 rpm and 190 rpm in 10 rpm

increments. For each speed, the torque of the HTS motor was varied from 0 % to 100 % in 20 % increments. The power developed by the HTS motor is at any speed ω, is given by (6-1).

$$P = (\tau - \tau_0)\,\omega$$

<div align="right">(6-1)</div>

where τ is the torque measure during the load test and τ_0 is the torque measured during the no-load test (core,and friction and windage losses).

6.2 Results

6.2.1 Motor output power

Figure 6-2. shows the torque and speed curves during the load test at 2 T magnetization. The speed was varied between 50 and 190 rpm in 10 rpm increments, while the torque of the ACS880-01 drive was systematically increased from 0 % to 100 % in 20 % increments. At 2 T, the torque meter measures 381.8 Nm when the ACS880-01 torque value is 100 %.
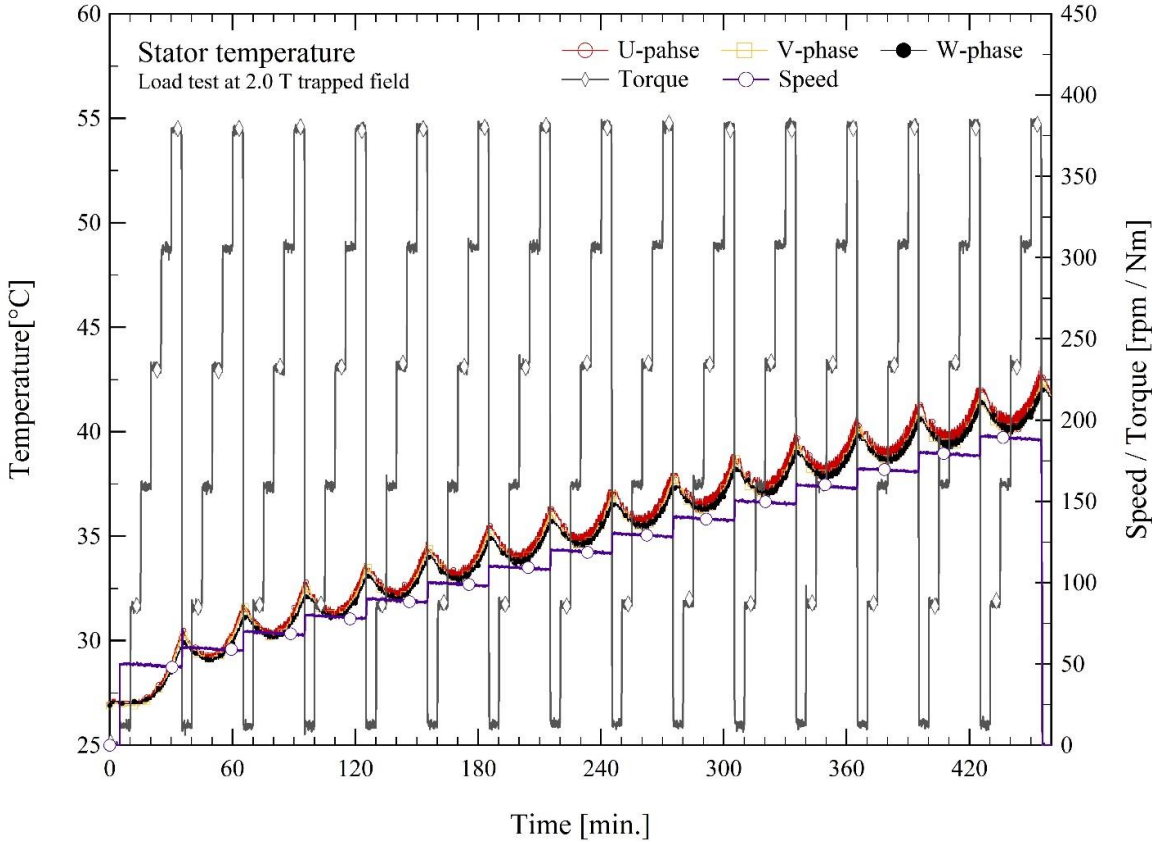

Figure 6-2. Bulk HTS motor load test at 2 T. The load torque of the HTS motor was varied from 0 % to 100 % in 20 % increments.

Using equation (6-1), the power developed by the HTS motor at different speeds was computed and is shown in Fig. 6-3. The maximum power obtained at approximately 190 rpm was 7.26 kW.

Figure 6-3. The power-speed curve of the bulk HTS motor at 2 T magnetizing field.

Fig. 6-4 shows the torque and speed curves during the load test for 3 T magnetization. The speed was also varied between 50 and 190 rpm. The torque of the ACS 880 drive was increased from 0 % to 100 % in 20 % increments. The maximum torque measured by the torque meter was 540.8 Nm when the ACS880-01 torque value is 100 %. Using equation (6-1), the power developed by the HTS motor at different speeds was computed and is shown in Fig. 6-5. The maximum power obtained at ap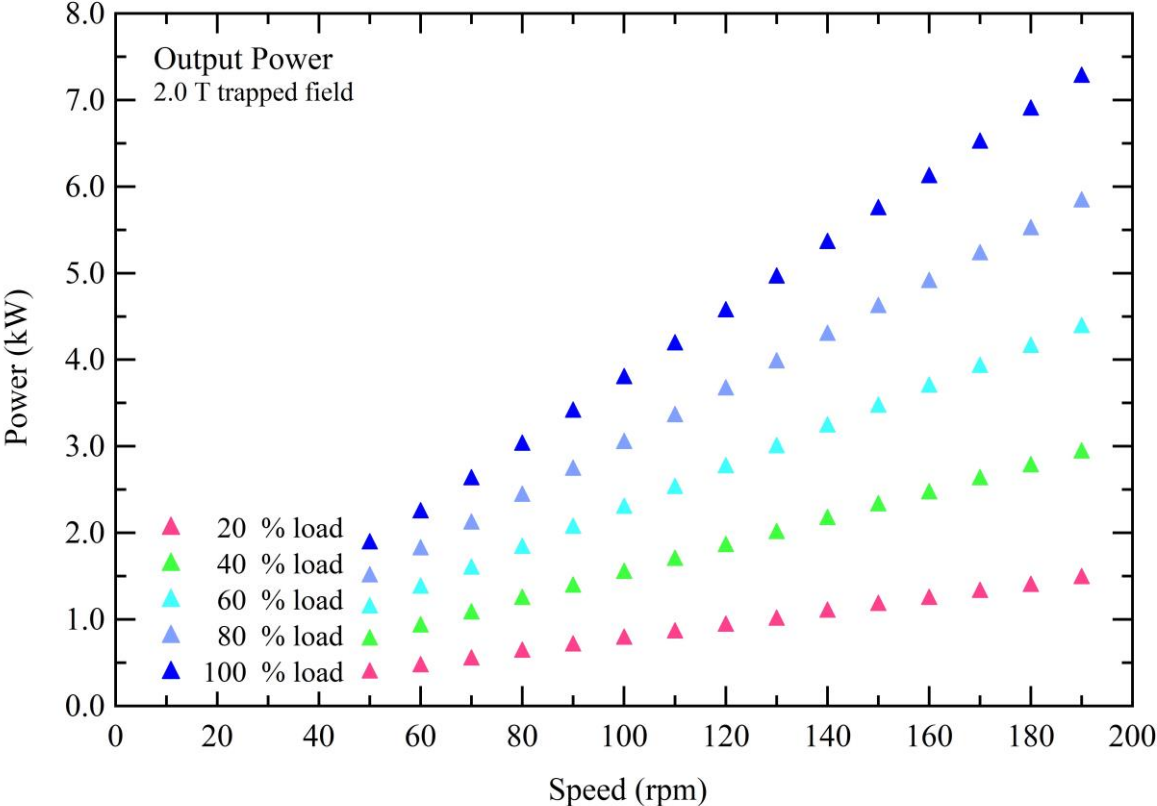proximately 190 rpm was 10.1 kW. In the case of 1 T, the maximum torque measured by the torque meter was 222.0 Nm when the ACS880-01 torque value is 100 %, and the maximum power at approximately 190 rpm reached 4.2 kW.
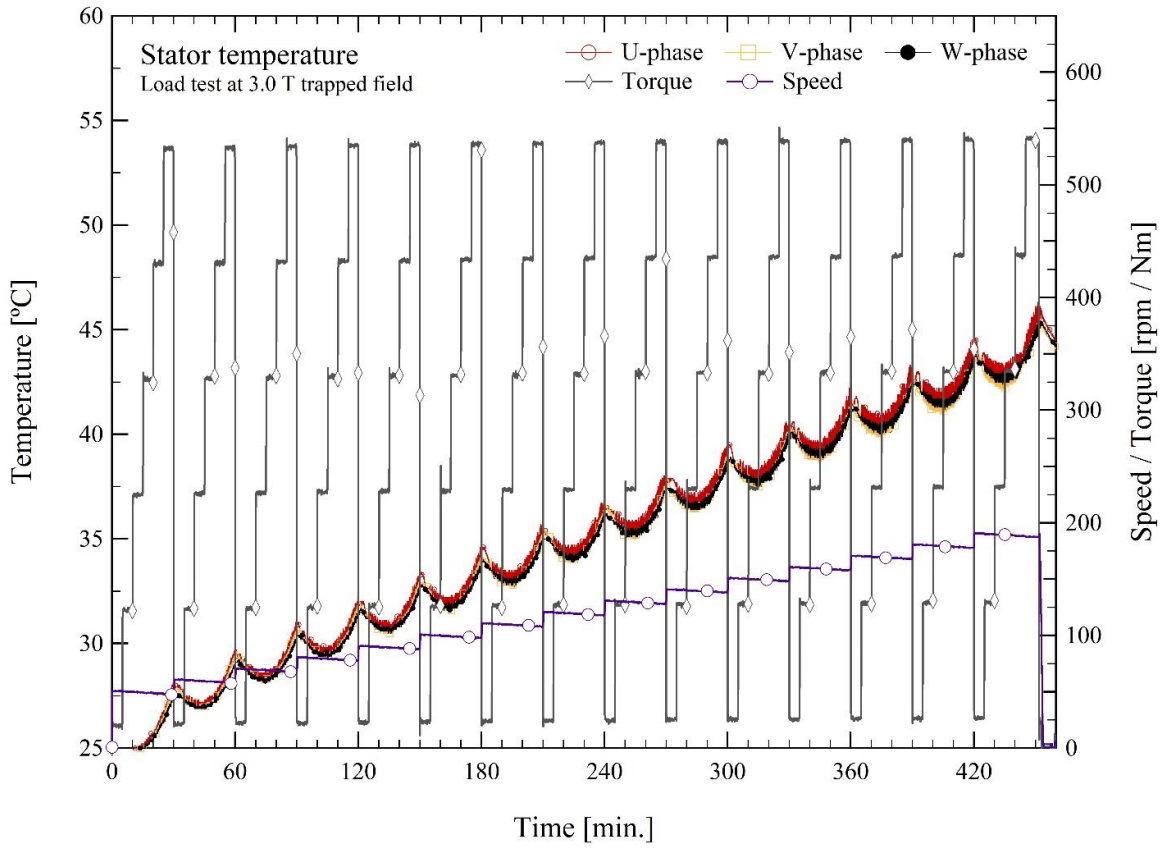
Figure 6-4. Bulk HTS motor load test at 3 T. The load torque of the HTS motor was varied from 0 % to 100 % in 20 % increments.
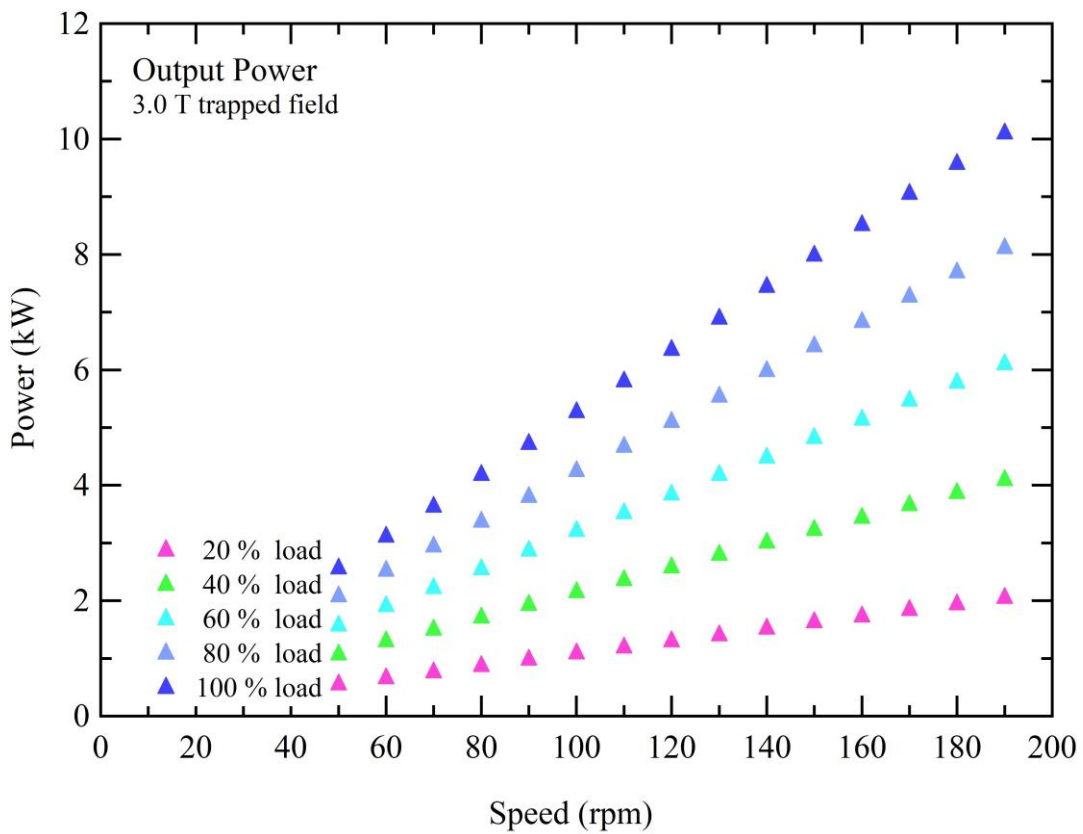
Figure 6-5. The power-speed curve of the bulk HTS motor at 3 T magnetizing field.

6.2.2 Long-run tests and trapped flux Stability

To assess whether the bulk HTS motor can keep its trapped field for extended periods, a series of long-run tests at 3 T. First, the motor was run at full load and rated speed for 100 consecutive hours, the graph of which is indicated in Fig.6-6. The second long-run test lasted for 360 consecutive hours, the graph of which is shown in Fig. 6-7.
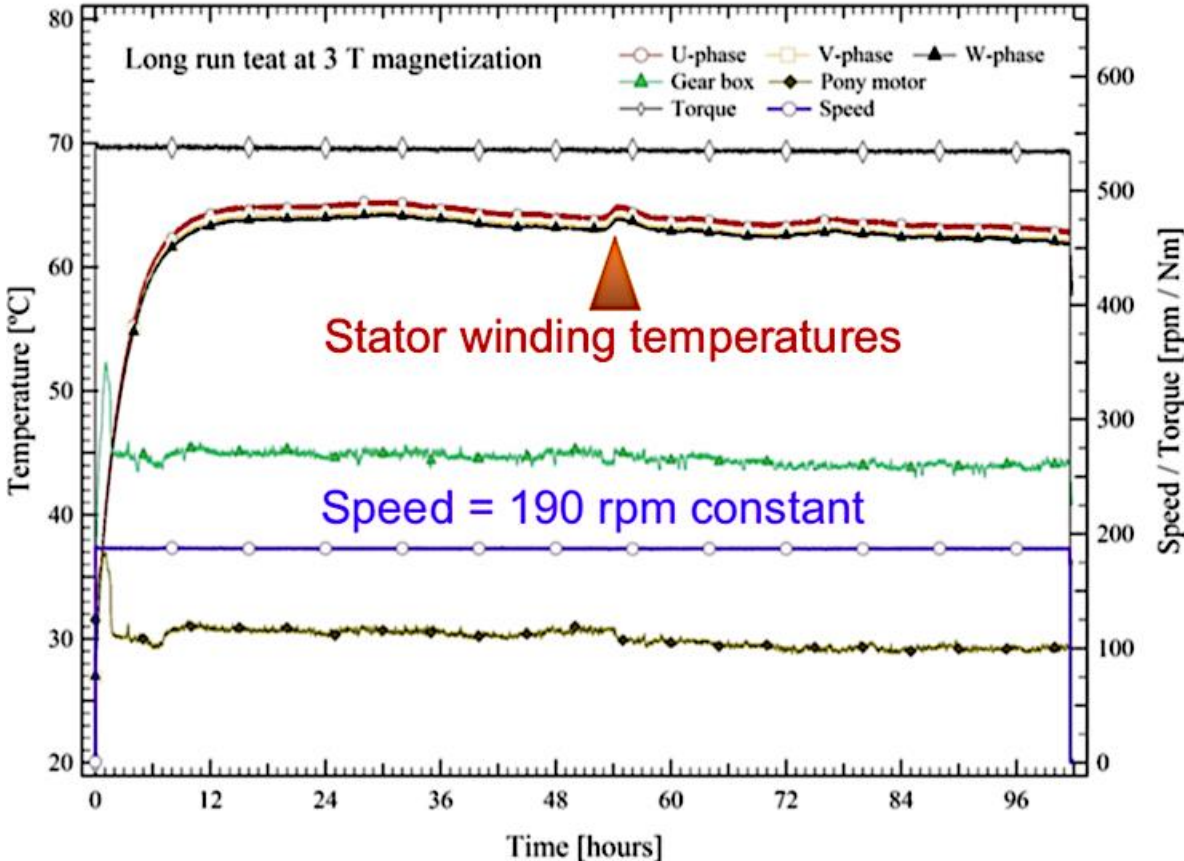
Figure 6-6. The full load test at rated speed for 100 hours at 3 T. The speed and torque remained constant throughout the test.
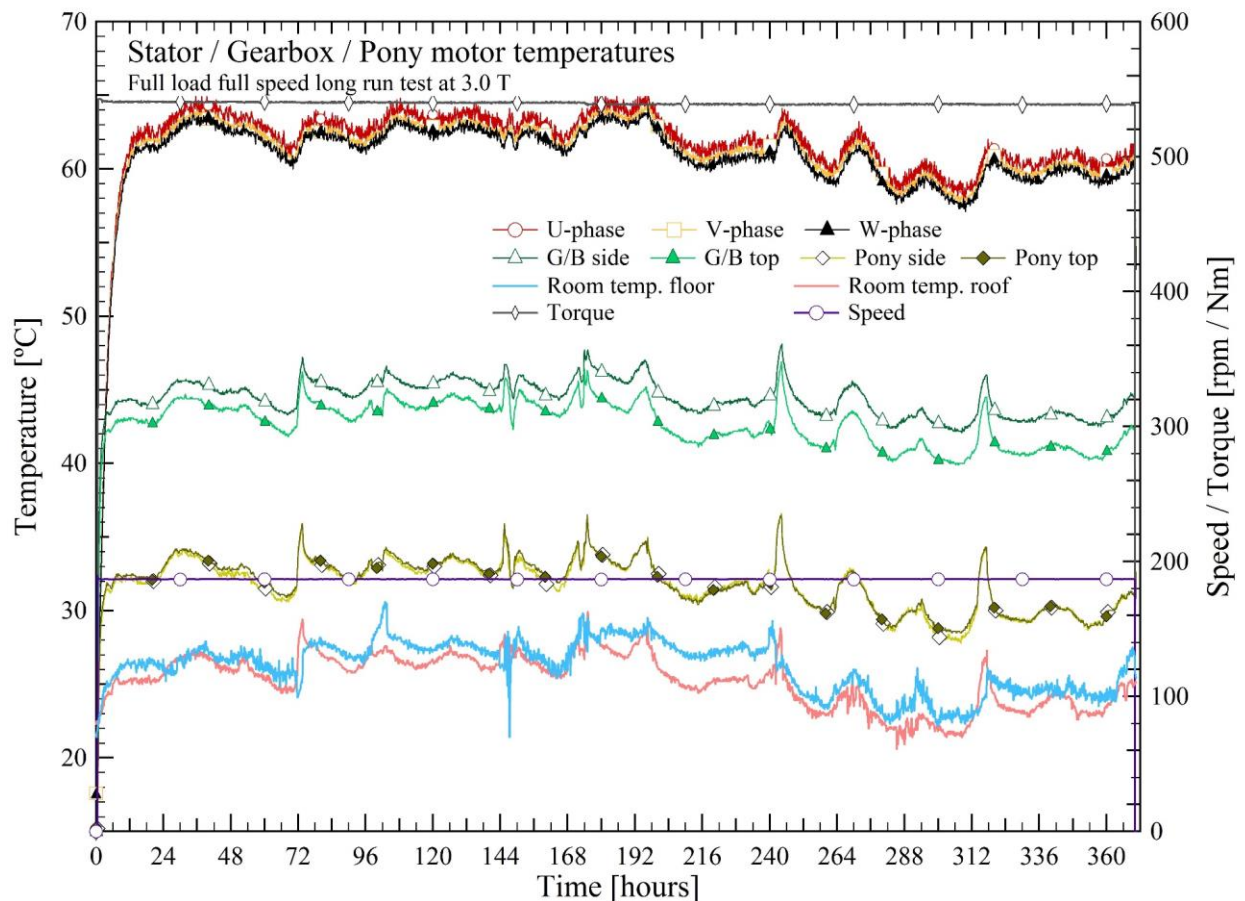
Figure 6-7. Full load test at rated speed for 360 hours at 3 T.

Both graphs indicate that both the speed and torque remained constant throughout the long run test. This, by extension, means that the flux of the HTS motor did not change.in spite of magnetic flux perturbations of the stator armature. Indeed, flux measurements using Hall sensors indicate that there was no significant change after no-load, load tests and long-run load tests. Only a decrease of less than 1 % has been measured as table 6-2 indicates.

Table 6-2 Normalised trapped flux after no-load and load tests

	CH 1	CH 2	CH 3	CH 4	CH 5
Initial (%)	100	100	100	100	100
After no load test (%)	100	100	100	99.9	100
After load test (%)	99.9	99.9	100	99.7	99.4

6.2.3 Cooling system performance

The temperature of the poles during load tests at 2 and 3 T are indicated in Fig. 6-8 and 6-9.

Figure 6-8. Temperature during load test at 3 T.

Figure 6-9. Temperature during load test at 3 T.

This thermosyphon differs from that in chapter III in that centrifugal forces act on the evaporator as the HTs motor rotates. Centrifugal forces cause a film of condensate to form all around the evaporator thereby enhancing cooling. Additionally, the liquid in the evaporator recirculates as the evaporator rotates, removing any temperature gradients in the liquid as shown in figure -9. This has an effect of flattening temperature across the poles.
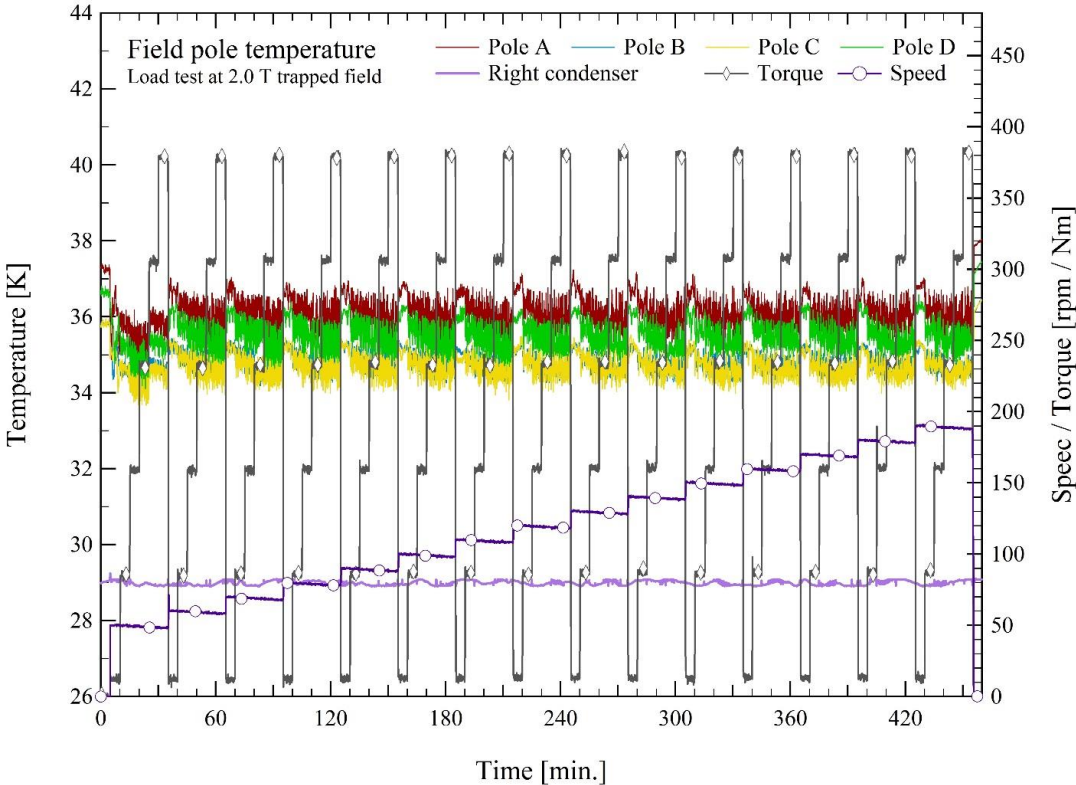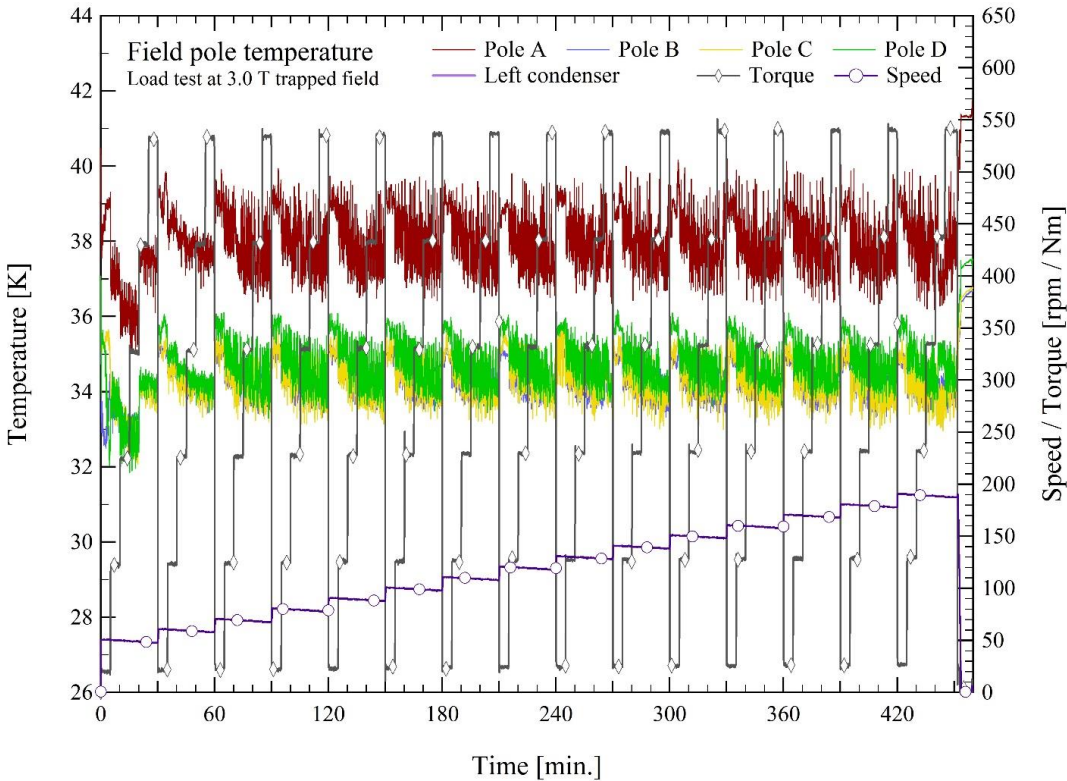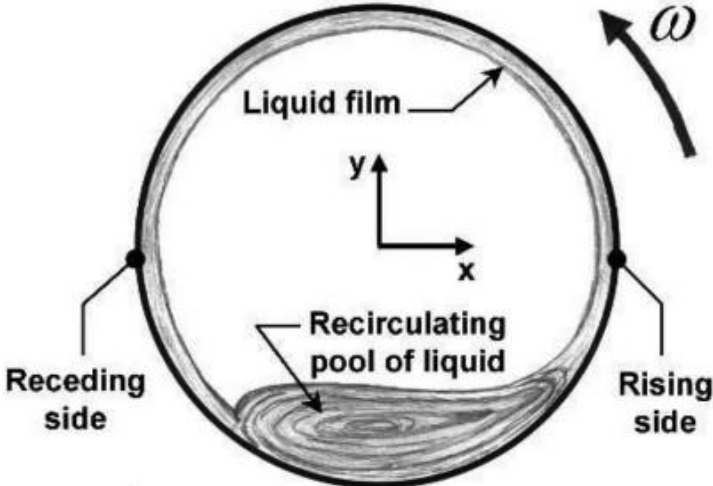

Figure 6-10. Liquid firm and motion in a rotating evaporator.

6.2.4 Motor performance after loss of cryocooler power

One of the contingencies of HTS power systems is the failure of the cooling system. To avoid catastrophe, the time available before the HTS device reaches 80 K after cooling system failure must be long enough to allow sufficient time for operators to activate contingency plans to make the system resilient. This time can be extended by adding a cryogenic thermal storage buffer of some kind which increases the heat absorption capacity of the device to avoid temperature increase.

To test the robustness of the motor, this condition was studied by switching off all cryocoolers at the same time, while the machine was at standstill with the rotor magnetized at 3 T. The decay of the trapped field as a function of the elapsed time is shown in Fig. 6-11. The magnetic flux density in the airgap remained constant until it reduced to 99 %, 90 % and 80 % of its initial value after 23, 36 and 51 minutes, respectively. The temperature of the pole was 49.3 K, and 49.4 K at the centre and edge, respectively when the drop to 99 % was detected.
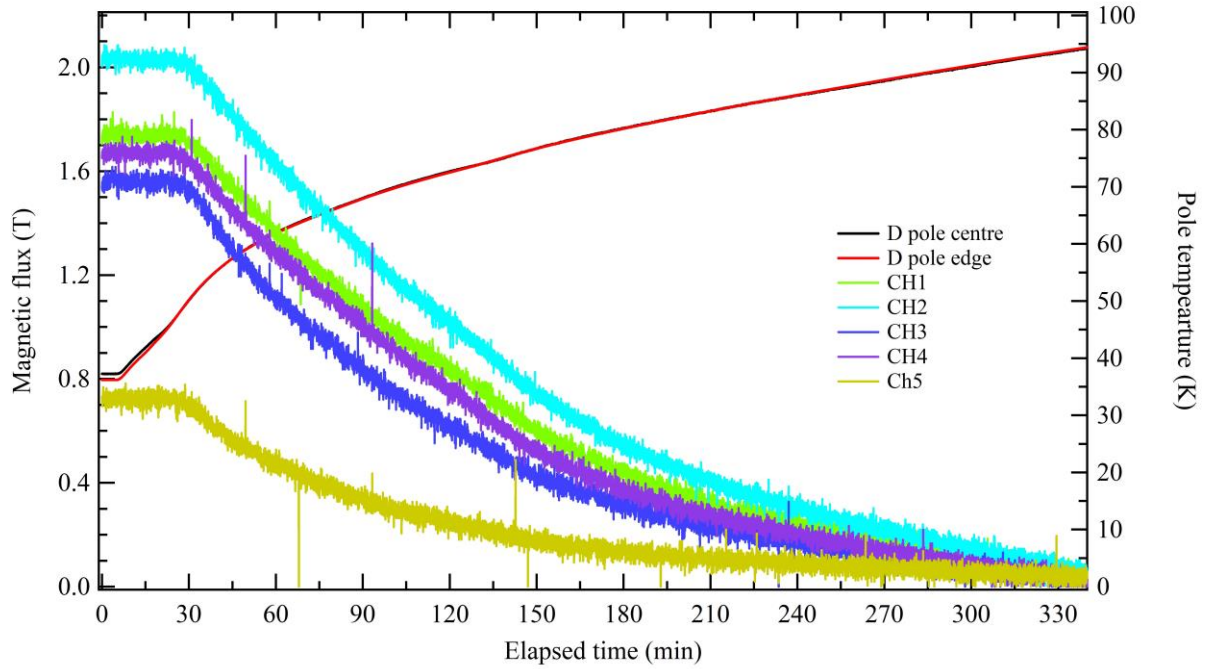
Figure 6-11. Evolution of pole D temperature and trapped flux after cryocooler is stopped.

Also, as a worst-case scenario, this condition was studied by switching off all cryocoolers at the same time, while the machine was running at full load at 1 T. The output power of the HTS motor was monitored as a function of elapsed time after cryocooler was switched off as shown in Fig.6-12. The test was stopped after 156 minutes, and the remaining magnetic field was measured.
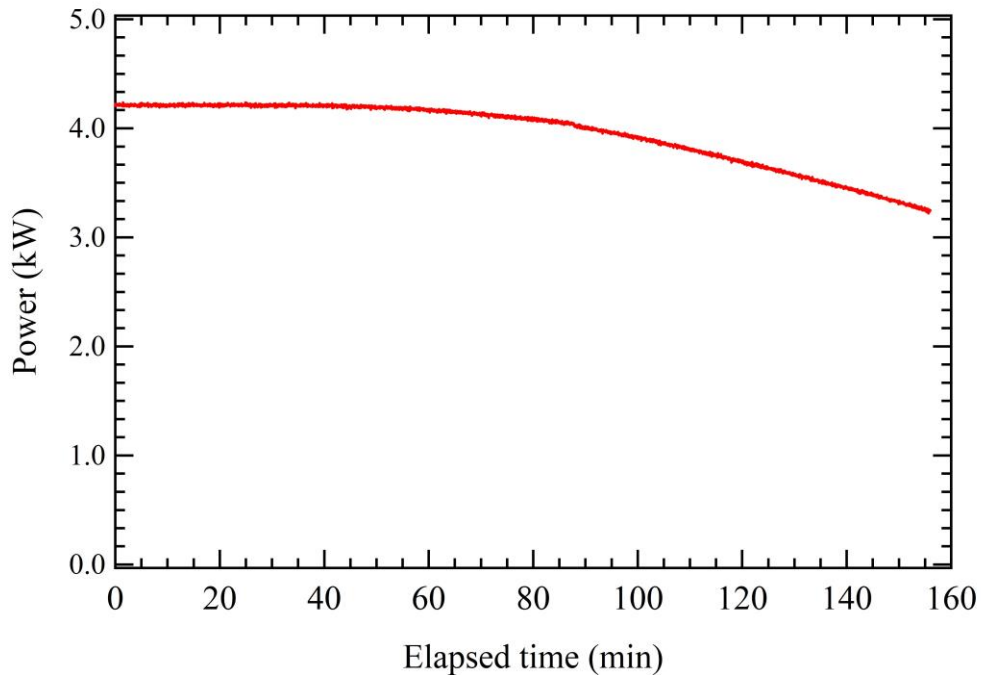
Figure 6-12. The evolution of output power after the cryocoolers were turned off.

The output power of the HTS motor remained constant for nearly 42 minutes after the cryocoolers were shut down. It took 59 minutes for the output to drop by 1 % to 99 %, while it took 1 hour 47 minutes 2 hours 23 minutes for the power to reduce to 90 % and 80 % of its initial value, respectively. The bulk HTS machine allows sufficient time to start up a standby cooling system. Liquid neon inside the evaporator and high heat capacity of the bulk and copper, all acted as a buffer, slowing down temperature increase. After the loss of cooling power, the bulks retained their magnetic field for some time. This can be attributed to two factors; the high heat capacity of GdBCO employed on the rotor which enables absorption of transient thermal loads with little temperature rise, and the presence of the liquid neon pool in the evaporator which as a storage buffer. The magnetic field graphs before and after the cryocooler loss load test are shown in Fig. 6-13 and 6-14, respectively.
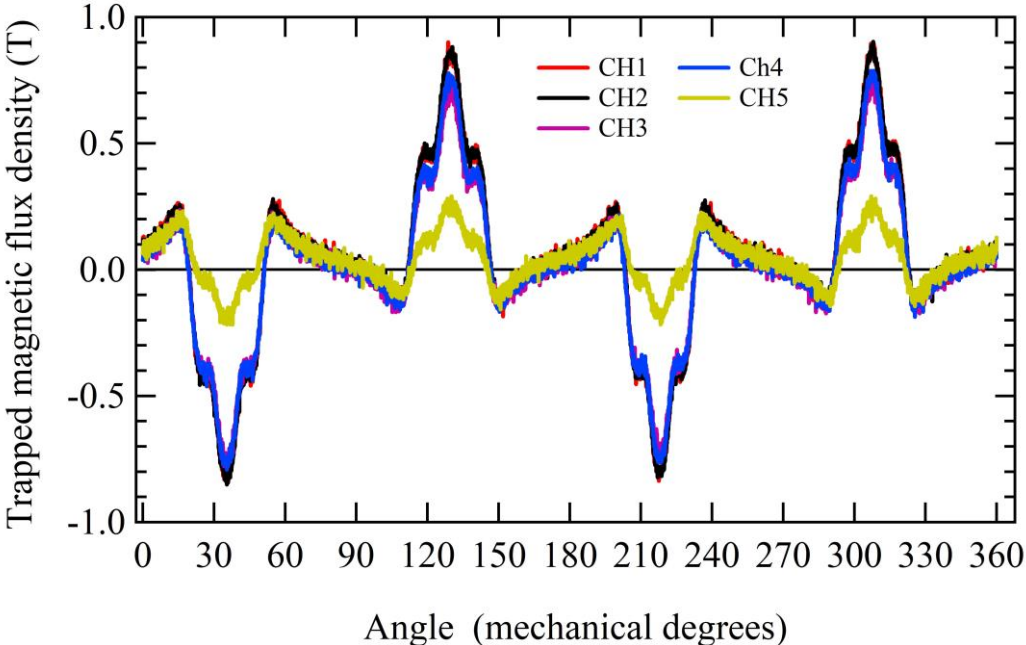
Figure 6-13. Magnetic flux before cryocooler loss experiment. Maximum trapped field: CH1 = 0.90 T, CH2 = 0.90 T, CH3 = 0.74 T, CH4 = 0.79 T, CH5 = 0.29 T.
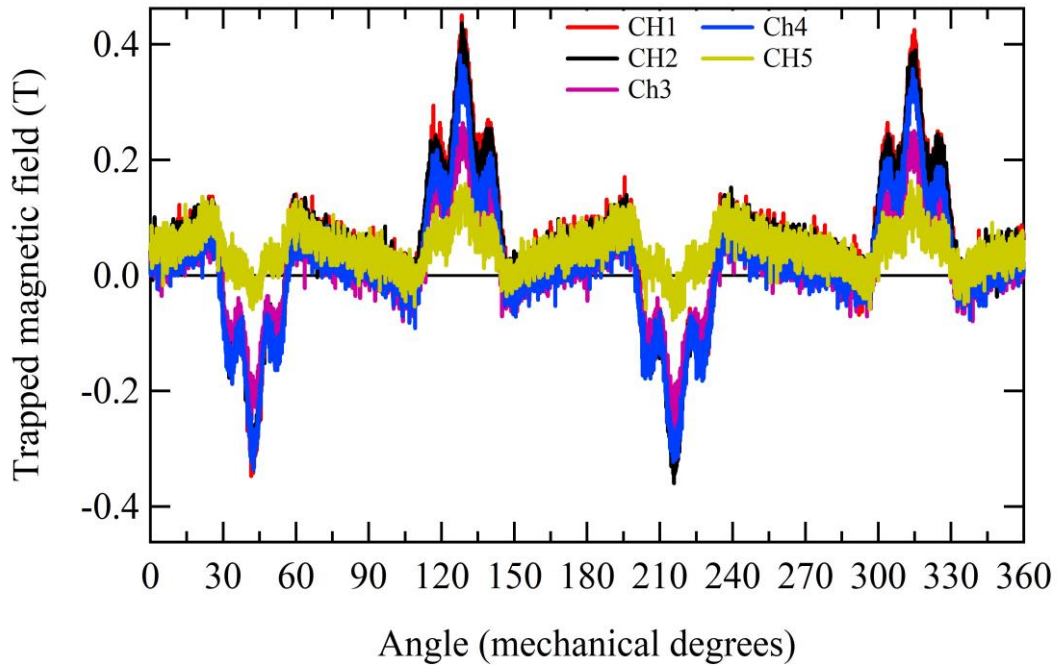
Figure 6-14. Th remaining magnetic field 156 minutes after the cryocooler was switched off. The remaining field measured as: CH1 = 0.45 T, CH2 = 0.44 T, CH3 = 0.26, CH4 = 0.38 T, CH5 =0.16 T.

6.3 Conclusion

The HTS machine was tested under no-load and load tests at 1, 2, and 3 T. A maximum of 10.05 kW was attained at 3 T load test. The machine was also operated at full load for up to 360 consecutive hours, showing no degradation in output power. The trapped flux exhibits stability before and after no-load and load tests at 3 T trapped field were investigated. So far, flux density exhibited an insignificant decrease of less than 1 %. This shows us again that no drastic demagnetization can be observed unlike described in the other research reports. The bulk motor also exhibited an advantage over HTS wires and tapes as it can retain its magnetic field in spite of cryocooler loss. These results are invaluable in indicating that bulk HTS machines are robust, in terms of trapped magnetic field and thermal stability. Motors with HTS winding would not have this advantage as the current in the field winding would cause the temperature of the rotor to raise rapidly, leading the quenching.

Chapter VII Summary and prospects

Temperature is a critical factor in the application of superconductors. Thermosyphon cooling systems provide reliable, high heat transfer rates and near-isothermal cooling. In thermosyphon-cooled superconducting machines, superconductor field poles are mounted on the periphery of an evaporator. It is, therefore, crucial to know the temperature of all points of the evaporator. In this thesis, experimental work was conducted to gather data from a stand-alone neon thermosyphon cooling system. Experimental results were obtained by applying heat loads to the evaporator. Further, a thermal analysis was conducted, and boundary conditions were identified to enable estimation of evaporator temperature distribution and heat invasion using a computer. The thermal effect of the MLI which is used as a thermal control element has been modelled as effective emissivity.

A comparison of experimental and estimated data suggests that a reasonable estimation of the temperature distribution of the evaporator was obtained. It is noteworthy that the effective emissivity value falls well within the effective emissivity rage found in the literature. The close proximity of simulation results to experimental data suggests that simulation results can be used to estimate temperature distribution or validate temperature sensor readings. An effective emissivity approach may also be useful in estimating heat invasion during the design of cooling systems that employ MLI. The model also provided further insight into how heat leaks into the thermosyphon. Although the thermosyphon studied has a stationary evaporator, it provided background knowledge

In order to explore the potential of bulk HTS machines and validate the technologies required to develop them, a 30-kW low-speed, radial-gap synchronous motor prototype was developed. The motor was designed as a ship propulsion motor motor prototype with a rated speed of 190 rpm. Its rotor features 4 poles with 15 GdBCO square bulks. The rotor operates at 30 K, cooled by a thermosyphon cooling system. The motor was installed in a testbed, magnetized at 1, 2, and 3 T, and series of tests were conducted on it to assess the performance, especially the stability of the trapped magnetic field.

No-load tests were conducted, and the open-circuit characteristic curve has been obtained. Core loss has been experimentally determined. Due to the nature of the trapped flux, air-gap flux reveals harmonics that show up in the terminal voltage of the machine. The presence of harmonics in the air-gap flux increase core loss. As expected, core losses increase with increasing rotor speed and trapped magnetic flux density. A temperature rise of approximately 2 K was recorded in the

armature core during no-load tests. Thus, it is expected that harmonics may adversely affect the efficiency of this machine topology, especially at high speeds and flux densities. Similar machines can, therefore, benefit from the large integrated flux of these trapped field magnets if composite teeth are used instead of ferromagnetic teeth. Compared to a wound-field HTS machine, the bulk HTS machine has more harmonics in its terminal voltage due to the highly non-sinusoidal shape of the trapped field.

The HTS machine was also tested under load tests at 1, 2, and 3 T. A maximum of 10.05 kW was attained at 3 T load test. The machine was also operated at full load for up to 360 consecutive hours, showing no degradation in output power. The stability of the trapped magnetic field before and after no-load and load tests at 1, 2, and 3 T trapped field was investigated. Only an insignificant decrease of less than 1 % has been observed, which is within the error range of the Bell Hall sensors. This shows us again that no drastic demagnetization has be observed in a synchronous machine operating at low speeds. The robustness of the motor in terms of its trapped field was also studied by switching off all cryocoolers at the same time. In one case, the cryocoolers were switched of while the machine was at standstill with the rotor magnetized at 3 T. The magnetic flux density in the airgap remained constant until it reduced to 99 %, 90 % and 80 % of its initial value after 23, 36 and 51 minutes, respectively. The temperature of the pole was 49.3 K, and 49.4 K at the center and edge, respectively when the drop to 99 % was detected.

In another case, the cryocoolers were switched off while the machine was running at full load at 1 T. The test was stopped after 156 minutes, and the remaining magnetic field measured. The output power of the HTS motor remained constant for nearly 42 minutes after the cryocoolers were shut down. It took 59 minutes for the output to drop by 1 % to 99 %, while it took 1 hour 47 minutes 2 hours 23 minutes for the power to reduce to 90 % and 80 % of its initial value, respectively. The conclusion is therefore that the bulk HTS machine allows sufficient time for an operator to start up any standby cooling system to maintain normal motor operation. This was made possible by the liquid neon buffer of the thermosyphon as well the high heat capacity of both the bulks and copper inside the evaporator.

As far as bulk HTS machine development is concerned, the stability of the trapped field results obtained in this study indicate that bulk HTS could find a niche application in low speed machines such as ship propulsion motors and wind generators. However, more research is necessary to determine if the field is stable at high speeds.

Acknowledgements

I wish to acknowledge family, friends, colleagues and academics supervisors without whose help I could not have come this far. I am deeply indebted to my immediate supervisor, Professor Mitsuru IZUMI, for guiding and shaping me and the whole student community if Tokyo University of Marine Science and Technology and beyond. I would also like to express gratitude towards my co-supervisors, Professor Satoshi YOSHIOKA, Professor Tetsuya IDA, and Professor Hitoshi OHNUKI. Your supervision and dedication to ensure that students like myself get the necessary guidance and support to grow and become seasoned researchers are highly appreciated. I wish you good health as you continue serving humanity.

I could not have done all this work all by myself. Indeed, I have had to work together with my laboratory colleagues to conduct experiments. I have heavily relied on the technical expertise of Dr. Motohiro MIKI who has been the beating heart of our laboratory team. I will forever treasure and be grateful for your lessons in many aspects of my study. I am also grateful to Mr. Clement BOCQUEL, Dr, Kota YAMAGUCHI, Dr. Li ZHI, Dr. Jing HAILIAN, and Dr. Yuanyuan XU. I am incredibly privileged to have worked alongside all of you. We have been a tight-knit team and have accomplished a lot together. I appreciate you all. My gratitude also goes all my other former fellow students, too numerous to mention, for their support. I have had issues due to the language barrier, but you always render assistance whenever I needed some. It is my sincere hope that we get to cross paths again and again in the future.

As the Laboratory of Applied Physics, we wish to that the following corporate partners, without whose cooperation this work would not have been possible.

Mr. Y. Murase, Mr. T. Oryu, and Dr. T. Yanamoto from Kawasaki Heavy Industries Ltd., with whom we worked together on thermosyphon system.

Dr. Mitsuru Morita, and Dr. Hidekazu Teshima of Advanced Technology Research Laboratories, Nippon Steel Corporation, Dr. Steven Englebretson of ABB Corporate Research Center, Raleigh, North Carolina, United States, Dr. Robert Chin of ABB Corporate Research, Vasteras, Sweden, and Dr. Jere Kolehmainen, formerly of Motors and Generators, ABB OY, Vaasa, Finland, who have been instrumental in the development and testing of the bulk HTS machine. We could not have conducted a study of this magnitude without your assistance and the financial assistance of your esteemed companies.

References

[1] V. Ginzburg and E. A. Andryushin, Supercoductivity (Revised Edition), World Scientific Publishing: Toh Tuck Link, 2004.

[2] H. K. Onnes, "The resistance of pure mercury at helium temperatures," *Commun. Phys. Lab.,* vol. 12, p. 120, 1911.

[3] A. Mourachkine, "Introduction," in *Room-temperature Superconductivity*, Cambridge, UK:, Cambridge, 2004, ch. 1, p. 4.

[4] J. G. Bednorz and K. A. Mueller, "Perovskite-type Oxides - The New Approach to High Tc Superconductivity. Nobel Lecture," *Angewandte Chemie-international Edition - ANGEW CHEM INT ED,* vol. 27, pp. 735-748, 1988, DOI:10.1002/anie.198807351.

[5] C. M. Rey and A. P. Malozemoff, "Fundamentals of Superconductivity," in *Superconductors in the Power Grid*, C. Rey, Ed., USA, Woodhead Publishing, 2015, pp. 29-73.

[6] S. S. Kalsi, "HTS Superconductors," in *Applications of High Temperature to Electric Power Equipment*, Ney Jersey, , USA: John Wiley & Sons, Inc., 2011, ch. 2, pp. 8.

[7] C. W. Chu and A. J. Jacobson, "HTS/LH2 Supergrid: An Energy Super Highway in the U.S. for the New Millenium," *Institute of Physics,* vol. 181, pp. 67-74, 2004, DOI: http://hdl.handle.net/1783.1/47229.

[8] P. Grima-Gallardo, M. Palmera, M. Munoz, S. Duran, M. Quintero, E. Quintero, L. Nieves, E. Moreno, M. A. Ramos and H. Romero, "History of superconductivity," *Adv. Mat. Sci. & Technol, Phy. DIv.,* vol. 17, no. 2, pp. 01-11, 2013.

[9] E. F. Talantsev, N. M. Strickland, S. C. Wimbush and W. P. Crump, "The onset of dissipation in high-temperature superconductors: Self-field experiments," *AIP Advances,* vol. 7, no. 12, 125230, 2017, DOI: https://doi.org/10.1063/1.4997261.

[10] Ł. Tomków, "Investigations on superconducting magnetic shields based on YBCO and BSCCO," M.S. thesis, Univ. of Cambridge, 2013. Accessed 05/12/2019. DOI: 10.13140/2.1.2727.8722.

[11] S. J. Ling, J. Sanny and W. Moebs, "University Physics Volume 3," 23 July 2019. [Online]. Available: https://opentextbc.ca/universityphysicsv3openstax/chapter/superconductivity/. [Accessed December 6, 2019].

[12] "Vortices,"Ame en Science Studio,

[Online]. Available: http://www.supraconductivite.fr/en/index.php?p=supra-levitation-vortex-more. [Accessed December 6, 2019].

[13] R. M. Scanlan, A. P. Malozemoff and D. Larbalestier, "Superconducting materials for large scale applications," *Proc. IEEE,* vol. 92, no. 10, pp. 1639 - 1654, 2004, DOI: 10.1109/JPROC.2004.833673.

[14] D. A. Cardwell and D. S. Ginley, Eds., "Part E Applications," in *A Handbook of Superconducting Materials*, vol. II, Bristol, UK: Institute of Physics Publishing, 2003, p. 1610.

[15] Hoffman Lab, "Index of /materials/images," 1 04 2018. [Online]. Available: http://hoffman.physics.harvard.edu/materials/images/SCimages/BSCCOstructure.gif. [Accessed February 2, 2020].

[16] J. H. Durrell, A. R. Dennis, J. Jaroszynski, M. D. Ainslie, K. G. B. Palmer, Y. H. Shi, A. M. Campbell, Hull, M. Strasik, E. E. Hellstrom and D. A. Cardwell, "A trapped field of 17.6 T in melt-processed, bulk Gd-Ba-Cu-O reinforced with shrink-fit steel," *Supercond. Sci. Tech.,* vol. 27, no. 8, 082001, 2014, DOI: 10.1088/0953-2048/27/8/082001.

[17] M. D. Ainslie and H. Fujishiro, "Modelling of Bulk superconductor magnetisation," *Supercond. Sci. Technol.,* vol. 28, no. 5, 053002, 2015, DOI: 10.1088/0953-2048/28/5/053002.

[18] D. Zhou, "Improvement of Trapped Magnetic Flux Density in Melt-Textured RE-Ba-Cu-O Bulk Superconductors," Ph.D. dissertation, Tokyo Univ. Marine Sc. Tech., Tokyo, Tokyo, 2013.

[19] T. Ida, K. Shigeuchi, S. Okuda, M. Watasaki and M. Izumi, "Waveform control pulse magnetization for HTS bulk magnet," *Journal of Physics: Conference Series,* vol. 695, no. 1, 012009, 2016, DOI:10.1088/1742-6596/695/1/012009.

[20] X. Feng, G. Gao, K. Davey, M. Werst, R. Hebner, R. Weinstein, D. Parks and R. Sawh, "Radial Flux High Temperature Superconductor Motor Using Bulk Trapped Field Magnets," *2009 IEEE International Electric Machines and Drives Conference,* pp. 458-464, 2009, DOI: 10.1109/IEMDC.2009.5075246.

[21] J. H. Durrell, M. . D. Ainslie, D. Zhou, P. Vanderbemden, T. Bradshaw, S. Speller, M. Filipenko and A. . D. Cardwell, "Bulk superconductors: a roadmap to applications," *Supercond. Sci. Technol.,* vol. 31, no. 10, 103501, 2018, DOI: 10.1088/1361-6668/aad7ce.

[22] F. J. T. E. Ferreira, J. A. C. Fong and A. T. de Almeida, "Ecoanalysisof Variable-speed drives for flow regulationin pumping systems," *IEEE Tans. Ind. Electron,* vol. 58, no. 6, pp. 2117-2125, 2011, DOI: 10.1109/TIE.2010.2057232.

[23] "Synchronous Motor–Construction, Principle, Types, Characteristics," Electricalfunda.com, [Online]. Available: https://electricalfundablog.com/synchronous-motor/. [Accessed December 7, 2019].

[24] "IEEE Guide: Test Procedures for Synchronous Machines Part I--Acceptance and Performance Testing Part II-Test Procedures and Parameter Determination for Dynamic Analysis," *IEEE Std 115-1995,* pp. 1-198, 1996, DOI: 10.1109/IEEESTD.1996.7328817.

[25] L. T. Mthombeni and P. Pillay, "Core losses in motor laminations exposed to high frequency or non-sinusoidal excitation," *IEEE Trans. Ind. Appl.,* vol. 40, no. 5, pp. 1325-1332, 2004, DOI: 10.1109/TIA.2004.834099.

[26] A. E. Fitzgerald, J. C Kingsley and A. Kusko, Electric Machinery, 3rd ed., New York, USA: McGraw-Hill, 1971, pp. 11-217.

[27] M. Ranlof, A. Wolfbrandt, J. Lindenholm and U. Lundin, "Core loss predition in large hydropower generators: Influence of rotational fields," *IEEE Trans. Magn.,* vol. 45, no. 8, pp. 3200-3206, 2009, DOI: 10.1109/TMAG.2009.2019115.

[28] G. Bertotti, "General properties of power losses in soft ferromagnetic materials," *IEEE Trans. Magn.,* vol. 24, no. 1, pp. 621-630, 1988, DOI: 10.1109/20.43994.

[29] M. S. Ahmed, "Effect of harmonics on iron losses," Ph.D dissertation, Dept. Ene. Env., Chalmers Univ., Goetenborg, Väst., 2007.

[30] M. Ainslie and H. Fujishiro, "Fundamentals of bulk superconducting materials," in *Numerical Modelling of Bulk Superconductor Magnetisation*, IOP, 2019, pp. 1-1 - 1-22, DOI: 10.1088/978-0-7503-1332-2ch1.

[31] T. Naito, H. Mochizuki, H. Fujishiro and H. Teshima, "Trapped magnetic-field properties of prototype for Gd-Ba-Cu-O/MgB2 hybrid-type superconducting bulk magnet," *Supercond. Sci. Technol.,* vol. 29, no. 3, 034005, 2016, DOI: 10.1088/0953-2048/29/3/034005.

[32] G. Klaus, M. Wilke, J. Frauenhofer, W. Nick and H.-W. Neumueller, "Design Challenges and Benefits of HTS," in *2007 IEEE Power Engineering Society General Meeting*, Tampa, FL, USA, 2007, DOI: 10.1109/PES.2007.385756.

[33] Y. Wang, Basic structure and Principle of Superconducting Apparatus in Power System, Singapore: John Wiley & Sons, 2013.

[34] B. Wang, "36.5 Megawatt superconducting motor Successfully Tested at Full Power," 13 Jan. 2009. [Online]. Available: https://www.nextbigfuture.com/2009/01/365-megawatt-superconducting-motor.html. [Accessed December 7, 2019].

[35] "Third IMO GHG Study 2014," Imternational Maritime Organisation, 2020. [Online]. Available: http://www.imo.org/en/OurWork/Environment/PollutionPrevention/AirPollution/Pages/Greenhouse-Gas-Studies-2014.aspx. [Accessed January 14, 2020].

[36] J. L. Kirtley, Jr, A. Banerjee and S. Englebretson, "Motors for Ship Propulsion," *Proc. IEEE,* vol. 103, no. 12, pp. 2320-2332, 2015, DOI: 10.1109/JPROC.2015.2487044.

[37] P. W. Eckels and G. Snitchler, "5 MW High Temperature Superconductor Ship Propulsion Motor Design and Test Results," *Naval Engineers Journal,* vol. 117, no. 4, pp. 31-36, 2005, DOI: https://doi.org/10.1111/j.1559-3584.2005.tb00381.x.

[38] K. Yamaguchi, M. Motohiro, K. Yamagata, T. Ikeda, H. Kashima, M. Izumi, Y. Murase, E. Yanase and T. Yanamoto, "Study of HTS Machine System Cooling With a Closed-Loop Thermosyphon : Stability of Unsteady Heat Load and Transient Conduction," *IEEE Trans. Appl. Supercond.,* vol. 26, no. 3, 5204405, 2016, DOI: 10.1109/TASC.2016.2533919.

[39] B. Chen, G.-B. Gu, G.-Q. Zhang, F.-C. Song and C.-H. Z. Zhao, "Analysis and Design of Cooling System in High Temperature Superconducting Synchronous Machines," *IEEE Trans. Appl. Supercond.,* vol. 17, no. 2, pp. 1557 - 1560, 2007, DOI: 10.1109/TASC.2007.898031.

[40] H. Teshima and M. Morita , "Recent Progress in HTS Bulk Technology and Performance at NSC," *Physics Procedia,* vol. 36, pp. 572-575, 2012, DOI: https://doi.org/10.1016/j.phpro.2012.06.086.

[41] S. Nariki, N. Sakai and M. Murakami, "Melt-processed Gd-Ba-Cu-O superconductor with trapped of 3 T at 77 K," *Supercond. Sci. Technol.,* vol. 18, p. S126, 2004, DOI: 10.1088/0953-2048/18/2/026.

[42] F. Shimoyashiki, K. Takahashi, T. Naito and M. D. Ainslie, "Trapped Field Properties of GdBaCuO Bulk Superconductors of Various Diameters Magnetized by Pulsed Fields Using an Identical Split Coil," *IEEE Trans Appl. Supercond.,* vol. 29, no. 5, 6802405, 2017, DOI: 10.1109/TASC.2019.2901349.

[43] H. Fujishiro, T. Tateiwa, A. Fujiwara, T. Oka and H. Hayashi, "Higher trapped field over 5 T on HTSC bulk by modified pulse field magnetizing," *Physica C: Superconductivity and its Applications,* Vols. 445-448, pp. 334-338, 2006, DOI: https://doi.org/10.1016/j.physc.2006.04.077.

[44] H. Fujishiro, K. Takahashi, T. Naito, Y. Yanagi, Y. Itoh, T. Nakamura and M. D. Ainslie, "Influence of Inner Diameter and Height of Ring-Shaped REBaCuO Bulks on Trapped Field and Mechanical Stress During Field-Cooled Magnetization," *IEEE Trans. Appl. Supercond.,* pp. 1-1, 2019, DOI: 10.1109/TASC.2019.2896782.

[45] J.-F. Fagnarda, S. Kirsch, M. Morita, H. Teshima, B. Vanderheyden and P. Vanderbemden, "Measurements on magnetized GdBCO pellets subjected to small transverse ac magnetic fields at very low frequency: Evidence for a slowdown of the magnetization decay," *Physica C. Superconductivity,* vol. 512, pp. 42-53, 2015, DOI: https://doi.org/10.1016/j.physc.2015.03.005.

[46] K. Yamagishi, O. Tsukamoto, J. Ogawa and D. Miyagi, "Study on Method to Suppress Decay of Trapped Magnetic Fluxes in the HTS Bulk Subjected to Pertubation of External Magnetic Field by Use of Shielding Coil Wound of HTS Wire," *IEEE Trans. Appl. Supercond.,* vol. 21, no. 3, pp. 3320 - 3324, 2011, DOI: 10.1109/TASC.2010.2093111.

[47] T. Nitta, "Superconducting rotating machines: A review of the past 30 years and future prospectives," *J. Phys.: Conf. Ser.,* vol. 1054, 012081, 2018, DOI: 10.1088/1742-6596/1054/1/012081.

[48] T. Ageta, "Recent R&D status for 70 MW class superconducting generators in the Super-GM project," *Supercond. Sc. Tech.,* vol. 13, no. 5, pp. 510-515, 2000, DOI : 10.1088/0953-2048/13/5/316.

[49] K. S. Haran, S. Kalsi, T. Arndt, H. Karmaker, R. Badcock, B. Buckley, T. Haugan, M. Izumi, D. Loder and J. W. Bray, "High power density superconducting rotating machines- developing status and technology roadmap," *Supercond. Sci. Technol.,* vol. 30, no. 12, 123002, 2017, DOI: 10.1088/1361-6668/aa833e.

[50] T. A. Keim, T. E. Laskaris, J. A. Fealey and P. A. Rios, "Design and Manufacture of a 20 MVA Superconducting Generator," *IEEE Trans. Power Apparat. Syst.,* Vols. PAS-104, no. 6, pp. 1474-1483, 1985, DOI: 10.1109/TPAS.1985.319162.

[51] P. Tixador, Y. Brunet, P. Vedrine, Y. Laumond and J. L. Sabrie, "Electrical tests on a fully superconducting synchronous machine," *IEEE Trans. Magn.,* vol. 27, no. 2, pp. 2265-2259, 1991, DOI: 10.1109/20.133665.

[52] K. Yamaguchi, M. Takahashi, R. Shiobara, T. Taniguchi, H. Tomeoku, M. Sato, H. Sato, Y. Chida, M. Ogihara , R. Takahashi and H. Kusafuka, "70 MW class superconducting generator test," *IEEE Trans. Appl. Supercond.,* vol. 9, no. 2, pp. 1209-1212, 1999, DOI: 10.1109/77.783517.

[53] B. Gamble, G. Snitcher and T. MacDonald, "Full Power Test of a 36.5 MW HTS Propulsion Motor," *IEEE Trans. Appl. Supercond.,* vol. 21, no. 3, pp. 1083-1088, 2011, DOI: 10.1109/TASC.2010.2093854.

[54] L. H. Zheng, X. J. Jin, Y. G. Guo and J. G. Zhu, "Technical and Theoretical Analysys of HTS Machines and their Development," *Nature Sciences,* vol. 1, no. 1, pp. 33-41, 2006.

[55] H. Matsuzaki, Y. Kimura, I. Ohtani, M. Izumi, T. Ida, Y. Akita, H. Sugimoto, M. Miki and M. Kitano, "An axial gap-type HTS bulk synchronous motor excited by pulsed-field magnetization with vortex-type armature copper windings," *IEEE Trans. Appl. Supercond.,* vol. 15, no. 2, pp. 2222-2225, 2005.

[56] M. Miki, S. Tokura, H. Hayakawa, H. Inami, M. Kitano, H. Matsuzaki, Y. Kimura, I. Ohtani, E. Morita, H. Ogata, M. Izumi, H. Sugimoto and T. Ida, "Development of a Syncronous Motor with Gd-Ba-Cu-Obulk Superconductors as Pole-Field Magnets for Propulsion System," *Supercond. Sci.Technol.,* pp. S494-S499, 2006.

[57] H. Matsuzaki, Y. Kimura, E. Morita, H. Ogata, T. Ida, M. Izumi, H. Sugimoto, M. Miki and M. Kitano, "HTS Bulk Pole-Field Magnets Motor With a Multiple Rotor Cooled by Liquid Nitrogen," *IEEE Trans. Appl. Supercond.,* vol. 17, no. 2, pp. 1553-1556, 2007, DOI: 10.1109/TASC.2007.898488.

[58] T. Yanamoto, M. Izumi, M. Yokoyama and K. Umemoto, "Electric Propulsion Motor Development for Commercial Ships in Japan," *Proceedings of the IEEE,* vol. 103, no. 12, pp. 2333-2343, 2015, DOI: 10.1109/JPROC.2015.2495134.

[59] H. Matsuzaki, Y. Kimura, I. Ohtani, M. Izumi, T. Ida, Y. Akita, H. Sugimoto, M. Miki and M. Kitano, "An axial gap-type HTS bulk synchronous motor excited by pulsed-field magnetization with vortex-type armature copper windings," *IEEE Trans. Appl. Supercond.,* vol. 15, no. 2, pp. 2222-2225, 2005, DOI: 10.1109/TASC.2005.849617.

[60] K. Umemoto, K. Aizawa, M. Yokoyama, K. Yoshikawa, Y. Kimura, M. Izumi, K. Ohashi, M. Numano, K. Okumura, M. Yamaguchi, . Y. Gocho and E. Kosuge, "Development of 1 MW-class HTS motor for podded ship propulsion system," *Journal of Physics: Conference Series,* vol. 234, no. 3, 032060, 2010, DOI: 10.1088/1742-6596/234/3/032060.

[61] S. D. Umans and B. A. Shoykhet, "Quench in High-Temperature Superconducting Motor Field Coils: Experimental Results," *IEEE Trans. Ind. Appl.,* vol. 42, no. 4, pp. 983-989, 2006, DOI: 10.1109/TIA.2006.877738.

[62] K. Yamaguchi, M. Miki, E. Shaanika, M. Izumi and T. Murase, "Study of Neon Heat Flux in Thermosyphon Cooling System for High-Temeperature Superconducting Machinery," *International Journal of Thermal Sciences ,* vol. 142, pp. 258-265, 2019.

[63] M. Habte, Thermal Hydraulic Annalysis of Two-Phase Closed Thermosyphon Cooling System for New Cold Neutron Source Moderator of Breazeale Reseach Reactor at Penn State, Saabruecken, Germany: VDM, 2009.

[64] R. W. Fast, Ed., Advances in Cryogenic Engineering, vol. A & B, Batavia, Illinois, USA: Springer, 1990.

[65] T. J. McCoy, "Thermosyphon-Cooled Axial Gap Electric Motors for Ship Propulsion Applications," Ph.D. dissertation, Dept. Ocean Eng., MIT, Cambridge, Massach. ,1995.

[66] D. G. Gilmore, Ed., Spacecraft Thermal Control Handbook: Cryogenics, vol. II, California, USA: The Aerospace Press, 2002.

[67] A. C. Yunus and A. G. Afshin, Heat and Mass Transfer Fundamentals & Applications, New York, USA: Mcgraw-Hill Education, 2015.

[68] D. G. Gilmore, Ed., Spacecraft Thermal Control Handbook: Fundamental technologies, vol. I, El Segudo, California, USA: The Aerospace Press, 2002.

[69] M. Izumi, M. Miki and M. Kitano, "Cryo-rotary Joint". Japan Patent 8616587, 31 Dec. 2013.

[70] S. J. Chapman, Electric Machinery Fundamentals, New York, USA: McGraw Hill, 2005.

[71] S. S. Kalsi, Applications of High Temperature Superconductors To Electrical Power Equipment, New Jersey: John Wiley & Sons Inc., 2011.

[72] K. Yamaguchi, M. Miki, E. Shaanika, M. Izumi and T. Murase, "Study of Neon Heat Flux in Thermosyphon Cooling System for High-Temperature Superconducting Machinery," *International Journal of Thermal Sciences,* vol. 142, pp. 258-265, 2019, DOI: https://doi.org/10.1016/j.ijthermalsci.2019.04.030.